University of Nottingham



In-situ monitoring of production of large composite structures using tool embedded capacitors

Galatée P. Levadoux, MSc

Supervisors: Prof. Trevor Benson, Dr A Vukovic, Prof. P Sewell, Dr Chris Worrall, Dr Mihalis Kazilas

Thesis submitted to the University of Nottingham for the degree of Doctor of Philosophy

March 2019

Abstract

The development of a new coplanar dielectric sensor able to monitor the entire process used for the manufacture of large composites panels was the main focus of this study. The cure reaction of an industrially available epoxy resin was investigated using differential scanning calorimetry and dynamic viscometry. A kinetics model of the resin cure was proposed for both constant heating rates and isothermal conditions. The theory of dielectric monitoring was outlined and electrical equivalent circuit were used in order to model the variations of the admittance due to the microscopic behaviour of the resin during cure. Electrical circuit equivalents were similarly used to model the variations of the sensor admittance during the filling of an infusion mould with liquid resin.

Several dielectric sensor prototypes were built in order to validate the geometry and fabrication protocol of the final prototype. These sensors were used to collect the variations of admittance in a frequency range of 1 Hz - 10 kHz during the infusion of glycerol, the infusion of unreinforced epoxy resin and the cure of the said resin. The results obtained with the first prototypes confirmed the chosen geometry and structure of the sensor was suitable to follow the infusion and cure of epoxy resin. A first attempt at 3D modelling of the sensor was carried out.

A final prototype of flexible and reusable dielectric sensor was built and used to monitor the infusion and cure of unreinforced epoxy resin, as well as the infusion and cure of glass fibre/epoxy composite plates in a frequency range of 1 Hz – 10 kHz. The results obtained confirmed the prototype was able to follow the filling of an infusion mould in two dimensions, as well as the cure of glass fibre/epoxy composite plates on a scale of centimetres. The influence of the number of reinforcement layers on the admittance measured was found inexistent. The admittance obtained during the epoxy resin cure confirmed the prevalence of the migrating charges contribution to the resin admittance in the frequency range studied. The comparison of the results obtained with the resin characterisation data suggested a way to closely follow the cure near the gel point of the resin.

“We are at the very beginning of time for the human race. It is not unreasonable that we grapple with problems. But there are tens of thousands of years in the future. Our responsibility is to do what we can, learn what we can, improve the solutions, and pass them on.”

— Richard P. Feynman

Acknowledgements

The present work would not have been possible without the help of my supervisors, Professor Trevor Benson, Dr Ana Vukovic, Professor Philip Sewell, Dr Mihalis Kazilas and Dr Chris Worrall. My appreciation extends to my colleagues in ACS as well as Dr Jan Przydatek and Dr Linda Starink, for their support when things did not go as planned.

Thanks to my Engineering Science teachers, MM. Spennato, Morize and Peugon, who fed my interest in “real life” science.

Finally, I would like to thank my parents for their endless patience and faith in me, as well as my friends Dave, Gerald, Helen, Jacob, Josh, Muhammad, Mirjam and Roger for their moral support. And Adam, you were right: *Cthulhu vincit.*

This work was funded by NSIRC and LRF Register.

Table of Contents

1. Necessity of Online Cure Monitoring and Thesis Structure 1

1.1. Scope and objectives 1

1.2. Composite materials and their importance in the wind turbine industry 1

1.3. Thesis structure 3

2. Wind Turbine Blade Manufacture, Potential Defects and Current Online Monitoring Solutions 5

2.1. Scope and objectives 5

2.2. Blade fabrication process and potential issues 5

2.2.1. Current design 5

2.2.2. Materials for rotor blades shells 6

2.2.3. Manufacture of the blades 10

2.2.4. Possible defects 13

2.3. Current dielectric sensing techniques for composite cures 15

2.3.1. Interest of dielectric analysis for thermosets cure monitoring 15

2.3.2. Existing dielectric sensors 17

2.4. Chapter Summary 22

3. Epoxy Resin Characterisation 24

3.1. Scope and objectives 24

3.2. Cure of epoxy resin 24

3.2.1. Mechanism 25

3.2.2. Semi-empirical kinetics models of epoxy resin cure 26

3.3. Differential scanning calorimetry 29

3.3.1. Experimental protocol 30

3.3.2. Experimental results 32

3.3.3. Kinetics model 39

3.4. Rheology of the RS-M135 epoxy resin during cure 42

3.4.1. Experimental protocol 43

3.4.2. Experimental results 45

3.5. Rheology and DSC experiments comparison 50

3.6. Chapter Summary 53

4. Theory of Dielectric Monitoring 54

4.1. Scope and objectives 54

4.2. Dielectric monitoring principle 54

4.3. Theory of dielectric monitoring thermosets 56

4.3.1. Charge migration 56

4.3.2. Electrode polarisation 57

4.3.3. Dipolar relaxation 59

4.3.4. Other phenomena 61

4.3.5. Total permittivity 62

4.4. Equivalent circuits of the sensor prototype 63

4.4.1. Relation between permittivity and admittance 63

4.4.2. Equivalent circuits for the different phenomena 64

4.4.3. Equivalent circuit of the overall sensor + resin system 70

4.5. Chapter Summary 73

5. Preliminary Dielectric Sensor Prototypes: Development and Characterisation 75

5.1. Scope and objectives 75

5.2. Sensor prototypes manufacture 75

5.2.1. PCB sensor 76

5.2.2. Kapton® film prototype 77

5.2.3. First PEEK-based prototypes 78

5.3. Composite plates manufacture and monitoring 82

5.3.1. Composite material components 82

5.3.2. Infusion and cure methodology 84

5.3.3. Dielectric measurement device 86

5.4. Prototypes tests 88

5.4.1. Kapton® prototype 88

5.4.2. PEEK prototypes 105

5.5. Chapter Summary 107

6. Final Prototype of the Flexible Dielectric Sensor 109

6.1. Scope and objectives 109

6.2. Sensor prototype fabrication 109

6.3. Prototype characterisation in air 111

6.4. Infusion process 114

6.4.1. Glycerol 114

6.4.2. 3 Layers of reinforcement 118

6.4.3. 6 Layers of reinforcement 122

6.5. Composite cure 127

6.5.1. Epoxy only 127

6.5.2. 3 Layers of glass fibres 132

6.5.3. 6 layers of glass fibres 135

6.6. Prototype characterisation at the end of the cure 137

6.7. Discussion 140

6.8. Chapter Summary 144

7. Conclusions and Suggestions for Further Work 146

7.1. Conclusions 146

7.2. Suggestions for further work 148

8. References 150

List of Figures

Figure 2.1 ***Schematic of the inside of a turbine blade*** **6**

Figure 2.2 ***Representation of a composite material. In blue, the reinforcement, in white the matrix*** **6**

Figure 2.3 ***Classification of composites. In red, the family of composite studied in the present work*** **(*Adapted from* Matthews and Rawlings 1999)** **7**

Figure 2.4 ***Schematic of a resin infusion process*** **12**

Figure 2.5 ***Parallel plate sensor. In blue, the medium investigated, in grey the electrodes*** **18**

Figure 2.6 ***Schematic of a comb dielectric sensor. In black, the interdigitated electrodes, in orange the substrate*** **19**

Figure 2.7 ***Representation of the penetration depth of the electric field with different spacing of the sensor electrodes*** **(*adapted from* Mamishev *et al.* 2004)** **20**

Figure 2.8 ***Representation the electric field repartition for different electrode grounding*** **(*adapted from* Mamishev *et al.* 2004)** **20**

Figure 3.1 ***Epoxy functional group*** **25**

Figure 3.2 ***Pre-polymerised epoxy resin with bisphenol A*** **25**

Figure 3.3 ***Addition of an amine site to an epoxide group to form a polymer chain*** **25**

Figure 3.4 ***3D grid of epoxy resin cured with a triamine*** **26**

Figure 3.5 ***Schematic representation of the DSC chamber*** **30**

Figure 3.6 ***Heat flow in the dynamic cure of RS-M135 epoxy resin*** **32**

Figure 3.7 ***Reaction rate in the dynamic cure of RS-M135 epoxy resin at constant heating rates*** ... **35**

Figure 3.8 ***Reaction rate versus time for RS-M135 epoxy resin under isothermal conditions*** **37**

Figure 3.9 ***Reaction rate versus degree of cure for RS-M135 epoxy resin under isothermal conditions*** **38**

Figure 3.10 ***Degree of cure versus cure time for RS-M135 epoxy resin under isothermal conditions*** **39**

Figure 3.11 ***Fit of the kinetics model for the dynamic cure of RS-M135 resin*** **40**

Figure 3.12 ***Fit of the kinetics model for the isothermal cure of RS-M135 resin*** **41**

Figure 3.13 ***Geometry of the oscillatory shear test*** **43**

Figure 3.14 ***Evolution of the elastic modulus (G') and viscous modulus (G'') versus time during the cure of RS-M135 epoxy resin at T=20.8 ˚C and f=1Hz*** **46**

Figure 3.15 ***Evolution of the elastic modulus (G') and viscous modulus (G'') versus time during the cure of RS-M135 epoxy resin at T=20.8 ˚C and f=1Hz, extrapolated. A-pregel stage, B-stage of gelation*** **47**

Figure 3.16 ***Elastic modulus, viscous modulus and complex viscosity versus time during the cure of RS-M135 epoxy resin at 40 ˚C*** **49**

Figure 3.17 ***Variations of the Elastic modulus, viscous modulus and degree of cure of the RS-M135 epoxy resin at 20.8˚C*** **50**

Figure 3.18 ***Variations of the elastic modulus, viscous modulus and degree of cure of the RS-M135 epoxy resin at 40˚C*** **51**

Figure 4.1 ***Illustration of the electrode polarisation phenomenon*** **58**

Figure 4.2 ***Illustration of the polarisation effect (a) permanent dipoles randomly orientated in the absence of an electric field, (b) permanent dipoles orientated under the application of an electric field (idealised view, in reality, the dipoles tend towards an alignment with the electric field rather than achieve it), (c) induced dipoles in the absence of an electric field and (c) deformation of the electron cloud of induced dipoles in the presence of an electric field*** . **60**

Figure 4.3 ***Equivalent circuit for permanent and induced dipoles*** **65**

Figure 4.4 ***Equivalent circuit of a thermoset resin*** **66**

Figure 4.5 *Real and imaginary admittance of the uncured RS-M135 epoxy resin electrical equivalent circuit. In blue, the frequency range investigated in the present study* **67**

Figure 4.6 *Real (a) and Imaginary (b) admittance of the uncured RS-M135 epoxy resin electrical equivalent circuit and the contributions of electrode polarisation, dipolar orientation and charge migration* **68**

Figure 4.7 *Effect on an increase of R_{ion} on the real (a) and imaginary (b) admittance of the RS-M135 epoxy resin electrical equivalent circuit* **70**

Figure 4.8 *Equivalent circuit of the sensor in air* **71**

Figure 4.9 *Equivalent circuit of the partially covered sensor* **72**

Figure 4.10 *Equivalent circuit of the sensor fully covered by epoxy resin* **72**

Figure 5.1 *Prototype of a small PCB based sensor* **77**

Figure 5.2 *Schematic of the Kapton® sensor layout* **77**

Figure 5.3 *Illustration of the copper wire guiding tool* **79**

Figure 5.4 *Schematic fabrication of the "sandwich" PEEK sensor (SP_1)* **81**

Figure 5.5 *Schematic fabrication of the one-sided PEEK sensor (SP_2)* **81**

Figure 5.6 *Cut plane of the setting of a composite plate infusion showing the sensor prototype (at the bottom) and the stacking of the glass fibre woven fabric* **85**

Figure 5.7 *Top view of a composite plate infusion setting* **85**

Figure 5.8 *Infusion setup for the Kapton® based sensor* **89**

Figure 5.9 *Spectra of the admittance of the Kapton® sensors in air* **90**

Figure 5.10 : *Real (a) and imaginary (b) part of the admittance during the drawing of glycerol on top of the Kapton® sensor at respectively 136 Hz and 10 kHz* **91**

Figure 5.11 *Real (a) and imaginary (b) admittance versus length of the Kapton® sensor wetted by glycerol at respectively 136 Hz and 10 kHz* **92**

Figure 5.12 *Numerically modelled admittance of the Kapton® sensor in air. The inter-wire distance is set at 2mm* **98**

Figure 5.13 *Numerically modelled admittance of the Kapton® sensor during an infusion of glycerol. The inter-wire distance is set at 2mm* **99**

Figure 5.14: *Real (a) and imaginary (b) part of the admittance of the sensor SK_2 during infusion of epoxy resin (1 kHz). The percentage indicates the length of the sensor wetted*..... **101**

Figure 5.15 *Variations of the real (a) and imaginary (b) admittance during the infusion and cure of RS-M135 epoxy resin on top of the Kapton® based sensor. Five frequencies of excitation are presented*..... **102**

Figure 5.16 *Spectra of real (a) and imaginary (b) admittance during the cure of RS-M135 epoxy resin on the Kapton® sensor*..... **104**

Figure 5.17 *Real and imaginary admittance versus length of SP_1 wetted by glycerol at respectively 136 Hz and 10 kHz*..... **106**

Figure 5.18 *Real and imaginary admittance versus length of SP_2 wetted by glycerol at respectively 136 Hz and 10 kHz*..... **106**

Figure 6.1 *Final sensor prototype* **111**

Figure 6.2 *Spectra of the real and imaginary admittance of the dry sensor prototype (a) without reinforcement, (b) with 3 layers of glass fibre and (c) with 6 layers of glass fibre* **113**

Figure 6.3 *Real (a) and imaginary (b) admittance for three sensors of the final prototype during an infusion of glycerol (normalised)*..... **115**

Figure 6.4 *Variations of the real (a) and imaginary (b) admittance versus the length of the sensor filled during an infusion of glycerol* **117**

Figure 6.5 *Variations of the real (a) and imaginary (b) admittance versus time during the infusion of RS-M135 resin through 3 layers of glass fibre reinforcement (normalised)* **119**

Figure 6.6 ***Real (a) and imaginary (b) admittance versus percentage of the sensor wetted during the infusion of RS-M135 resin through 6 layers of glass fibre reinforcement*** **..... 121**

Figure 6.7 ***Variations of the real (a) and imaginary (b) admittance versus time during the infusion of RS-M135 resin through 6 layers of glass fibre reinforcement (normalised)*** **..... 123**

Figure 6.8 ***Real (a) and imaginary (b) admittance versus percentage of the sensor wetted during the infusion of RS-M135 resin through 6 layers of glass fibre reinforcement*** **..... 125**

Figure 6.9 ***Real (a) an imaginary (b) admittance variations during the cure of RS-M135 resin*** **..... 128**

Figure 6.10 ***Variations of the real (a) an imaginary (b) admittance during the cure of RS-M135 resin (logarithmic scale)*** **..... 129**

Figure 6.11 ***Spectra of the real (a) and imaginary (b) admittance during the cure of the of RS-M135 resin*** **..... 131**

Figure 6.12 ***Variations of the real (a) an imaginary (b) admittance during the cure of RS-M135 resin reinforced with 3 layers of woven glass fibre fabric*** **..... 133**

Figure 6.13 ***Spectra of the real (a) and imaginary (b) admittance during the cure of the of RS-M135 resin reinforced with 3 layers of woven glass fibre*** **..... 134**

Figure 6.14 ***Variations of the real (a) an imaginary (b) admittance during the cure of RS-M135 resin reinforced with 6 layers of woven glass fibre fabric*** **..... 136**

Figure 6.15 ***Spectra of the real (a) and imaginary (b) admittance during the cure of the of RS-M135 resin reinforced with 6 layers of woven glass fibre*** **..... 137**

Figure 6.16 ***Spectra of the real and imaginary admittance of the sensor prototype after full cure of the RS-M135 epoxy resin (a) without reinforcement, (b) with 3 layers of glass fibres and (c) with 6 layers of glass fibres*** **..... 139**

Figure 6.17 ***Evolution of the elastic modulus, real (a) and imaginary (b) part of the admittance during the cure of RS-M135 epoxy resin at 20 ˚C*** **..... 141**

Figure 6.18 ***Evolution of the degree of cure α, real (a) and imaginary (b) part of the admittance during the cure of RS-M135 epoxy resin at 20 ˚C*** **..... 142**

List of Tables

Table 2.1 ***Comparison of the mechanical properties of E-Glass fibres and carbon fibres*** **(Brøndsted** ***et al. 2005)*** **..... 8**

Table 2.2 ***Comparison of different composite monitoring techniques (adapted from Konstantopoulos et al. 2014)*** **..... 16**

Table 3.1 ***Total heat of reaction for the cure of epoxy resin*** **..... 34**

Table 3.2 ***Temperature and conversion at maximum reaction rate*** **..... 36**

Table 3.3 ***Final degrees of cure of RS-M135 epoxy resin under isothermal conditions for 24 hours*** **38**

Table 3.4 ***Calculated parameters of the kinetics model for the dynamic cure of RS-M135 epoxy resin at constant heating rates*** **..... 40**

Table 3.5 ***Calculated parameters of the kinetics model for the isothermal cure of RS-M135 epoxy resin*** **..... 41**

Table 4.1 ***Relations between the different immitances*** **(*adapted from* Macdonald 1987)..... 63**

Table 4.2 ***Parameters used in the theoretical electrical circuit model of the RS-M135 epoxy resin system*** **..... 67**

Table 5.1 ***RS-M135 resin properties*** **..... 83**

Table 5.2 ***RS-MH134 hardener properties*** **..... 83**

Table 5.3 ***Properties of glycerol*** **..... 88**

Table 5.4 ***Experimental and calculated values of admittance for the Kapton® sensors (in air and covered by glycerol) at 136 Hz and 10 kHz for respectively the real and imaginary part of the admittance*** **..... 94**

Table 5.5 ***Dimensions of the Kapton® sensor numerical model components*** **..... 96**

Table 5.6 ***Dielectric properties of the Kapton® sensor numerical model components*** **(Segur, 1953; Dupont, 2018)** **96**

Table 5.7 ***Comparison between the slope of the modelled and recorded admittance of SK_1 during the infusion of glycerol*** **99**

Table 5.8 ***Experimental and calculated values of admittance for the PEEK sensors (in air and covered by glycerol)*** **107**

Table 6.1 ***Capacitance obtained experimentally for sensor with and without glass fibre reinforcement*** **114**

Table 6.2 ***Value for the admittance of the dry sensor obtained with linearization, experimentally and their relative error*** **118**

Table 6.3 ***Value for the admittance of the dry sensor with 3 layers of glass fibres obtained with linearization, experimentally and their relative error*** **122**

Table 6.4 ***Value of the admittance of the dry sensor with 6 layers of glass fibres obtained with linearization, experimentally and their relative error*** **126**

Table 6.5 ***Capacitances of the sensors after full resin cure*** **139**

Table 6.6 ***Location of the dipole relaxation peaks and corresponding degree of cure for the RM-S135 resin cure at 20˚C*** **143**

Nomenclature

The symbols used in the present work are listed in alphabetical order.

Symbol	Description	Unit
A	Parameter constant	$Ohm.s^{v}$
A	Pre-exponential function	min^{-1}
A_1	Pre-exponential function	min^{-1}
A_k	Pre-exponential function	min^{-1}
A_l	Linearization slope	Ohm^{-1}
B	Ratio amine equivalents/epoxides equivalents	
B_l	Linearization ordinate	Ohm^{-1}
C_0	Air capacitance	F
$C_{covered}$	Capacitance of the wetted part of the sensor	F
C_{dry}	Capacitance of the dry part of the sensor	F
C_{ind}	Capacitance due to induced dipoles	F
C_{perm}	Capacitance due to permanent dipoles	F
C_{sensor}	Capacitance of the dry sensor	F
C_{tot}	Capacitance of the wetted sensor	F
D	Displacement field	$C.m^{-2}$
d_b	Double layer width	m
De	Distance between parallel electrodes	m
E	Electric field	$V.m^{-1}$
E1	Activation energy	$J.mol^{-1}$

E2	Activation energy	$J.mol^{-1}$
Ea	Activation energy	$J.mol^{-1}$
f	Frequency	Hz
f_{amine}	Functionality of the reactive amine	
f_{epoxy}	Functionality of the epoxy resin	
G'	Elastic modulus	Pa
G''	Loss modulus	Pa
H	Heat measured by the DSC	J
H_T	Total heat of reaction	J
i	Sinusoidal current	A
I*	Complex current	A
I_0	Current amplitude	A
J	Current density	$A.m^{-2}$
J_e	Externally generated current density	$A.m^{-2}$
k	Reaction rate	min^{-1}
k1	Reaction rate	min^{-1}
k1'	Reaction rate	min^{-1}
k2	Reaction rate	min^{-1}
l%	Percentage of the dielectric sensor covered	
M	Number of independent measurement of an array of parallel electrodes	
m	Exponent of the cure kinetics model	
m_{amine}	Number of mole of amine reactant	mol

m_{epoxy}	Number of mole of epoxy reactant	mol
M*	Complex modulus	
N	Number of parallel electrodes	
n	Exponent of the cure kinetics model	
n_1	Exponent of the cure kinetics model	
n_2	Exponent of the cure kinetics model	
Ni	Number of charge carrier per unit of volume	
n_p	Degree of polymerisation of the epoxy resin	
qi	Charge of the species i	$V.m^{-1}$
$Q_{j,v}$	Volumetric source of current inside the selected modelled layers	$A.m^{-3}$
$R_{covered}$	Resistance of the wetted part of the sensor	Ohm
R_{dip}	Dipolar resistance	Ohm
R_{dry}	Resistance of the dry part of the sensor	Ohm
R_{ion}	Ionic resistance	Ohm
R_{perm}	Resistance due to permanent dipoles	Ohm
R_{sensor}	Resistance of the dry sensor	Ohm
R_{tot}	Resistance of the wetted sensor	Ohm
T	Temperature	˚C, K
t	Time	min, s
tanδ	Loss factor	
T_g	Glass transition temperature	˚C
T_r	DSC Reference temperature	˚C

T_s	DSC Sample temperature	˚C
u	Charged species mobility	$m^2.V^{-1}.s^{-1}$
v	Sinusoidal voltage	V
V*	Complex voltage	V
V_0	Voltage amplitude	V
v_i	Charged species velocity	$m.s^{-1}$
Y'	Real part of the complex admittance	Ohm^{-1}
Y''	Imaginary part of the complex admittance	Ohm^{-1}
Y*	Complex admittance	Ohm^{-1}
Y^*_{dip}	Complex admittance due to the presence of dipoles	Ohm^{-1}
Y^*_{dry}	Complex admittance of the dry sensor	Ohm^{-1}
Y^*_{EP}	Complex admittance due to the electrode polarisation	Ohm^{-1}
Y^*_{ion}	Complex admittance due to the presence of migrating charges	Ohm^{-1}
Y^*_{tot}	Complex admittance of the fully wetted sensor	Ohm^{-1}
Y'_{dry}	Real admittance of the dry sensor	Ohm^{-1}
Y''_{dry}	Imaginary admittance of the dry sensor	Ohm^{-1}
Y_{meas}	Admittance measured by the dielectric sensor prototype	Ohm^{-1}
Y'_{tot}	Real admittance of the fully wetted sensor	Ohm^{-1}
Y''_{tot}	Imaginary admittance of the fully wetted sensor	Ohm^{-1}
Z*	Complex impedance	Ohm
α	Degree of cure of the epoxy resin	
α_{gel}	Degree of cure of the epoxy resin at gel point	
γ	Strain	

γ_0	Stain amplitude	
δ_{ar}	Relative error	
δ_p	Penetration depth of the electric field	m
δ_v	Phase between stress and strain	
ε'	Real part of the complex permittivity	
ε''	Imaginary part of the complex permittivity	
ε^*	Complex permittivity	
ε^*_{dipole}	Complex permittivity due to the presence of dipolar species	
$\varepsilon^*_{electrode}$	Complex permittivity due to electrode polarisation	
ε^*_{ion}	Complex permittivity due to the presence of migrating charges	
ε'_{bulk}	Real part of the complex permittivity of the bulk material	
ε''_{bulk}	Imaginary part of the complex permittivity of the bulk material	
ε'_{dipole}	Real part of the complex permittivity due to the presence of dipolar species	
ε''_{dipole}	Imaginary part of the complex permittivity due to the presence of dipolar species	
$\varepsilon'_{electrode}$	Real part of the complex permittivity due to electrode polarisation	
$\varepsilon''_{electrode}$	Imaginary part of the complex permittivity due to electrode polarisation	
$\varepsilon'_{'iom}$	Imaginary part of the complex permittivity due to the presence of migrating charges	
ε'_{ion}	Real part of the complex permittivity due to the presence of migrating charges	

ε_r	Fully relaxed permitivitty	
ε_u	Unrelaxed permittivity	
η^*	Complex viscosity	Pa.s
ν	Fractal exponent of the electrode polarisation model	
σ	Conductivity	S.m
σ_v	Stress	Pa
σ_{v0}	Amplitude of the stress	Pa
τ	Relaxation time	s
τ_{dip}	Dipolar relaxation time	s
ϕ	Phase between voltage and amplitude	
ω	Angular frequency	$ras.s^{-1}$

Mathematical Operators and Physical Constants

R	Ideal gas constant, 8.3144598 $J.K^{-1}.mol^{-1}$
Δ	Difference
j	Imaginary unit, $j^2=-1$
ε_0	Permittivity of free space, 8.854x10-12 $F.m^{-1}$
π	Pi, 3.14
Σ	Sum

Abbreviations

The abbreviations are listed in alphabetical order.

Abbreviation	Explanation
3D	Three dimensional
AC	Alternative Current

BC	Before Christ
BNC	Bayonet Neill–Concelman
DC	Direct Current
DEA	Dielectric Analysis
DSC	Differential Scanning Calorimetry
E.P.	Electrode Polarisation
ETDR	Electrical Time Domain Reflectometry
FTIR	Fourier Transform Infrared spectroscopy
HCl	Hydrochloric Acid
I-CRTM	Injection-Compression Resin Transfer Moulding
LCI	Liquid Resin Infusion
LCM	Liquid Composite Moulding
OFI	Optical Fibre Interferometers
OFR	Optical Fibre Refractometers
PCB	Printed Circuit Board
PEEK	Polyetheretherketone
RFI	Resin Film Infusion
RTM	Resin Transfer Moulding
S_1	Prototype sensor 1
S_2	Prototype sensor 2
S_3	Prototype sensor 3
S_4	Prototype sensor 4
SK_1	Kapton® Sensor number 1
SK_2	Kapton® Sensor number 2
SP_1	PEEK Sensor Prototype number 1
SP_2	PEEK Sensor Prototype number 2
VARTM	Vacuum-Assisted Resin Transfer Moulding

1. Necessity of Online Cure Monitoring and Thesis Structure

1.1. Scope and objectives

The development of a new sensor for monitoring the manufacture of large scale composites plates is the main topic of this study. The device prototype, based on dielectrometry techniques, is used to follow the entire composite making process from the filling of the mould to the final composite plate. In this introductory chapter, the need for such a technique is outlined before the thesis structure is given.

1.2. Composite materials and their importance in the wind turbine industry

Since the beginning of times, humans have been shaping matter to manufacture objects and manifest their visions. After using readily available materials, such as wood, bone or stone, they found themselves limited and thus began to create new ones. They discovered that combining dissimilar components could provide a resulting element distinct from the sum of its parts. First developed empirically with the creation of alloys, this knowledge morphed into alchemy, before later acquiring the name of chemistry.

However, material blends are not limited to the microscopic scale. Combining materials on a macroscopic level has been done for thousands of years. Contrarily

to a homogeneous mixture, the integrity of the individual components remains in the final structure, called composite material. An example of such materials may date back from as far as the 4th Dynasty (circa 2750 BC) in the form of the oldest iron plate ever found. Discovered in the Great Pyramid of Gizeh, Egypt, it is formed of several iron laminates of different composition hammered together. Different alloys would be later treated with this hammering technique: in the Illiad, Homer describes Achilles' shield as formed of two layers of bronze, two layers of tin and one of gold (Wadsworth and Lesuer 2000).

If nowadays alloys are becoming less and less prevalent in the industry, the idea of combining dissimilar materials to create a better one remains, as illustrated by the rise of advanced composites in the last century. Fibre reinforced plastic matrix are a family of composite now widely used in the industry. Their lightweight and outstanding structural properties make them materials of choice for the creation of large structures in sectors such as aeronautics, aerospace or renewable energies. Yet, their manufacture on a large scale remains mostly based on empirical procedures. That has been proven problematic, considering that any defect during the manufacturing process might generate weak points in the final piece, likely to become later sources of failures.

In the wind energy sector, these failures can have disastrous consequences. In the case of a wind turbine breakdown, not only are costly and time-consuming repairs needed, but any interruption also implies a loss in energy produced during the whole maintenance time. If the turbine happens to be offshore, the replacement process is made all the more difficult by requiring the use of special boats able to stabilise themselves on the sea ground.

The most common cause of malfunctions of wind turbines is by far blade failure (Ciang *et al.* 2008), accounting for 8 to 20% of the cumulated downtime of a wind turbine (Hahn *et al.* 2007; Lauter *et al.* 2017). In 2011, a preliminary survey

performed by Sandia National Laboratory on five wind farms reported a blade failure on about 20% of the wind turbines panel examined. In the event of rotor blade breakage, blades or pieces of blades can travel up to one mile away from the turbine, damaging buildings and being a great safety issue (Ciang *et al.* 2008; Caithness Windfarm Information Forum 2018).

Considering that most of these failures can be linked back to improper manufacturing of the blade material, the reliability issues should be addressed at as early a stage as possible during fabrication. An online monitoring technique able to provide real time information during the manufacture of the blade would be beneficial to detect potential problems before the process is even finished, and ensure the viability of the final product. This would prevent the loss in production and the costs of potential breakages, making the wind energy sector more reliable and therefore more competitive.

1.3. Thesis structure

The main body of the present study is composed of seven chapters:

After the present chapter, where the need of an online monitoring technique for the manufacture of large scale composite panels is highlighted, chapter 2 concentrates on the manufacture techniques of the said composites and the current online monitoring techniques available.

Chapter 3 focuses on the characterisation of the resin matrix used in the present study. After a brief explanation of the cure mechanism of epoxies, the resins cure is studied by mean of differential scanning calorimetry and rheology.

Chapter 4 develops the theory behind dielectrometry. The basic principle behind dielectric monitoring are discussed, before developing the causes for the variations of the dielectric properties of the curing epoxy resin. An equivalent circuit of the

curing resin is discussed. An electric equivalent of the dielectric sensor system is likewise examined.

Chapter 5 presents the first sensor prototypes developed. It is composed of three parts: a description of the composite making protocol used in the present work is given, before the sensor prototypes fabrication is described. Finally, the results obtained with the two types of prototypes are presented. In that chapter, a brief introduction to a 3D numerical model of one sensor prototype is given.

Chapter 6 concentrates on the final sensor prototype. The first part describes the sensor prototype fabrication process. The prototype is then characterised in air, before its suitability to follow the composite manufacture process in its entirety is verified. The results obtained with the prototype are compared with the epoxy cure characterisation established in chapter 3.

An overall conclusion of the results of the present work and with suggestions for further work are summarised in chapter 7.

2. Wind Turbine Blade Manufacture, Potential Defects and Current Online Monitoring Solutions

2.1. Scope and objectives

This chapter starts by describing the manufacture process of wind turbine blades and the potential issues that can arise during this step. The focus then shifts on to the different methods of online monitoring currently available, before concentrating on the presentation of the dielectric sensors geometries currently available.

2.2. Blade fabrication process and potential issues

The design and choice of materials for the production of a wind turbine blade is crucial to ensure the efficiency and reliability of the final machine. Similarly to aeronautics, the shape of the blade must be carefully studied to be as aerodynamic as possible, and the materials used must simultaneously be strong, robust and light-weight.

2.2.1. Current design

Most blades are composed of a thin shell reinforced by spars, beams or webs as shown in Figure 2.1 (Brøndsted *et al.* 2005; Lauter *et al.* 2017). These reinforcements ensure a good repartition of the load along the blade.

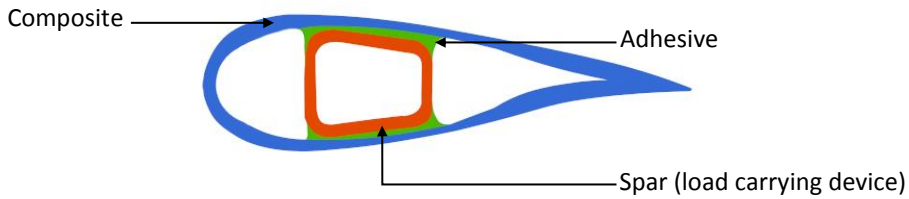


Figure 2.1 *Schematic of the inside of a turbine blade*

The challenges associated with the reinforcing beams, or the joints between the different blade parts will not be discussed further in the present work. The focus shall be kept on the blade shell manufacture and the issues arising from it, responsible for 13% of the blade failures (Galappaththi *et al.* 2013).

2.2.2. Materials for rotor blades shells

The materials used to build the shell must comply with three main constraints: they need to be stiff enough to maintain the aerodynamic design of the blade, light-weight to limit the impact of gravity on the turbine and resistant enough to fatigue load to ensure a service of 20-30 years (Veers *et al.* 2003).

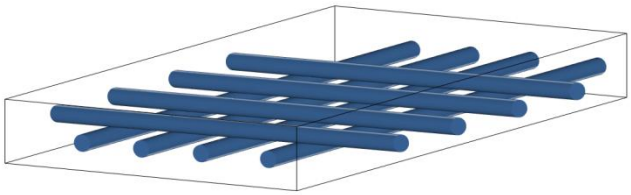


Figure 2.2 *Representation of a composite material. In blue, the reinforcement, in white the matrix*

Composite materials are therefore ideal candidates for the fabrication of the blade (Veers *et al.* 2003; Brøndsted *et al.* 2005). The term “composite” refers to a wide range of objects, from wood to ceramics. Their common point lies in their composition: two or more different materials are combined to make a final product with superior properties. Composite materials made of a fibre reinforcement embedded in a polymer matrix (Figure 2.2) have been extensively used in the

industry for decades. They are part of a much bigger family of materials, of which a classification is presented in Figure 2.3.

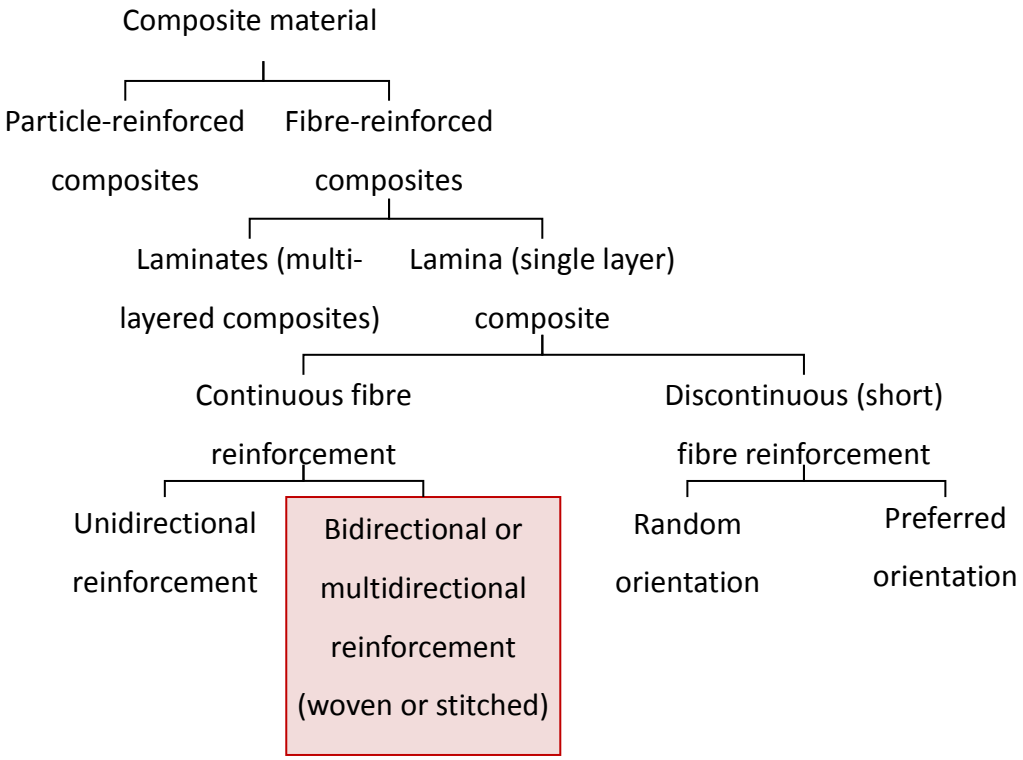


Figure 2.3 *Classification of composites. In red, the family of composite studied in the present work* (*Adapted from* Matthews and Rawlings 1999)

The present work focuses only on the dual composite system formed of fibre reinforced polymer matrix, highlighted in red in Figure 2.3 . The presentation of the two materials forming the final piece is given in the section below.

2.2.2.1. *Fibres*

The reinforcement in the composite material serves to increase the mechanical properties of a plain polymer, such as its rigidity or resistance to cracks. The reinforcement can take the form of small particles, nanoparticles or, more frequently, fibres. In the wind turbine blade manufacturing industry, the wide use of glass fibres, and especially E-Glass fibres, can be explained by their moderate

stiffness, moderate density, and high strength. All these mechanical properties are combined with a relatively low cost.

The choice of carbon fibres as a reinforcement is becoming popular, but despite their excellent mechanical properties, their price prevents them from being more prevalent. They can, however, be used in conjunction with glass fibres in strategical areas of the blade (Veers *et al.* 2003; Brøndsted *et al.* 2005). A comparison of some mechanical characteristics of E-Glass fibres and carbon fibres is given in Table 2.1.

Table 2.1 *Comparison of the mechanical properties of E-Glass fibres and carbon fibres* (Brøndsted *et al. 2005)*

Type	Stiffness (GPa)	Tensile strength (MPa)	Density (g.cm^{-3})
E-Glass	72	3500	2.54
Carbon	350	4000	1.77

Other interesting fibres such as aramid, polyethylene and cellulose can be cited, but they remain very niche. Because of the predominance of glass fibres, and more specifically E-Glass reinforcement, in the current blade manufacture process (Veers *et al.* 2003), the word "reinforcement" will exclusively refer to this kind of fibres from now on unless otherwise stated.

2.2.2.2. *Matrix*

Working as a binder, the role of the polymer matrix is to keep the fibres together and transfer the mechanical stress evenly among them. It can be made of either thermosets or thermoplastics. Thermosets are usually liquid or pourable polymers requiring a curing process to become solid. For that reason, they are mixed with a hardener, heated or irradiated under precise conditions to initiate the chemical reaction which results in the wanted final product. This curing phenomenon is a chemical reaction implying the cross-linking of macromolecules and the creation of chemical bonds. It is thus irreversible. Typical examples of thermosets used as a

matrix in the composite industry are epoxy, polyester, vinylester, bismaleimide, and phenolic resins (Gurit Holding 2016).

Alternatively, thermoplastics polymers are materials that are typically solid at room temperature, but become malleable or liquid when heated above certain temperatures, called respectively the glass transition temperature and the melting point. Contrarily to thermosets, no chemical bonds are created in the process and thus the polymer can be melted and shaped several times before it starts to deteriorate. This property makes them interesting in terms of recycling (Gurit Holding 2016). Polyetheretherketone (PEEK) is an example of a high-performance thermoplastic; polypropylene and polyamide (Nylon) are thermoplastics commonly used in industry.

The manufacture of large composite panels typically relies on thermosets resins and thus the present document will only discuss the production of composites based on such.

2.2.2.3. *Composite material*

As a combination of the reinforcement and the matrix, the final composite material possesses mechanical properties that aim to be greater than the sum of their part. The said properties are typically dependent on the ratio between the fibre and the matrix, since the reinforcement has the biggest contribution to the final material properties.

The research and development on composite materials lead to a significant increase in the length of the rotor blades. Today, they typically measure between 40 and 130 m. (Brouwer *et al.* 2003; Veers *et al.* 2003). However, the manufacturing techniques used to produce those blades did not evolve at the same rate and remain a very delicate step in the blade making process. Any defect occurring at the manufacturing stage can have dramatic consequences on the blade mechanical

properties, leading at best to expensive scrap parts, and to failure in the worst case scenario (Hahn *et al.* 2007; Galappaaththi *et al.* 2013).

2.2.3. Manufacture of the blades

Composite materials can be manufactured with various techniques such as spray lay-up, wet hand lay-up, vacuum bagging, filament winding, pultrusion, resin transfer moulding, autoclave or resin film infusion. (Brøndsted *et al.* 2005; Gurit Holding 2016). For the sake of clarity, only the two techniques relevant to rotor blades manufacture will be described here, namely wet lay-up and liquid composite moulding.

2.2.3.1. *Wet lay-up*

The wet lay-up process has been used for decades to make boat shells or chemical tanks and is still relevant for small blades up to 50 meters (Veers *et al.* 2003). It is well-known, simple, requires low-cost equipment and is applicable to a wide choice of fibres and matrix. Woven, knitted, stitched or bonded fibres fabrics are impregnated with the liquid resin which is manually deposited by rollers, or brushed, before being left to cure at room temperature and pressure (Gurit Holding 2016).

However, not only does the quality of the final product very much depend on the human factor (technical skills of the operator), but the resin used in that process needs to present a low viscosity. This limitation has an impact on the mechanical and thermal properties of the end product. Besides, the resins traditionally used in wet lay-up are potentially harmful to the operator, who can notably develop styrene emission poisoning from polyester resin and dermatitis from epoxy (Gurit Holding 2016).

2.2.3.2. *Liquid composite moulding*

Liquid composite moulding (LCM) is the process most largely used in industry to produce composite parts. It comprises several variations such as resin transfer moulding (RTM), vacuum assisted resin transfer moulding (VARTM), liquid resin infusion (LRI), resin film infusion (RFI), and injection-compression RTM (I-CRTM). All those variations are based on the same principle: the reinforcement fabric is placed into a closed area in which the liquid resin is injected. The system is then cured until solidification of the resin (Brouwer *et al.* 2003; Gurit Holding 2016).

The liquid resin infusion process is favoured for the blade manufacturing and therefore will be the only one further developed here. It can be broken into four steps, as schematised in Figure 2.4:

(1) The dry reinforcement is placed in a stack in a mould.
(2) The stack is then covered with peel ply and breathing fabric, before being vacuum-bagged. The breathing fabric is a porous media allowing an even flow of the liquid resin during the infusion. Without it, the vacuum bag would be pressed too tightly against the reinforcement to allow the resin to flow and impregnate the fibres correctly.
(3) The pressure difference between the inside of the bag (vacuumed) and the surface of the liquid resin brings it to flow into the reinforcement stack until the latter is fully impregnated. Afterwards, the resin is cured according to the manufacturer specifications.
(4) When the curing process is complete, the vacuum bag, breathing fabric and peel ply are removed. At that point, the composite obtained is ready for further assembly.

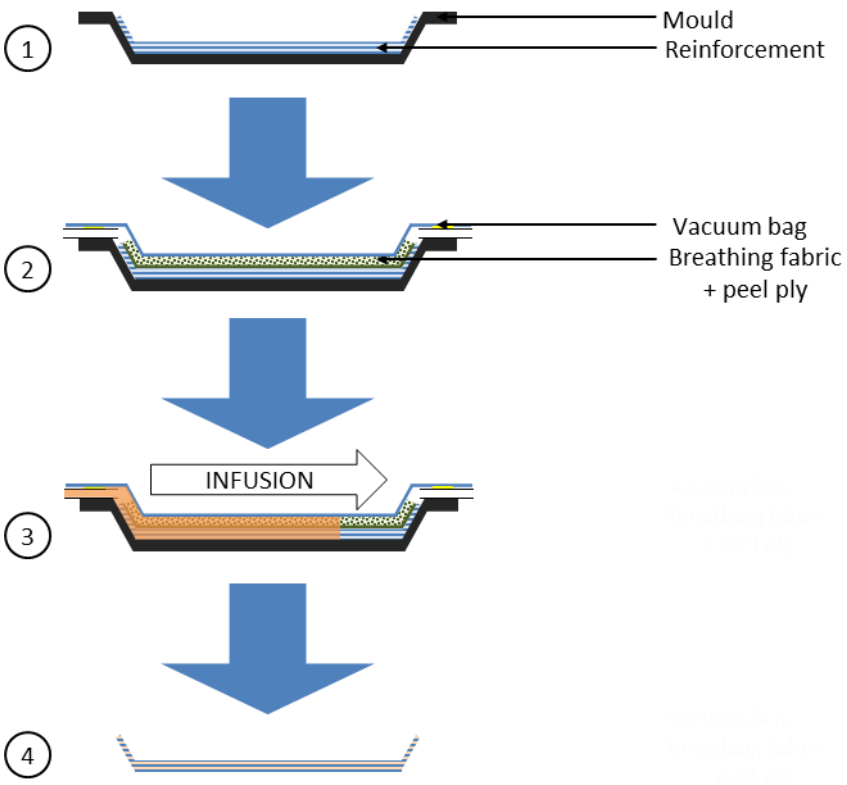


Figure 2.4 *Schematic of a resin infusion process*

The side of the final piece in contact with the mould has a smooth finish, typically corresponding to the outside of the blade shell in the case of wind turbine blade manufacture. The inside of the blade does not need to have a perfectly smooth surface, hence the use of a fully closed mould, such as the ones used in RTM processes, is not necessary. Therefore, the liquid resin infusion will be the main focus of this study.

The LCM technique allows the fabrication of large, complex shapes with very low void contents and high fibre volume in a single step and at a relatively low cost. Besides, cored structures can be produced using this technique, making it an especially interesting choice for the manufacture of blade shells in one seamless piece. Compared to wet lay-up, the health and environmental risks are reduced thanks to the resin being cured in a vacuum bag (Brouwer *et al.* 2003). Finally, the

automation of the RTM process further reduces the process time and thus reduces costs (up to 40% compared to the wet lay-up process (Long 2005)).

However, the infusion process is a complex technique that can present some issues, likely to impact the properties of the final composite (McIlhagger *et al.* 2000). The fabric can be displaced during the filling, leading to an inhomogeneous final product. The injection process itself can lead to inhomogeneity of the resin (uneven flow of the resin flux or interfaces during mould filling, dry spots, incomplete filling…), especially in the case of large structures requiring a complex infusion strategy (Brouwer *et al.* 2003). In thick laminates, the curing process can be uneven: the heat generated by the exothermic reaction at the core of the laminante is difficult to dissipate due to the poor thermal conductivity of the resin which may result in over cured matrix. Local variations in the degree of cure and thus improperly cured matrix can also occur due to the gradients of temperature (Bogetti and Gillespie, 1991). Finally, the cure cycle of the resin is typically based on the recommendations of the resin manufacturer, derived from tests on the unreinforced resin. As such, they do not accurately reflect either the geometry of the component or the constitution of the composite material.

2.2.4. Possible defects

The production of large composite panels is an industrial process that may thus result in the presence of defects in the final product, leading to potential blade failure. Those defects can be due to the blade design itself, in which case the problem must be addressed while researching the blade design, but most of them are created during the blade manufacturing process. More precisely, the resin infusion is known to be a crucial step influencing most of the mechanical properties of the final part. Defect linked to this step of manufacture can be classified into several types (Sørensen *et al.* 2004; Cairns *et al.* 2011; Galappaththi *et al.* 2013; Yang *et al.* 2013):

- Porosity/voids: air or residual gas bubbles are present in the cured composite.
- Dry spots: the reinforcement fibres are improperly wetted by the resin.
- Debonding: the matrix and fibres are no longer adhering to each other.
- Delamination: the laminated composite becomes separated, usually between two layers of reinforcement.
- Non-homogeneity in the fibre/resin distribution: Some areas are too rich in fibres/resin.
- Fibre misalignment/ ply waviness: The reinforcement fibres show waviness, along with the plan of the lay-up, or through the stack.
- Fibre cracking: the length of the fibres is reduced because of breakage.
- Foreign inclusion: foreign objects are trapped into the composite, typically between two layers of reinforcement.
- Improperly cured matrix: The polymer matrix is either over or under-cured.
- Matrix cracking: the matrix itself shows a structural failure.

Those irregularities can have a tremendous impact on the mechanical properties of the final composite piece. It has been shown that a 1% void content leads to a decrease of 10% in the inter-laminar shear strength and 5% in the bending stiffness of a cured thermoset composite (Matsuzaki *et al.* 2011b). Similarly, fibre waviness can lead to failure of flat glass fibre/epoxy composite panels at 74%-77% of their reference ultimate failure stress. Delamination causes breakage at an even lower value, around 32%-38% of the reference ultimate failure stress (Galappaaththi *et al.* 2013) .

Any of the presented defects is a potential stress concentration area under the cyclic loading of the blade. In time, it can become the starting point of bigger

structural failures, ending up in a sudden stress relief mechanism and the spectacular collapse of the blade (Yang *et al.* 2013).

Resin infusion remains a complex process, difficult to monitor, and issues during that step can lead to expensive discarded part. In addition, the number of parameters to take into account when considering each steps of the infusion process (filling of the mould, composite cure and final composite piece) makes it difficult to model it accurately. For those reasons, online control of the whole infusion process is highly desirable. Instant feedback on the filling of the mould, the cure of the resin and the potential formation and/or location of defects during the process would provide invaluable information to detect issues at an early stage during production and ensure the viability of the final piece (Matsuzaki *et al.* 2011a).

2.3. Current dielectric sensing techniques for composite cures

Considering how minor defects can have dramatic consequences on the mechanical properties of large composite pieces, close attention has been given to the monitoring of their manufacturing process. Because the risk of creating flaws is significant during resin infusion and cure, particular attention is required during these steps.

2.3.1. Interest of dielectric analysis for thermosets cure monitoring

Several online composite monitoring techniques have already been developed (Laurent-Mounier *et al.* 2005; Konstantopoulos *et al.* 2014; Lauter *et al.* 2017; Lira *et al.* 2017), including dielectric analysis (DEA), direct current analysis, electrical time domain reflectometry (ETDR), optical fibre interferometers (OFI), ultrasonic transducers, optical fibre refractometers (OFR), spectrometers, thermometers and pressure transducers. However, these techniques are poorly fitted to the industrial

scale as they require too expensive an infrastructure or too small a sample size to be industrially viable (Schubel *et al.* 2013).

For that reason, the monitoring of the resin infusion is currently limited mainly to time and temperature parameters, relying on the cure profile given by the resin manufacturer. As such, it provides little to no feedback (Lira *et al.* 2017). In addition, even if all the aforementioned techniques were to be adapted to an industrial setting, few of them would allow the monitoring of the whole infusion process from the filling of the mould to the final part, as shown in Table 2.2 (Konstantopoulos *et al.* 2014). Some of the investigation methods are even destructive and therefore cannot be considered for on-line monitoring of a wind turbine blade.

Table 2.2 *Comparison of different composite monitoring techniques (adapted from Konstantopoulos et al. 2014)*

		Flow front	Degree of cure	Void content	Delamination
Electromagnetic properties	Dielectric analysis	√	√	√	√
	Direct Current analysis	√	√		
	Electrical time domain reflectometry	√	√		
Mechanical properties	Optical fibre interferometers	√	√		
	Ultrasonic transducers	√	√	√	√
Optical properties	Optical fibre refractometers	√	√		
	Spectrometers	√	√		
Thermo-dynamical properties	Thermometers	√	√		√* *Only by Infrared (IR) thermography
	Pressure transducers	√			

Amongst all these approaches, the dielectric analysis presents the advantage of being one of the few non-destructive, well-established methods that can theoretically monitor the entire composite manufacturing process, from the filling of the tool by the resin material to the final product. This is particularly interesting in the case of E-glass/epoxy laminate composites, which are low loss dielectric materials (Chin and Lee 2007), thus making dielectric methods suitable to the monitoring of their fabrication (Bidstrup *et al.* 1989; Stephan *et al.* 1998; Skordos and Partridge 2004; Chin and Lee 2007; Yang *et al.* 2014).

During the polymerisation reaction leading to the resin solidification, its physical, chemical and structural properties undergo changes that impact the dielectric properties of the material, providing an effective means for indirect in-line non-destructive testing. In particular, it has been shown that the viscosity of the thermoset resin, directly linked to the degree of cure, presented an effect on the dielectric properties of the material (Kranbuehl *et al.* 1989). This dependence will be studied in more detail in chapter 3.

Finally, because dielectric measurement does not require the sensor to be in direct contact with the material studied, it can be embedded in a tool such as a mould and thus does not damage the surface of the material, preventing additional manufacturing (McIlhagger *et al.* 2000; Yenilmez and Murat Sozer 2009).

2.3.2. Existing dielectric sensors

In order to follow the variations of the dielectric properties of the resin system during the whole infusion process, several types of sensors have been developed. Those devices are usually composed of electrodes in contact with the material to investigate. A time-varying voltage is applied between the electrodes, establishing an electric field in the material. This electric field causes the apparition of an electric current in the material investigated. The characteristics of this current can then be

analysed to infer the properties of the material studied (Senturia and Sheppard Jr 1986). The way these devices operate will be described in more detail in chapter 4.

Dielectric sensors have been developed for the on-line monitoring of the infusion process and are starting to be employed industrially nowadays. Two main geometries are commonly found in literature: parallel plate sensor and comb or coplanar sensors. They shall be briefly discussed in the following sections.

2.3.2.1. *Parallel plate sensors*

Several laboratory studies have used a parallel plate geometry to follow the cure of epoxy resins systems (Figure 2.5) (Shigue *et al.* 2004, 2006).

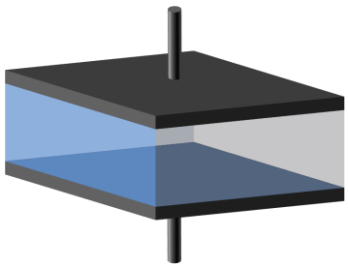


Figure 2.5 *Parallel plate sensor. In blue, the medium investigated, in grey the electrodes*

Parallel plate sensors require access to both sides of the material, which shows several advantages such as large and easily measurable capacitances as well as a more uniform field distribution in thick samples. It provides results considered more representative of the monitored process than the data obtained with a surface sensor (McIlhagger *et al.* 2000; Mamishev *et al.* 2004). Parallel plate sensors have been used to follow the cure of both an epoxy resin alone and a glass fibre reinforced composite (Nixdorf and Busse 2001). However, the necessity to have access to both sides of the curing plate makes them unsuitable to follow a liquid infusion, in which only one side of the composite remains in contact with the mould. They are also unpractical if large pieces of composites, such as rotor blades, need to be monitored across their whole surface. For these reasons, the industrial

use of parallel plate sensors seems limited in large scale composite manufacture, despite their benefits (McIlhagger *et al.* 2000).

2.3.2.2. *Co-planar sensors*

Interdigitated sensors, or comb sensors, are the most common type of dielectric sensor used when it comes to monitoring time-dependent phenomena. Composed of two co-planar electrode intertwined (Figure 2.6), they are commercially available and have been extensively used to monitor the dielectric properties of various materials, including epoxy resin during cure (Bidstrup *et al.* 1989; Kranbuehl *et al* 1997; Skordos and Partridge 2004).

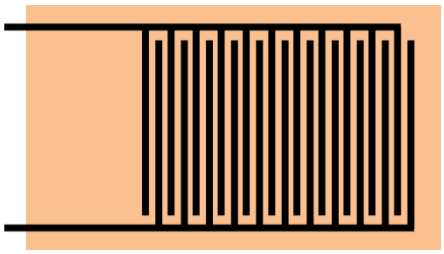


Figure 2.6 *Schematic of a comb dielectric sensor. In black, the interdigitated electrodes, in orange the substrate*

Contrarily to parallel plate sensors, interdigitated sensors do not require access to both sides of the monitored sample, making them suitable for liquid infusion processes.

The strength of the signal obtained is controlled by adjusting the geometry of the sensor as the depth of penetration of the electric field in the tested material only depends on the distance between the sensor fingers. By varying that parameter, the depth penetration of the signal is changed and a spatial profile of the material tested can potentially be achieved. This means that stratified mediums such as complex composites can be investigated without the need to access each layer separately (Mamishev *et al.* 2004).

The depth of the material investigated should be proportional to the half-distance between two driving fingers: the larger the distance, the deeper the field, as schematised in Figure 2.7.

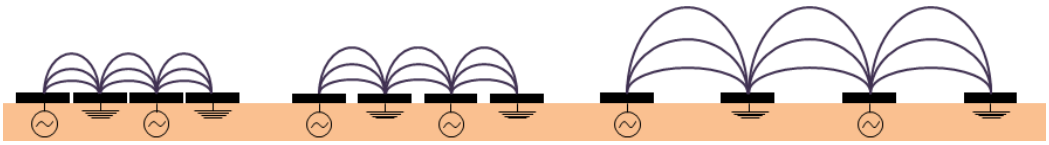


Figure 2.7 *Representation of the penetration depth of the electric field with different spacing of the sensor electrodes* (*adapted from* Mamishev *et al.* 2004)

However, the electric field intensity decreases proportionally to an exponential factor $e^{\frac{1}{\delta p}}$ (where δ_p is the penetration depth). Hence, the accuracy of the measurement decreases when the inter-finger distance increases, as the signal intensity can reach the lower limit of detection of the dielectric measurement apparatus. To solve this issue, a combination of interdigitated sensors with different geometry can be used. Another option is to address independently an array of electrodes placed on the same plane to obtain a mapping of the whole thickness, as shown schematically in Figure 2.8.

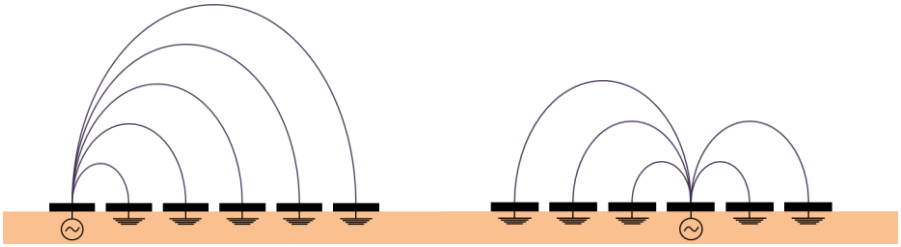


Figure 2.8 *Representation the electric field repartition for different electrode grounding* (*adapted from* Mamishev *et al.* 2004)

In that case, the number of independent measurements M is given by

$$M = \frac{N(N-1)}{2} \qquad (2.1)$$

where N is the number of electrodes (Mamishev *et al.* 2004).

The location of the coplanar sensor can be either attached to the infusion mould surface or inside the curing resin. If it is fixed on the mould, it allows the sensing system to be reusable. If the sensor remains embedded in the final composite piece, it can serve as a health monitoring device along the lifespan of the final piece, or simply be considered as a foreign inclusion. Interdigitated disposable sensors placed between reinforcement plies have been successfully used to follow the cure of glass fibre/epoxy composites (Bang *et al.* 2001; Yang *et al.* 2016).

However, the typical scale of those sensors is of the order of a few millimetres. Therefore, they can only provide local data, making the use of such devices impossible for monitoring the fabrication of large pieces of composite over their full surface. Nevertheless, the geometry of coplanar sensor seems to be adaptable to larger scales. A bigger scale, copper-based co-planar sensors has been designed and investigated, showing interesting preliminary results in its ability to monitor the flow front and cure of glass fibre-epoxy composites (Skordos *et al.* 2000).

2.3.2.3. *Other geometries*

In addition to parallel plate sensors and comb sensors, several other geometries have been studied on a laboratory scale. The SMARTweave dielectric sensor developed by the Army Research Laboratory and the University of Delaware (Vaidya *et al.* 2000) is based on a planar grid design. Consisting of several conductive filaments (carbon fibres or copper) embedded in an insulating material, it is placed in contact with the material to monitor and can follow mould filling and cure advancement in the composite making processes.

Another grid design developed consists of the equivalent of 50 small parallel plates sensors evenly spaced across the monitored area (Yenilmez and Murat Sozer 2009). To achieve this, an array of copper plates is embedded on the top of an RTM

mould. Another matching array of copper plates is embedded at the bottom of the mould, so that the closing of the machine creates 50 parallel plate capacitors able to give local information across the whole surface of the designated area.

A carbon fibre based integrated sensor has been studied to follow the cure of glass fibre epoxy composites, with positive results (Laurent-Mounier *et al.* 2005). One step further, the use of co-cured carbon electrodes was proven promising in the case of a carbon fibre reinforced composite (Inada and Todoroki 2003). This type of embedded device could allow the investigation of carbon fibre reinforced composite manufacture with a minimal impact on the final composite mechanical properties.

Last but not least, a disposable area-sensor array made of several square interdigitated sensors covering the entire bottom of a vacuum-assisted resin transfer moulding (VARTM) mould was proposed (Matsuzaki *et al.* 2011b). This device can monitor both the resin flow and the temperature during the whole process using the frequency dependence of the resin permittivity. Moreover, it is able to detect out of plane resin wetting in the reinforcement. The sensor can remain attached to the composite part after the curing process, in order to monitor the composite health as the manufacturing process continues further, or it can simply be peeled off (Matsuzaki *et al.* 2011b, 2011a, 2012) before additional manufacture.

2.4. Chapter Summary

Composite materials are more and more widely used in various applications, including the fabrication of large pieces of equipment such as wind turbine blades. However, their manufacturing process remains difficult to follow in real time. In particular, the liquid resin infusion process, widely used for the creation of large

composite pieces, still requires online monitoring despite being a crucial step for the final properties of the final composite.

Of all the non-destructive methods of characterisation that could be applicable to the monitoring of the said infusion process, dielectric monitoring presents the advantage of being theoretically able to follow the entire procedure, from the filling of the mould with liquid resin to the final solid composite piece. However, the devices currently used to perform dielectric measurements are not suitable for large scale monitoring because of their small size.

The present study aims to help solving this issue by developing a new type of dielectric sensor suitable for the monitoring of the infusion process on a larger scale.

3. Epoxy Resin Characterisation

3.1. Scope and objectives

In this chapter, the cure of the RS-M135 epoxy resin mixed with the fast hardener RS-MH134 provided by PRF Composite Materials is investigated. An overview of the epoxy resin cure mechanism is given and a kinetics model of the cure is discussed. The kinetics study of the resin system during cure can be performed using chemical methods such as liquid chromatography, infrared spectroscopy or FTIR. It can also be achieved via physical methods including differential scanning calorimetry (DSC), dynamic viscometry, thermal scanning rheometry and dynamical mechanical thermal analysis. In the present work, differential scanning calorimetry and dynamic viscometry are used to investigate the kinetics of the epoxy resin curing reaction.

3.2. Cure of epoxy resin

The curing reaction of the epoxy based RS-M135 thermosetting resin involves a crosslinking of the pre-cured polymer chains triggered by the addition of a hardener. The mechanism of this reaction follows a rather complex kinetics behaviour, discussed in the following section.

3.2.1. Mechanism

The denomination “epoxy resin” covers both the viscous, uncured liquid and the solid polymerized material containing epoxy groups shown in Figure 3.1.



Figure 3.1 *Epoxy functional group*

For ease of storage and longer stability, the monomer is usually pre-polymerised using bisphenol-A (Agarwal *et al.* 2017), resulting in the reactive molecule presented in Figure 3.2.

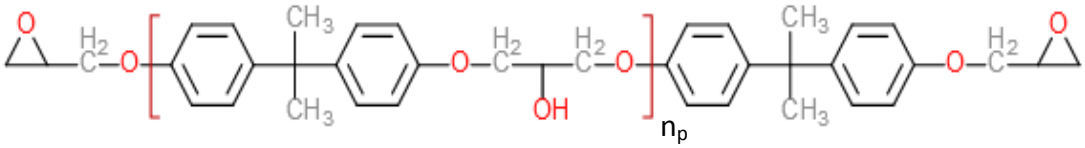


Figure 3.2 *Pre-polymerised epoxy resin with bisphenol A*

The number n_p corresponds to the number of times the motif between the brackets is repeated, called degree of polymerisation. At that stage, the pre-polymer is under a viscous liquid form.

The actual tri-dimensional cross linking reaction resulting in the epoxy resin final properties involves a hardener or crosslinking agent, typically an amine with a functionality $f_{amine}>2$, such as diethylene triamine ($NH_2(CH_2)_2NH(CH_2)_2NH_2$). The amine sites react with the epoxide group, opening the ring by a simple addition mechanism shown in Figure 3.3. This addition reaction is autocatalytic.

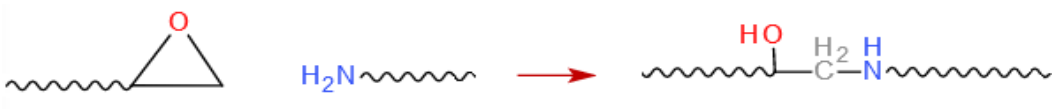


Figure 3.3 *Addition of an amine site to an epoxide group to form a polymer chain*

In the case of diethylene triamine, each molecule presents five reactive sites and thus can react with five pre-polymer chains, resulting in the configuration shown in Figure 3.4.

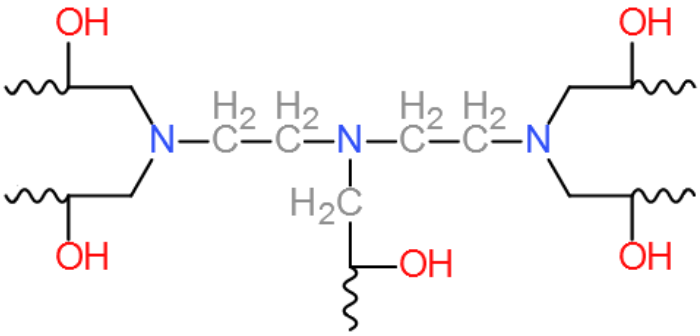


Figure 3.4 *3D grid of epoxy resin cured with a triamine*

Other curing agents containing oxygen or sulphur can be used (Ashcroft 1993).

In the cured state, the epoxy rings have reacted and opened, forming the 3D network that gives the polymer its properties, such as good resistance to chemicals and heat, high adhesive strength, very high glass transition temperature (Tg) or low shrinkage.

As the crosslinking reaction occurs, a thermoset polymer undertakes two important steps, namely the gelation and the vitrification. The gelation of a polymer is defined by the moment the cure reaction is no longer producing one dimensional polymer chains, but rather starting to form a three-dimensional linked network. The vitrification correspond to the point this three dimensional network is sufficiently developed for the viscous liquid to turn into a glassy state. The entire cure reaction encompasses the gelation and vitrification of the polymer resin.

3.2.2. Semi-empirical kinetics models of epoxy resin cure

Curing reaction kinetics can be described by a rate of reaction, function of either the disappearance of reactants or the creations of products. For thermosets, a

degree of cure α corresponding to the consumption of functional groups (here epoxides) is defined. Therefore, (1-α) corresponds to the number of epoxide group left at a set time. A general rate of reaction is then given by (Bilyeu *et al.* 2001):

$$\frac{d\alpha}{dt} = k(1-\alpha)^n \qquad (3.1)$$

where k is the rate constant and n the order of the reaction.

However, this equation only takes into account the concentration of epoxides groups and does not convey the autocatalytic nature of the curing reaction of epoxy resin with a triamine. To account for the autocatalysis, another term needs to be added to the expression, which becomes

$$\frac{d\alpha}{dt} = k\alpha^m(1-\alpha)^n \qquad (3.2)$$

The α^m term represents the autocatalytic nature of the reaction, adding an additional reaction rate with the order of m. If the reaction is not catalytic, m=0 and the equation is simplified to become equation (3.1).

According to the two aforementioned equations, the autocatalytic nature of the curing reaction can be easily determined from experimental data: if the reaction is not autocatalytic, then the reaction rate will be maximal for α=0, at the beginning of the cure. It will then decrease as the polymerisation reaction occurs. However, if the reaction is autocatalytic, then the maximum of the reaction rate will not be observed at the start of the reaction, but rather reached for a higher degree of cure. By plotting the reaction rate versus the advancement and fitting a theoretical equation, the numbers n and m can be determined.

Assuming the constant k follows an Arrhenius law:

$$k = A_k e^{-\frac{Ea}{RT}} \qquad (3.3)$$

where A_k is the pre-exponential function, Ea the activation energy of the reaction, R the perfect gas constant and T the absolute temperature in kelvin. Equation (3.2) becomes:

$$\frac{d\alpha}{dt} = (Ae^{-\frac{Ea}{RT}})\alpha^m(1-\alpha)^n \quad (3.4)$$

Autocatalytic reactions can be triggered by impurities such as water or remaining ions from the resin formulation (Karkanas *et al.* 1996). Therefore, the reaction rate at the beginning of the cure is, in practice, never null. Thus, the reaction rate equation has to be modified to take into account the autocatalytic character of the reaction. To that end, an initial reaction rate independent of the advancement is introduced in equation (3.4) which becomes:

$$\frac{d\alpha}{dt} = (k_1 + k_2\alpha^m)(1-\alpha)^n \quad (3.5)$$

where k_1 is the reaction rate at the start of the reaction and k_2 the rate of reaction for a system without impurities. Those two reaction rates follow the Arrhenius law given in equation (3.3) and k_1 can be theoretically extracted using the reaction rate at α=0. However, this model is often unsuitable to render the entire cure of epoxy resin. In particular, a deviation toward the end of the cure can be observed (Karkanas *et al.* 1996).

Further refining that model and taking into account all the different reactions that can happen during an autocatalytic cure, Horie *et al.* (Horie *et al.* 1970) proposed writing the reaction rate as:

$$\frac{d\alpha}{dt} = (k_1\alpha + k_1')(1-\alpha)(B-\alpha) \quad (3.6)$$

where B is the ratio between amine equivalents to epoxides equivalents. In the case of a perfectly stoichiometric mixture, B=1 and the equation becomes equation (3.5) with m=1 and n=2

Another way to obtain a better fit of the model with the experimental data is to modify equation (3.5) by using two different reactions orders n_1 and n_2 (Karkanas *et al.* 1996). These two reaction rates correspond respectively to the addition of primary and secondary amines on the epoxy group, as discussed in section 3.2.1. In that case, the reaction rate becomes:

$$\frac{d\alpha}{dt} = k_1(1-\alpha)^{n_1} + k_2\alpha^m(1-\alpha)^{n_2} \qquad (3.7)$$

This equation has been successfully applied to model the cure of epoxy/amine resins in the literature (Karkanas and Partridge, 2000). Therefore, unless otherwise stated, it will be assumed that the cure of the RS-M135 epoxy resin follows the model described by equation (3.7).

As mentioned in the introduction of the present chapter, several techniques give access to the kinetics of the cure reaction. In the present study, DSC and dynamic viscometry are used, and will be discussed in the following sections.

3.3. Differential scanning calorimetry

Differential scanning calorimetry (DSC) is used to follow the cure of the RS-M135 epoxy resin and develop a model of the cure for both dynamic heating and isothermal conditions.

3.3.1. Experimental protocol

The DSC experiments were carried out using a PerkinElmer DSC 6000 (www.perkinelmer.co.uk/corporate). It is a single furnace setting DSC similar to the one shown schematically in Figure 3.5.

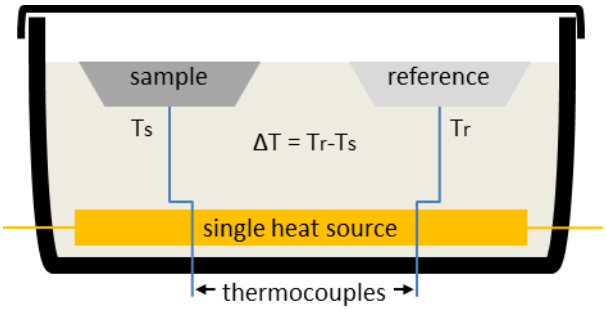


Figure 3.5 *Schematic representation of the DSC chamber*

Special aluminium crucibles were sealed with either the substance under study (in the case of the sample) or air (in the case of the reference) inside. The crucibles were placed in two symmetrical depressions for analysis. Two thermocouples collected the temperature of the sample (T_s) and the reference (T_r) while a single heat source regulated the temperature inside the closed chamber. The temperature difference between the sample side and reference side (ΔT) was measured at all time. Since the sample and reference are subjected to the same temperature profile, the difference between their respective temperatures can be used to determine the energy change due to the exothermic reaction taking place in the sample crucible. That temperature difference was recorded and post processed by the Pyris™ instrument managing software provided by PerkinElmer in order to obtain the heat flow as a function of time.

A temperature and cell calibration was performed before each experiment. The temperature of melting and latent heat of melting of a calibration material sample were recorded and compared to their theoretical values. The difference between

the temperature of melting measured and the theoretical value was stored in the data collecting software for automatic correction of the recordings to follow. The ratio between the measured latent heat of melting and the theoretical value constituted the cell constant and was used to convert the temperature difference into heat flow. In the case of this study, indium was used as the reference material before each run.

To ensure reproducibility of the experimental results, a batch of RS-M135 resin and RS-MH134 hardener was mixed before quickly being divided into weighted samples no heavier than 15 µg. Those samples were sealed into aluminium crucibles and frozen at -18˚C to slow the reaction down almost to a stop. The cooled samples were pulled out of the freezer as needed to perform the DSC analysis.

Two types of experiments were performed on the epoxy resin samples: dynamic runs and isothermal runs. The protocols for each analysis shall be described in the following sections.

3.3.1.1. *Dynamic runs settings*

To perform the dynamic runs, the sample crucible was taken from the freezer, immediately placed in a pre-cooled DSC at either -30˚C or -50˚C and kept for one minute at that temperature before being subjected to a ramp of 4 ˚C/min, 6 ˚C/min, 8 ˚C/min, 10 ˚C/min, 20 ˚C/min or 40˚C/min up to 300˚C. The sample was then kept at 300˚C for one minute before being cooled down to 20˚C at 6˚C/min.

3.3.1.2. *Isothermal*

In the case of an isothermal run, the sample was taken out the freezer, placed in a pre-heated DSC at 10˚C, 15˚C, 20˚C, 25˚C or 30˚C and left to cure for 24 hours.

The results of these experiments are presented in the section below.

3.3.2. Experimental results

3.3.2.1. *Dynamic runs*

When the cure process is analysed using a dynamic setting, that is submitting the sample to different speeds of heating, the physical properties of the resin are affected by several mechanisms simultaneously (Kenny and Trivisano 1991). Typically, the crosslinking process between the monomers and the increase of the resin viscosity are greatly impacted by how quickly the sample is heated. As the resin heats up, its viscosity decreases, allowing the reactive species to move more easily. The reaction rate thus increases.

The main purpose of investigating the cure of epoxy resin using dynamic heating conditions is to determine whether or not the cure mechanism is affected by the heating rate, as well as obtaining the total heat generated by the cure reaction.

The curves obtained for different heating rate of epoxy resin samples prepared with the protocol described in section 3.3.1 are presented in Figure 3.6.

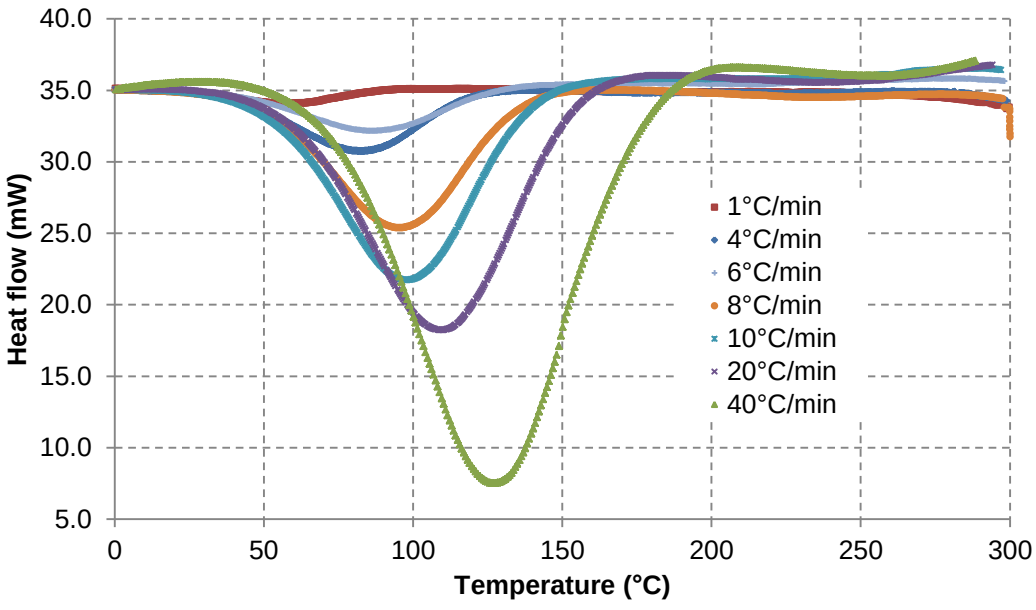


Figure 3.6 *Heat flow in the dynamic cure of RS-M135 epoxy resin*

The heat flow decreases until reaching a minimum point, before increasing and reaching a plateau as the resin approaches the vitrification point. Up to the vitrification point, the mobility of the charged species is possible and improved by thermal agitation. Thus the reaction rate increases with the temperature. After the vitrification point, the formation of the 3D network greatly reduces the mobility of the species, causing the drop in the reaction rate. The minimum of the curves shifts towards higher temperatures as the heating rate increases. The resin used in the present study cures at room temperature. Therefore, when subjected to a low heating rate, the cure happens gradually and the heat released by the exothermic reaction is distributed along the duration of the experiment. When the heating rate increases, the reaction happens quicker and the heat is generated on a smaller time scale, creating a lower minimum at a higher temperature.

Assuming that the heat of reaction is proportional to the advancement of the reaction, or degree of cure α:

$$\alpha(t) = \frac{1}{H_T}\int_0^t \frac{dH}{dt}dt \tag{3.8}$$

where H_T is the total heat flow measured during the dynamic experiments and the integral corresponds to the area under the curve at the instant t.

In the case of a dynamic scanning, it is assumed the system undergoes a complete reaction. In that case, the advancement of the cure α can be linked the total heat of reaction using equation (3.9).

$$\alpha(t) = \frac{H(t)}{H_T} \tag{3.9}$$

where H(t) is the cumulated heat from the start of the experiment to the instant t, and H_T is the total heat of reaction previously determined. Graphically, α

corresponds to the ratio between the area under the curve at instant t over the total area under the curve.

The total heat of reaction is obtained by integrating the area under the curve for the entire reaction. Good reproducibility of the experimental result is observed, as shown in Table 3.1. Different heating rates give a similar total heat of reaction with an acceptable standard deviation. This suggests the reaction mechanism of the resin cure remains the same for heating rates between 1°C/min and 40°C/min. For the rest of the analysis, the average of the obtained heats of reaction will be used in the calculations.

Table 3.1 *Total heat of reaction for the cure of epoxy resin*

Rate (°C/min)	1	4	6	8	10	20	40
Total Heat of reaction (J/g)	366	326	320	366	412	360	330
Average (J/g)				354			
Stan. Deviation				32%			

Figure 3.7 shows the reaction rate as a function of the degree of cure for all the heating rates studied.

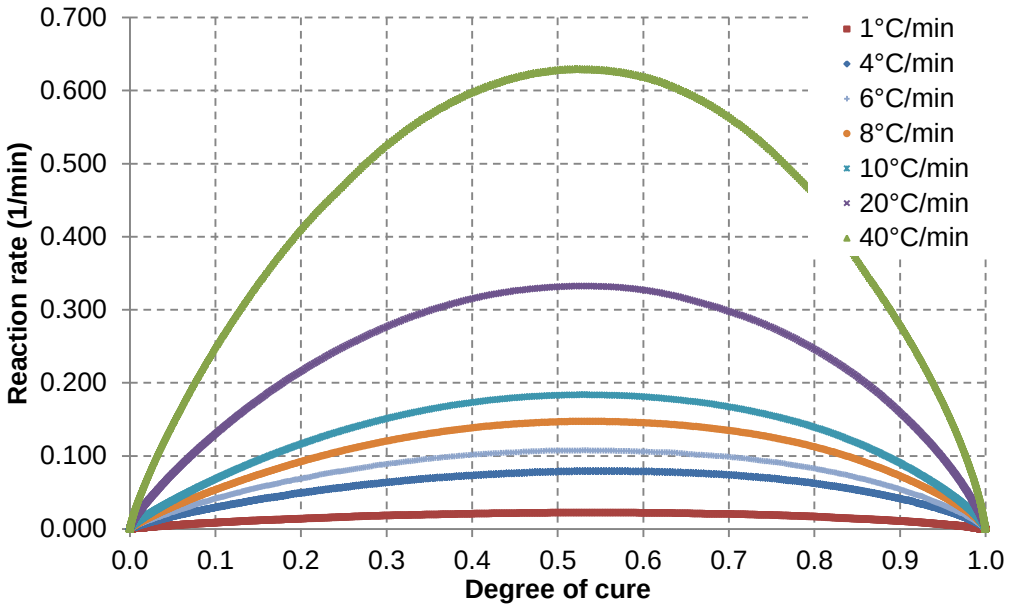


Figure 3.7 *Reaction rate in the dynamic cure of RS-M135 epoxy resin at constant heating rates*

For a given degree of cure, the higher the heating rate, the higher the reaction rate. As mentioned before, if the system is heated rapidly, the reaction will take place quicker. Moreover, the reaction rate reaches a maximum at a fixed degree of cure, as shown by Table 3.2.

Table 3.2 *Temperature and conversion at maximum reaction rate*

rate (°C/min)	Maximum dα/dt (min^{-1})	Temperature at max dα/dt (°C)	Degree of cure at max dα/dt
1	$2.25x10^{-2}$	55.8	53%
4	$7.91x10^{-2}$	82.6	57%
6	$1.07x10^{-1}$	87.1	53%
8	$1.47\ x10^{-1}$	95.1	53%
10	$1.84\ x10^{-1}$	97.5	53%
20	$3.32\ x10^{-1}$	110.1	53%
40	$6.29\ x10^{-1}$	127.0	52%

Independently of the heating rate, the maximum reaction rate is reached for a constant degree of cure, around 53%. This indicates the reaction mechanism of the resin cure reaction, despite being affected by temperature, is independent of the heating rate. The different parameters of equation (3.7) are thus independent of the heating rate and can be calculated to provide a model fitting the experimental data in the range studied.

3.3.2.2. *Isotherms*

The cure of the resin was investigated at 10˚C, 15˚C and 25˚C. The curves showing the reaction rate of the cure versus time for these three temperatures are given in Figure 3.8.

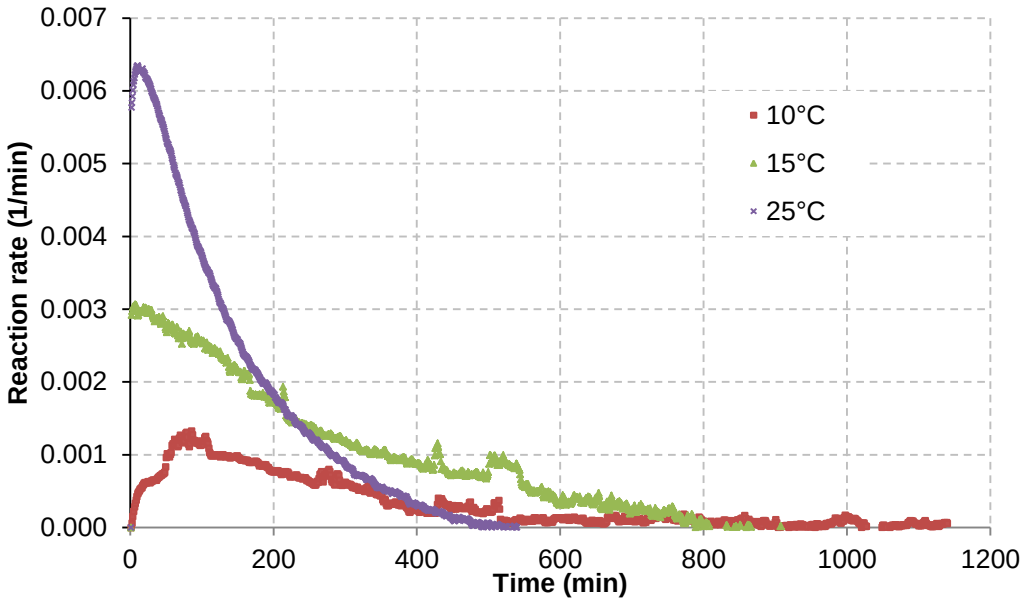


Figure 3.8 *Reaction rate versus time for RS-M135 epoxy resin under isothermal conditions*

For the experiments at 10˚C and 25˚C, the reaction rate starts by increasing, before reaching a maximum and decreasing until a value close to zero. The curve obtained at 15˚C presents a maximum at the beginning of the experiment before decreasing. This is likely due to the preparation and the storage of the samples. As described in section 3.3.1, a batch of resin was mixed and divided between several crucibles. This was not instantaneous and the resin had time to react before the reaction was put to a halt by freezing the samples. Therefore, the cure reaction had already started before the samples were put in the freezer.

As discussed in section 3.2.2, the reaction rate is not maximal at the beginning of the reaction, indicating the autocatalytic nature of the reaction. Higher temperatures of cure lead to a higher maximum value of the reaction rate, confirming the reaction is temperature dependant.

The curves showing the reaction rate versus degree of cure are shown in Figure 3.9. For all the temperatures tested, the reaction reaches a maximum and decreases with the advancement of the reaction. None of the curves reach a degree

of cure equal to one, indicating that the reactions are not complete at the end of the experiment. However, it is verified that curing the resin at higher temperatures results in a higher degree of cure for the same length of time.

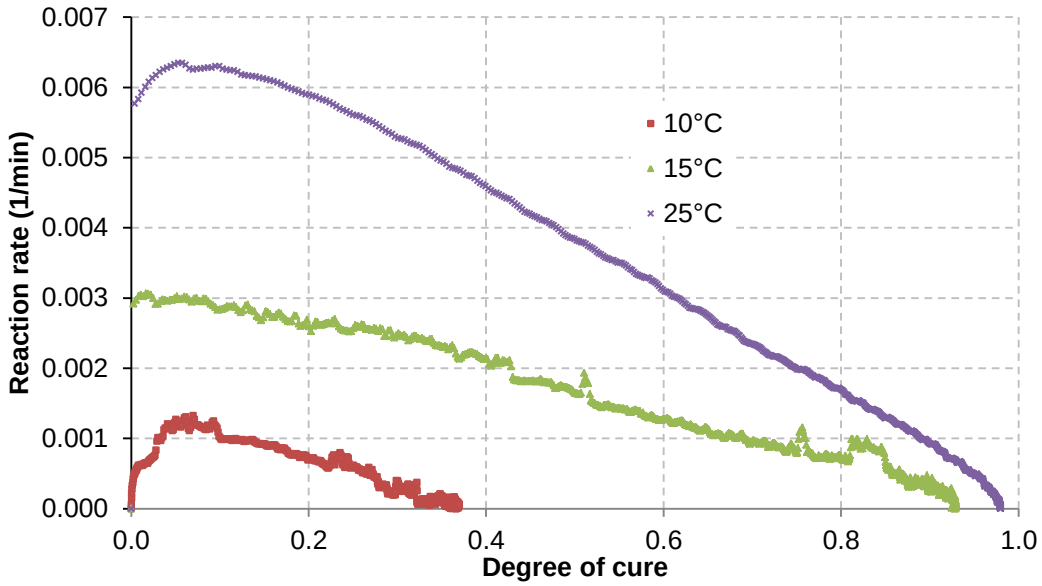


Figure 3.9 *Reaction rate versus degree of cure for RS-M135 epoxy resin under isothermal conditions*

The curves shown in Figure 3.10 confirm the incomplete nature of the reaction for all temperatures at the end of the experiment. The evolution of the final degrees of cure with time reaction is given in Table 3.3.

Table 3.3 *Final degrees of cure of RS-M135 epoxy resin under isothermal conditions for 24 hours*

	10˚C	**15˚C**	**25˚C**
Final degree of cure	37%	92%	99%

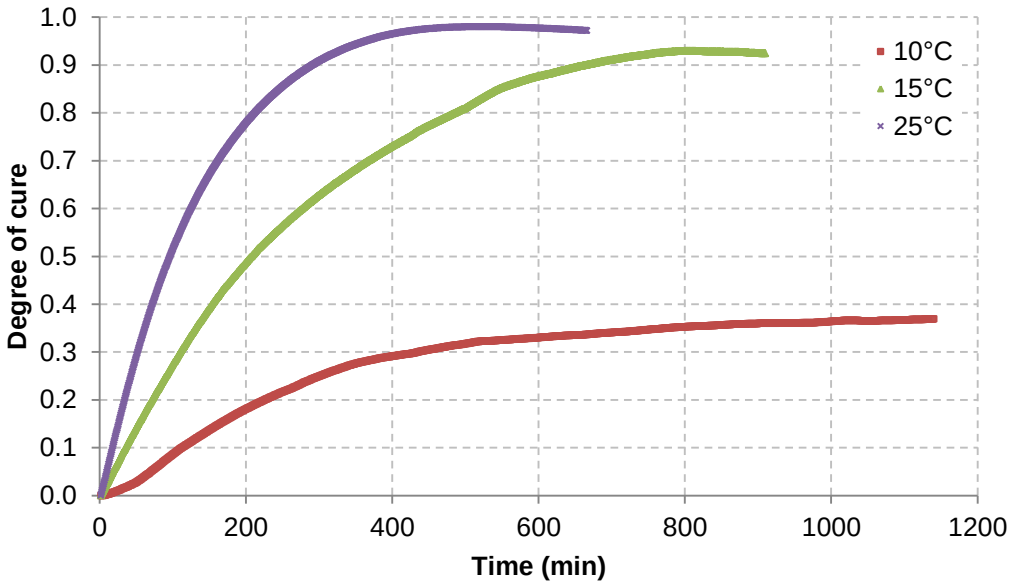


Figure 3.10 *Degree of cure versus cure time for RS-M135 epoxy resin under isothermal conditions*

The final degree of cure for the resin treated at 25˚C is however very close to 100%. The resin manufacturer indicates a complete cure of the resin after 24 hours, but encourages a postcure treatment of the final piece to improve its mechanical properties. This is achieved by reheating the cured resin at temperatures between 40 -150˚C for up to 24 hours (PRF Composite Materials, 2015b). This additional step ensures a full cure of the resin and thus enhanced mechanical properties.

3.3.3. Kinetics model

Using the experimental data presented in the previous sections, the kinetics model discussed in section 3.2.2 was fitted to the epoxy resin studied by means of the solver tool in Excel. The absolute error was calculated between each value of the heating rate recorded experimentally and the heating rate calculated using the mathematical model. The sum of those errors was minimised using the GRG Nonlinear method with a convergence of 0.0001 in the solver tool.

3.3.3.1. *Dynamic*

By fitting the results presented in Figure 3.6, it was possible to determine the parameters for equation (3.7). They are presented in Table 3.4 and the comparison of the curves obtained with the model and the experimental results are given in Figure 3.11.

Table 3.4 *Calculated parameters of the kinetics model for the dynamic cure of RS-M135 epoxy resin at constant heating rates*

A_1 (min^{-1})	E_1 ($J.mol^{-1}$)	A_2 (min^{-1})	E_2 ($J.mol^{-1}$)	n_1	n_2	m	Average fitting error
290247	443797.5	1000069	44441.0	0.227	1.193	0.36	44%

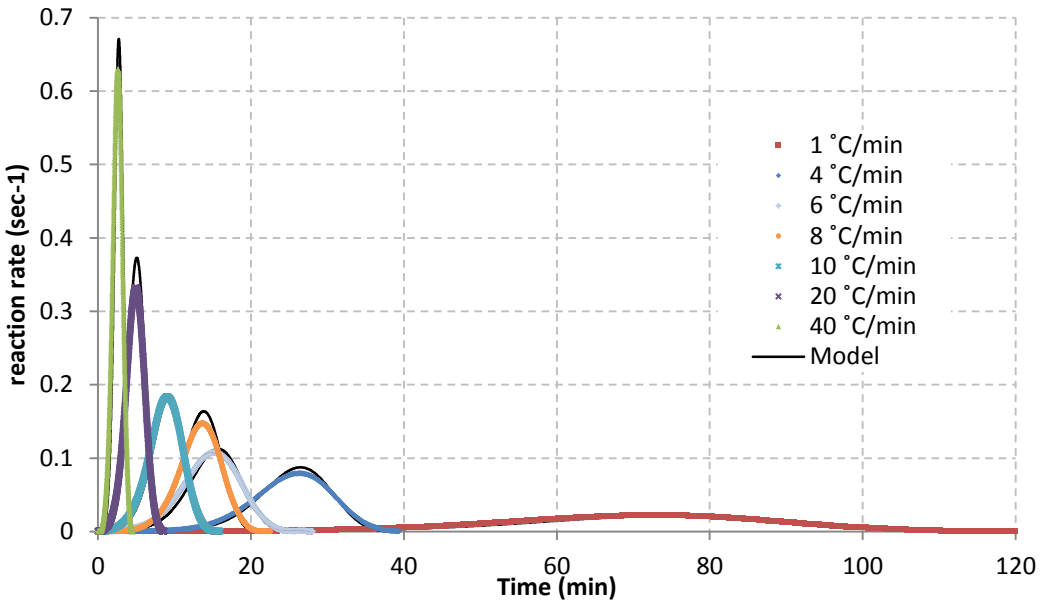


Figure 3.11 *Fit of the kinetics model for the dynamic cure of RS-M135 resin*

According to those results, the chosen parameters are suitable to model the cure of the resin for heating rates between 1˚C/min to 40˚C/min.

3.3.3.2. *Isotherms*

The results of the isothermal experiments are used to find another set of parameters suited to model the isothermal cure of the RS-M135 resin with equation (3.7). The new sets of parameters are presented in Table 3.5.

Table 3.5 *Calculated parameters of the kinetics model for the isothermal cure of RS-M135 epoxy resin*

A_1 (min^{-1})	E_1 ($J.mol^{-1}$)	A_2 (min^{-1})	E_2 ($J.mol^{-1}$)	n_1	n_2	m	Average fitting error
290247	443797	1000069	44441	0.23	1.87	0.5	45%

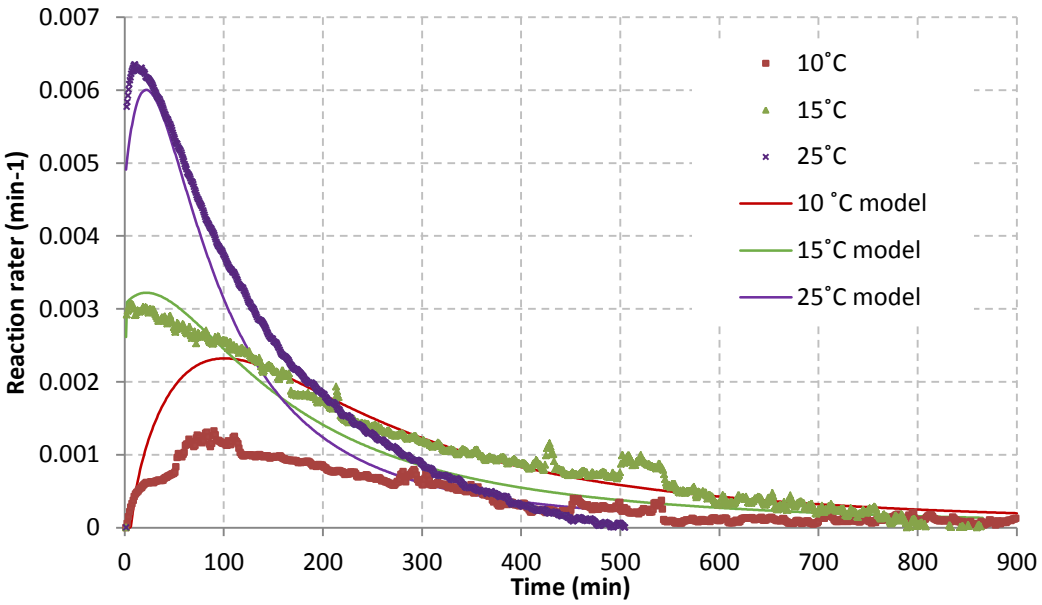


Figure 3.12 *Fit of the kinetics model for the isothermal cure of RS-M135 resin*

The modelled curves obtained, presented in Figure 3.12, show a good fit with the experimental data at 15˚C and 25˚C. However, the curve obtained at 10˚C presents quite a large discrepancy with the one obtained using the mathematical model. In the mathematical model, the temperature and degree of cure are considered ideal,

which is not representative of the reality during the experiment. This is especially true when extreme values of temperatures or heat rate are used, thus leading to more divergences between the experimental values and calculated ones.

3.3.3.3. *Summary*

Investigating the cure of the RS-M135 epoxy resin under dynamic heating and isothermal conditions confirmed the autocatalytic nature of its cure reaction. A model of the cure kinetics was fitted to both dynamic heating settings and isothermal cure. A discrepancy between the set of parameters obtained for the isothermal cure and the dynamic cure is observed, but this is likely due to experimental errors on the isothermal data. It is likely that better isothermal curves would have provided a set of parameters close enough to the dynamic ones to consider a single fitting model for both experimental settings. The model developed for isothermal cure shall nonetheless be used in section 3.5 to determine the degree of cure at gelation, as well as in chapter 6 for the interpretation of the dielectric sensor prototype response.

3.4. Rheology of the RS-M135 epoxy resin during cure

In their uncured state, thermosetting resins are viscoelastic materials exhibiting properties of non-Newtonian fluids (Franck 2004). During cure, the polymer chains grow and a three dimensional crosslinking reaction takes place between the long polymer chains, as explained in 3.2.1. Because chains have less and less mobility as the reaction progresses and the three dimensional network forms, the viscosity of the resin increases continuously until the material becomes solid. It is thus possible to follow the cure of a resin by following the variation of its viscosity with time (Kenny *et al.* 1990; Lapique and Redford 2002). When the crosslinking of the long polymer chains becomes prevalent over the mobility of the said chains, the polymer reaches its gel point and an abrupt increase in viscosity is observed. The sudden

increase in viscosity marks the onset of gelation, the actual gelation taking place a few minutes after the sudden change in viscosity (Karkanas and Partridge 2000).

The dielectric properties of epoxy resins are closely linked to their viscosity. Therefore, investigating the changes in the viscosity of the resin as it cures provides valuable information that shall be later linked to the dielectric sensor prototype results.

3.4.1. Experimental protocol

The investigation of the RS-M135 thermoset epoxy resin was done using a controlled strain experiment. A rotational oscillatory shear test was performed on the epoxy resin during its cure using a Malvern Bohlin Gemini Nano rheometer. The curing resin was placed in a 150 micron gap between two disposable circular parallel plates of a diameter 25 mm, as shown schematically in Figure 3.13. In order for the curing reaction to start at the beginning of the experiment, the resin and hardener were mixed right before a few drops were put between the plates. The distance between the plates was then set at 150 microns and the excess resin at the edge of the plates was cleaned with a spatula. The system was either left at room temperature or placed in a small crucible to control the ambient temperature. The recording of the measurements was started, the setting of the parameters and data collection being achieved by the mean of the Bohlin R65103 software provided with the rheometer.

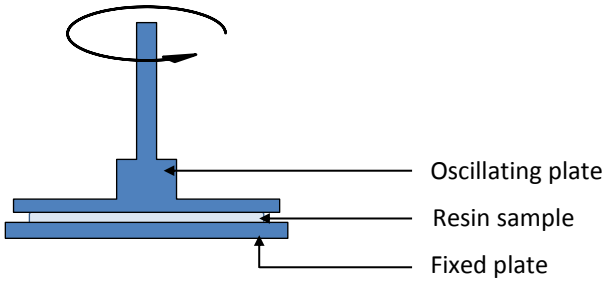


Figure 3.13 *Geometry of the oscillatory shear test*

During the test, the sample was exposed to a fixed sinusoidal strain γ (or displacement) of 0.001 with an angular frequency of 1 Hz. The torque, or stress σ_v transmitted to the fixed plate was monitored as the resin cured and its viscosity increased.

In the linear domain of the polymer viscoelasticity (small displacement), the storage modulus, the viscosity of a material is defined as the ratio between the force (stress) to the deformation rate (shear) (Deshpande 2009).

$$\eta = \frac{\sigma_v}{\dot{\gamma}} \tag{3.10}$$

Assuming a sinusoidal strain:

$$\gamma = \gamma_0 \sin(\omega t) \tag{3.11}$$

where γ_0 is the amplitude of the stain and ω the angular frequency of the excitation, the stress is expressed by:

$$\sigma_v = \sigma_{v0} \sin(\omega t + \delta_v) = \gamma_0 (G'(\omega) \sin(\omega t) + G''(\omega) cos(\omega t)) \tag{3.12}$$

where ω is the frequency of the excitation, σ_v the stress, γ the strain and δ_v the phase between stress and strain. G' is the elastic modulus and G'' is the loss modulus. The complex viscosity of a material is linked to these quantities by the relations:

$$|\eta^*| = \sqrt{(\eta')^2 + (\eta'')^2} \tag{3.13}$$

$$\eta' = \frac{G''}{\omega} \tag{3.14}$$

$$\eta'' = \frac{G'}{\omega} \tag{3.15}$$

G' corresponds to the energy that the viscous system is able to store and resituate, while G'' is the energy dissipated due to the friction of the viscous

medium. Thus, the elastic modulus dominates in the case of solid materials, while viscous liquids are governed by the loss modulus. The loss factor $\tan\delta = \frac{G''}{G'}$ translates the viscous character of the material tested. When tanδ<1, the loss modulus prevails and the material is considered a viscous liquid. When tanδ>1, the material behaviour verges towards that of a solid.

During the resin cure, its behaviour evolves from viscous liquid to glassy solid. Therefore, the evolution of the elastic and viscous modulus gives indications about the advancement of the crosslinking reaction and can be used to characterise the cure of the system.

3.4.2. Experimental results

In order to investigate the viscosity variations of the RS-M135 epoxy resin during cure, two temperatures of cure (ambient and 40˚C) were tested. The two experiments were carried out using the protocol presented in section 3.4.1.

3.4.2.1. *Ambient temperature cure*

The elastic modulus (G'), viscous modulus (G'') and loss factor (tan δ) recorded during the cure of epoxy resin at 20.8 ˚C are shown in Figure 3.14.

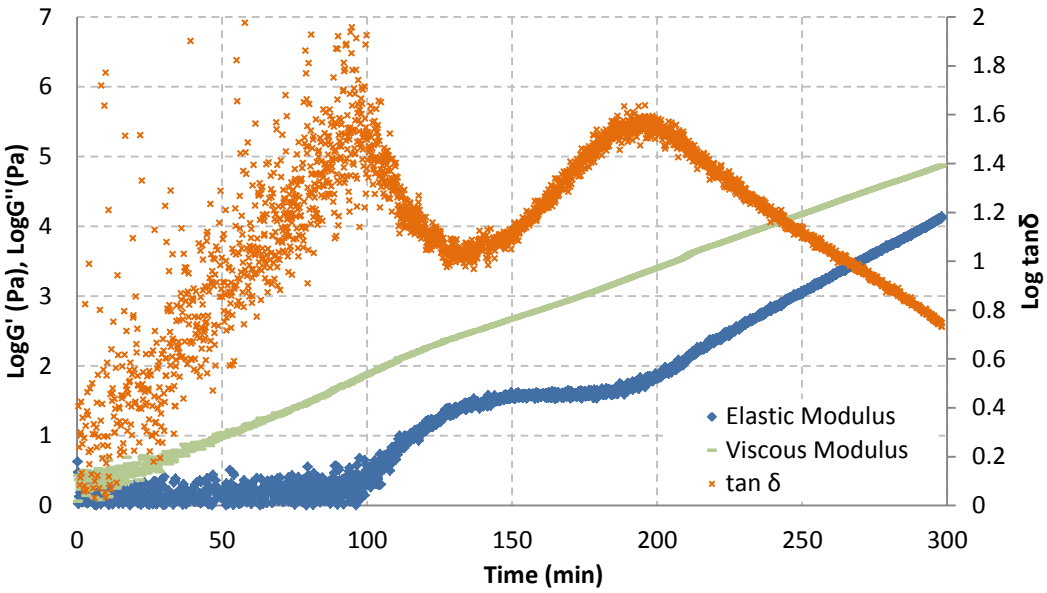


Figure 3.14 *Evolution of the elastic modulus (G') and viscous modulus (G'') versus time during the cure of RS-M135 epoxy resin at T=20.8 ˚C and f=1Hz*

At the beginning of the cure, the signals for all the quantities are very noisy. According to the data provided by the resin manufacturer, the uncured mixture of resin and hardener has a viscosity of around 200 mPa at room temperature, which is too low for the apparatus detection range. In the case of the viscous modulus, the noise diminishes around 50 minutes. The elastic modulus stabilises around 110 minutes after the start of the recording.

The viscous modulus curve exhibits an almost linear increase from 2 Pa to $7.4x10^4$ Pa after 300 minutes of reaction. Around 125 minutes after the start of the experiment, a small shoulder in the curve is observable. A corresponding shoulder is clearly visible at the same time on the elastic viscosity curve.

After the initial scattered measure points around 1 Pa, the value of the elastic viscosity starts to increase 100 minutes after the start of the experiment. It reaches a plateau of 40 Pa between 145 and 185 minutes. Afterwards, the curves exhibit a linear increase up to $1.4x10^4$ Pa at the end of the experiment.

The loss factor presents two maximums: one is observable around 100 minutes, when the value of the elastic modulus becomes high enough to be recorded by the rheometer. The second maximum takes place around 180 minutes, when the slope of the elastic modulus changes.

According to Tung and Dyne, (Tung and Dynes 1982) the gel point of the resin can be estimated using the viscous and elastic modulus curves. In the liquid state of the resin, the viscous properties of the resin dominates, translating to G''>G'. As the resin cures and the 3D network starts to appear, the resin solidifies, its elastic response takes over the viscous one and G'>G''. Therefore, the time at which the viscous modulus and elastic modulus curves intersect is a good estimate of the gel point of the resin. The intersection point is not visible on the experiment at ambient temperature due to the limitation in recording time; however, it is possible to extrapolate the curves for the viscous and elastic modulus, as shown in Figure 3.15.

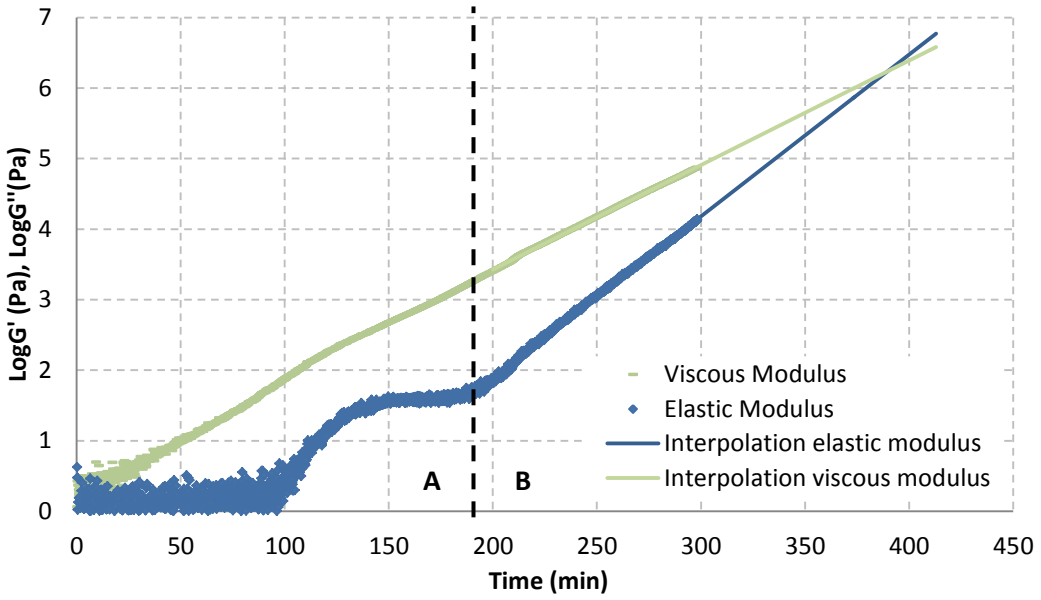


Figure 3.15 *Evolution of the elastic modulus (G') and viscous modulus (G'') versus time during the cure of RS-M135 epoxy resin at T=20.8 ˚C and f=1Hz, extrapolated. A-pregel stage, B-stage of gelation*

With the help of this extrapolation, the gel time at room temperature is determined to happen around 390 minutes after mixing. However, this method of determining the gel time is dependent on the test frequency (Tung and Dynes 1982) and may not be accurate for all systems. Matějka (Matějka 1991) proposed that the gel point corresponds instead to a sharp change in the slope of the elastic modulus curve. According to this theory, Figure 3.15 can be divided into two regions, A and B.

Region A corresponds to a pre-gel stage of the resin. The cure reaction generates long 1D chains, increasing the molecular weight of the polymer. Because of this growing molecular weight, the real viscosity increases and therefore so does the viscous modulus, as shown by equation (3.14).

In region B, the 1D polymer chains start to crosslink and form the 3D network. This region corresponds to the gel formation, and the elastic modulus increases rapidly as the resin solidifies.

The gel point of the polymer is thus determined using the second maximum of tanδ, shown in Figure 3.14. For the RS-M135 resin cured at 20.8 ˚C with the fast hardener RS-MH134, it corresponds to 188 minutes after mixing. This gel point provides the very end of the practical limit for industrially processing the resin before it becomes too viscous.

In reality, the manufacturer recommends a pot life of maximum 30 minutes after mixing the resin with the hardener for best results in infusion processes.

3.4.2.2. *40 ˚C cure*

The same experiment was repeated, this time keeping the temperature of the resin at 40 ˚C. The curves obtained are shown in Figure 3.16.

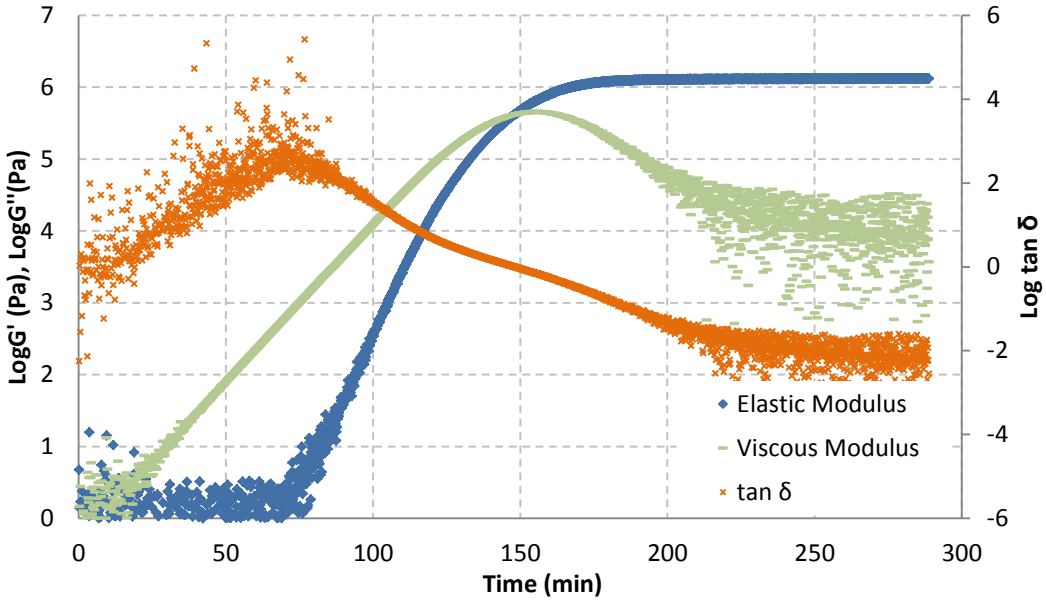


Figure 3.16 *Elastic modulus, viscous modulus and complex viscosity versus time during the cure of RS-M135 epoxy resin at 40 ˚C*

Similarly to the previous experiment, the signals for all the grandeurs are noisy at the beginning of the recording. In the case of the viscous modulus, the noise diminishes around 25 minutes, while it takes around 80 minutes for the elastic modulus. The viscous modulus curve exhibits a lot of scattering after 200 minutes, due once again to the apparatus detection limits. When the resin reaches its solid state, the rheometer still gives a false value to the complex viscosity despite the latter being above the upper detection levels of the apparatus.

The viscous modulus curve exhibits a linear increase from 2 Pa to a maximum of 4.4×10^5 Pa at 155 minutes. The elastic modulus linearly increases from 1 Pa at 70 min to a final value plateau of 1.3×10^6 Pa around 175 min. No shoulder is visible on any of the curves.

The change in the slope of the elastic modulus curve is not observable at that temperature. It is assumed that the resin reacts too rapidly at 40 ˚C for the signals to be stable enough at the time gelation occurs. This confirms that a higher temperature of cure leads to a faster reaction.

Studying variations of the elastic and viscous modulus of the epoxy resin during cure provides an overview of the reaction profile. The experiment at room temperature gives an estimate of the gel point that might be observable on the dielectric curves as well. That profile shall be compared with the results obtained with the dielectric sensor prototypes in chapter 6.

3.5. Rheology and DSC experiments comparison

The rheometry and DSC analysis of the resin provide complementary information on the cure mechanism of the RS-M135 resin.

Using the isothermal model developed in section 3.3.3.2, the theoretical degree of cure of the resin versus time at 20.8˚C is calculated. It is plotted with the results of rheometry measurements at the same temperature in Figure 3.17.

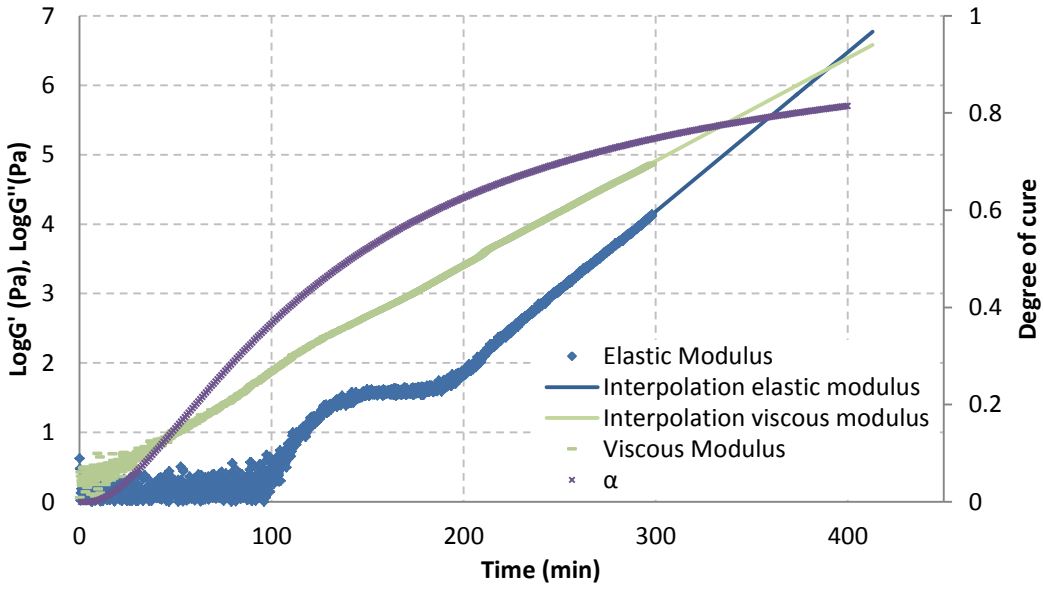


Figure 3.17 *Variations of the Elastic modulus, viscous modulus and degree of cure of the RS-M135 epoxy resin at 20.8˚C*

The gel point obtained by using the change in the elastic modulus slope corresponds to a degree of cure of 58%, which is more in accord with the microscopic explanation of the gelation phenomena than the degree of cure of 81%

found by using the intersection between the curves of the elastic and viscous modulus. Gelation, corresponding to the point the 1D polymer chains are starting to create the final 3D network, is unlikely to take place near the end of the polymerisation reaction. The glass transition is expected at the end of the cure, marking the passage of the epoxy from a viscous medium to a glassy solid.

Using the kinetics model, the degree of cure is calculated as a function of time for an isothermal experiment at 40˚C. The model obtained is superimposed to the curves of the dynamic viscometry experiment at the same temperature in Figure 3.18.

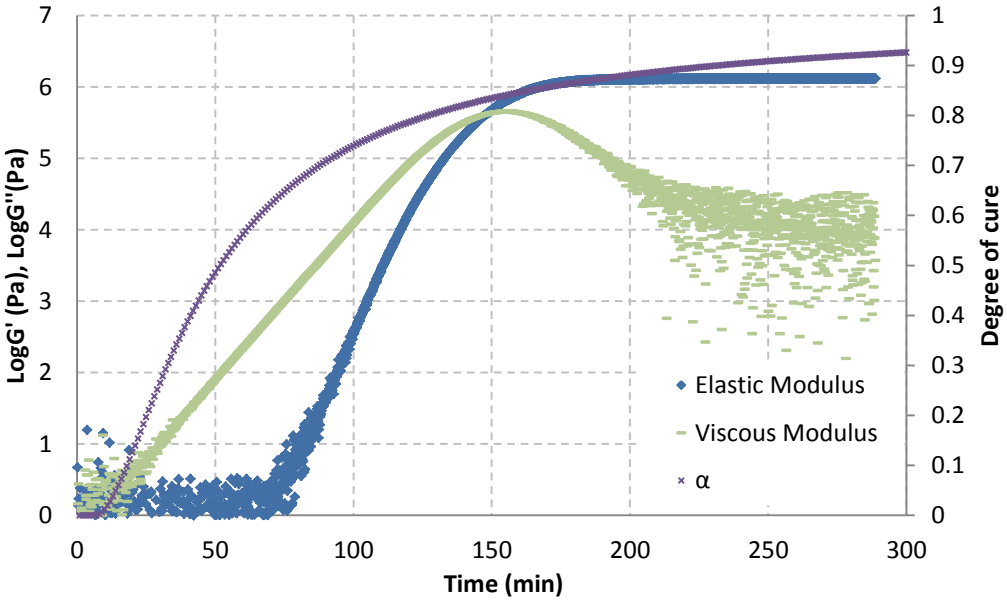


Figure 3.18 *Variations of the elastic modulus, viscous modulus and degree of cure of the RS-M135 epoxy resin at 40˚C*

At 40˚C, the kinetics model indicates that the degree of cure reaches 58% one hour after mixing. Assuming that gelation happens at a set degree of cure, the gel point occurs while the elastic modulus is still very noisy, preventing the observation of the change in the elastic modulus slope.

The gel point of epoxies depends on the volume of the resin investigated during cure. Considering that the polymerisation reaction is exothermic, more material will produce more heat and therefore speed up the cure, whereas less material will cure more slowly. Moreover, the results obtained with the aforementioned viscometry experiments are likely to be incorrect: not only does finding an acceptable gel time require a different interpretation of the modulus curves than the one typically used for industrial grade epoxies, but the manufacturer indicates a pot life of 30 minutes (PRF Composite Materials, 2015b), which should be relatively close to the gel point.

Using the standard gelation theory of Flory (Flory, 1953), the degree of cure at the gel point α_{gel} is given by:

$$\alpha_{gel} = \frac{m_{amine} f_{amine}}{m_{epoxy} f_{epoxy} (f_{amine} - 1)(f_{epoxy} - 1)} \quad (3.16)$$

where m_{amine} and m_{epoxy} are respectively the moles of amine and epoxy reacting, and f_{amine} and f_{epoxy} are the functionalities of the said amine and epoxy. Assuming the reactants are introduced in stoichiometric proportions,

$$m_{amine} f_{amine} = m_{epoxy} f_{epoxy} \quad (3.17)$$

and thus equation (3.16) becomes:

$$\alpha_{gel} = \frac{1}{(f_{amine} - 1)(f_{epoxy} - 1)} \quad (3.18)$$

Using the values of f_{amine}=3 and f_{epoxy}=2 provided by the manufacturer (PRF Composite Materials, 2015b), the advancement of the cure at gel point is theoretically equal to 50%. Therefore, the value of 58% found experimentally shall be used as the advancement at gel point for the rest of the present work.

3.6. Chapter Summary

In this chapter, the cure of the RM-S135 resin mixed with the fast hardener RS-MH134 was investigated by way of rheometry and differential scanning calorimetry.

The DSC experiments validated the autocatalytic nature of the resin cure reaction, and lead to the development of a cure kinetics model for both dynamic testing conditions and isothermal cure of the resin. In the present study, the resin investigated is cured at room temperature, but it is seldom the case in industry. Typically, the resin system is heated after infusion in order to achieve a quicker reaction. The developed models can therefore be used as a predictive tool for the behaviour of the resin in the case of a modification of the cure temperature.

The data provided by the rheology measurements indicated that the gel point of this resin should be determined using the change in the slope of the elastic modulus rather than the crossover of the elastic and viscous modulus curves. This gel point was found to happen three hours after the mixing of the resin with the hardener for an experiment at room temperature.

The results obtained in that chapter shall be compared to the experimental results provided by the new dielectric sensor prototypes presented in chapter 5 and chapter 6.

4. Theory of Dielectric Monitoring

4.1. Scope and objectives

In this chapter, the principles behind dielectric monitoring are briefly explained before focusing on the different phenomena responsible for the dielectric behaviour of thermoset resins. Electrical circuit equivalences for those phenomena are examined before presenting a simple electrical equivalent circuit for the sensor prototypes and their surroundings.

4.2. Dielectric monitoring principle

As described in section 2.3.1, dielectric monitoring requires a sample of material placed in contact with two (or more) electrodes. A time-varying, typically sinusoidal voltage is applied, creating an electric field in the material investigated. This electric field generates a resulting time-varying current in the material, which is recorded. The induced current results from two main phenomena taking place in the bulk of the material investigated: conduction and polarisation. These two mechanisms will be described later in section 4.3. Because both of those phenomena are greatly affected by the cure reaction of a thermoset, the resulting current varies significantly during the process, thus providing a way to follow the curing reaction. The sinusoidal excitation voltage and resulting current can be expressed as:

$$v(t) = V_0 \sin(\omega t) \quad (4.1)$$

$$i(t) = I_0 \sin(\omega t + \varphi) \quad (4.2)$$

where V_0 an I_0 are the amplitudes of the voltage and current respectively, ω is the angular frequency of the signal and φ the phase between the voltage and current.

By using complex notation, the voltage and current expressions become:

$$V^* = V_0 e^{j\omega t} \quad (4.3)$$

$$I^* = I_0 e^{j(\omega t + \varphi)} \quad (4.4)$$

The admittance is then defined by :

$$Y^* = \frac{I^*}{V^*} = Y' + jY'' \quad (4.5)$$

$$Y^* = \frac{I_0}{V_0} e^{j\varphi} = \frac{I_0}{V_0}\cos(\varphi) + j\frac{I_0}{V_0}\sin(\varphi) \quad (4.6)$$

The real and imaginary parts of Y* are thus:

$$Y' = \frac{I_0}{V_0}\cos(\varphi) \quad (4.7)$$

and

$$Y'' = \frac{I_0}{V_0}\sin(\varphi) \quad (4.8)$$

respectively.

I_0 and φ are frequency dependent (Senturia and Sheppard Jr 1986), thus the admittance measured depends on the frequency of the excitation signal.

4.3. Theory of dielectric monitoring thermosets

As discussed in section 2.3.1, thermosets resins such as epoxies are low loss material reacting to electric fields. They can be characterised by their complex relative permittivity ε* = ε'-jε''. This permittivity is a sum of the contributions of several phenomena taking place when the resin is subjected to an electric field. They are presented in this subsection.

4.3.1. Charge migration

Charged species mobile enough to react to the electric field applied are present in the epoxy resin. They can be ions remaining from the manufacture of the resin precursors or charged species due to the polymerisation process described in 3.2.1. Charges from the hydrogen bonds of the final cured 3D network can also be considered as a contribution to the conductivity of the curing resin (Mijovic and Fitz 1998). Those charged species are able to move in the bulk of the material when an electric field is applied, dissipating the energy through movement. Assuming an electric field E, the velocity of the charged species is proportional to E by a factor u called mobility:

$$v_i = uE \tag{4.9}$$

where v_i is the velocity of the charged species, u its mobility and E the electric field applied.

The contributions of the different species present in the resin are cumulative and thus, the overall conductivity can be expressed as (Senturia and Sheppard Jr 1986):

$$\sigma = \sum_i q_i N_i u_i \tag{4.10}$$

where σ is the measured conductivity of the resin, q_i the charge, N_i number of the charge carrier per unit of volume and u the mobility of the species i. It is assumed that the conductivity of epoxy resin is mainly due to free chloride and sodium ions resulting from the monomer fabrication (Fava and Horsfield 1968; Senturia and Sheppard Jr 1986).

The ion migration phenomenon is dominant at low frequencies, where ions have time to move through the bulk of the material. It is responsible for the main contribution to the permittivity of the resin at those frequencies. That contribution is expressed by:

$$\varepsilon'_{ion} = 0 \tag{4.11}$$

$$\varepsilon''_{ion} = \frac{\sigma}{\omega \varepsilon_0} \tag{4.12}$$

where σ is the conductivity of the resin, ω is the angular frequency of the excitation signal and ε_0 is the permittivity of free space.

In addition to the conduction phenomenon, two types of polarisation contribute to the permittivity of the material. They are described in the following sections.

4.3.2. Electrode polarisation

Electrode polarisation is a local phenomenon due to a difference in the transfer rate of charges between the bulk of the material and the interface with the sensor electrodes. Because the exchange of charges between the electrode and the resin is slower than the migration rate of the charged species from the bulk of the material to the electrode, the said species accumulate near the electrode of opposed polarity and form a charged layer in the vicinity of it. This charged area close to the electrode is called “double layer” and represented by d_b on Figure 4.1.

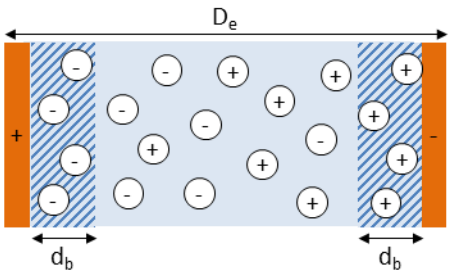


Figure 4.1 *Illustration of the electrode polarisation phenomenon*

The polarisation phenomenon is observable when the frequency of the excitation signal is low enough to allow the migration of the ions through the medium towards the electrodes.

According to the model developed by Day *et al*. (Day *et al.* 1985), the contribution of the electrode polarisation to the permittivity of a parallel plate capacitor is:

$$\varepsilon'_{electrode} = \varepsilon'_{bulk}\frac{D_e}{2d_b}\frac{\frac{\varepsilon''_{bulk}}{\varepsilon'_{bulk}} + \frac{D_e}{2d_b}}{(\frac{\varepsilon''_{bulk}}{\varepsilon'_{bulk}})^2 + (\frac{D_e}{2d_b})^2} \quad (4.13)$$

$$\varepsilon''_{electrode} = \varepsilon''_{bulk}\frac{D_e}{2d_b}\frac{\frac{D_e}{2d_b} - 1}{(\frac{\varepsilon''_{bulk}}{\varepsilon'_{bulk}})^2 + (\frac{D_e}{2d_b})^2} \quad (4.14)$$

where ε'_{bulk} and ε''_{bulk} are the real and imaginary part of the complex permittivity of the bulk material, D_e is the distance between the two electrodes, and d_b is the double layer width shown in Figure 4.1.

Because electrode polarisation depends on the accumulation of charges near an electrode, it is closely linked to the mobility and abundance of the said charges. Therefore, as both the mobility and the number of charged species plummet as the

epoxy resin cures due to the formation of the 3D network, electrode polarisation is usually observable at the beginning of the cure and at low frequency.

4.3.3. Dipolar relaxation

Charged species are not the only species affected by the application of an electric field. Dipolar species such as molecules or molecular groups orientate themselves in the direction of the applied electric field. Dipoles can be divided into permanent dipoles and induced dipoles.

Permanent dipoles are species whose asymmetrical geometry results in asymmetrical charge distribution and thus a permanent dipole moment. In the absence of electric field, the dipoles are oriented randomly, but when an electric field is applied, they tend to align their dipole moments with the field lines. When the electric field stops, they return to their original state (see Figure 4.2 a and b). This return can be hindered by the increasing viscosity of the curing resin or the formation of the 3D network. Therefore, some of the energy stored by the dipole is dissipated through the movement of the dipole returning to its initial position, or its potential interactions with other species created during the 3D network formation. In the case of an epoxy resin, the epoxy and amine groups of the reactant, the –NHR groups presents on the intermediate products of the reaction and the –OH and –NH groups forming the final polymer are all permanent dipoles (Gallone *et al.* 2001).

Contrarily to permanent dipoles, induced dipoles do not possess an intrinsic dipole moment in the absence of an electric field. The application of such a field modifies the spatial distribution of their electron cloud (Mijovic and Fitz 1998), creating a dipole moment (see Figure 4.2 c and d). Because their polarisation relies on the movement of electrons rather than the orientation of molecules, this phenomenon is almost instantaneous and does not dissipate energy through the movements of the dipoles.

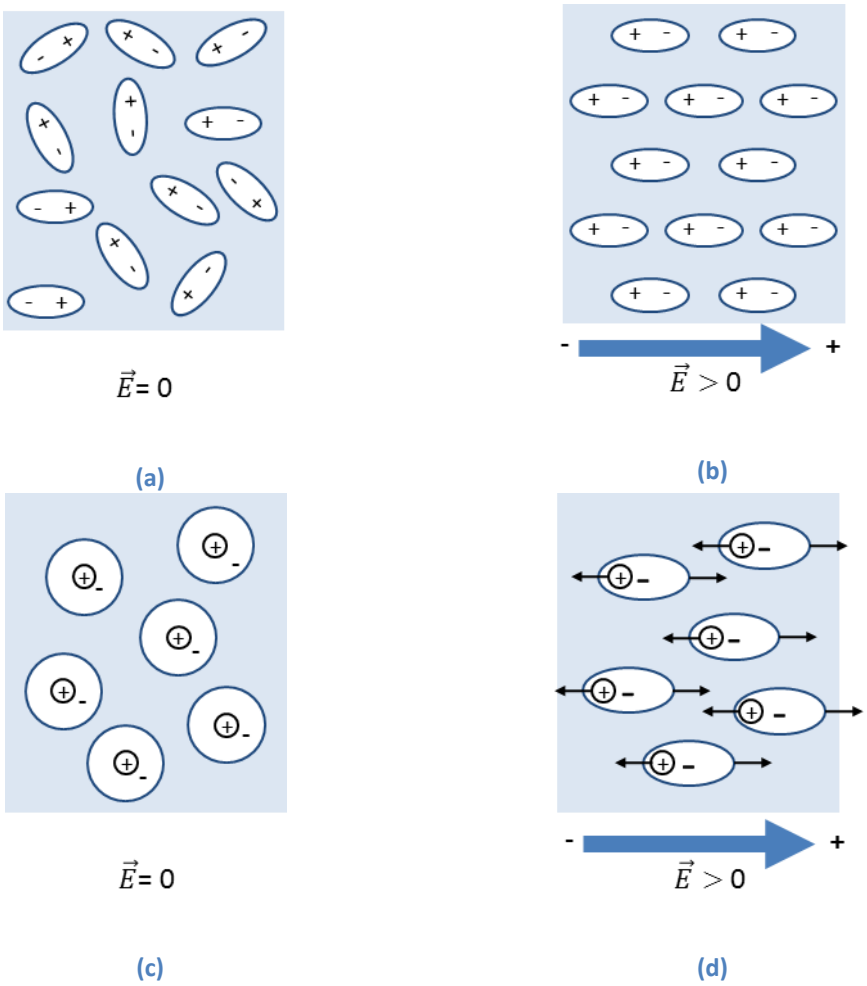


Figure 4.2 *Illustration of the polarisation effect (a) permanent dipoles randomly orientated in the absence of an electric field, (b) permanent dipoles orientated under the application of an electric field (idealised view, in reality, the dipoles tend towards an alignment with the electric field rather than achieve it), (c) induced dipoles in the absence of an electric field and (c) deformation of the electron cloud of induced dipoles in the presence of an electric field*

Using a Debye model for a spherical dipole with a single relaxation time, the contribution of dipoles to the permittivity is given by (Senturia and Sheppard Jr 1986):

$$\varepsilon'_{dipole} = \varepsilon_u + \frac{\varepsilon_r - \varepsilon_u}{1 + \omega^2\tau^2} \tag{4.15}$$

$$\varepsilon''_{dipole} = \frac{(\varepsilon_r - \varepsilon_u)\omega\tau}{1 + \omega^2\tau^2} \tag{4.16}$$

where ε_u is the unrelaxed permittivity at high frequencies, ε_r is the fully relaxed permittivity at low frequencies and τ is the relaxation time of permanent dipoles.

Several relaxation times can be present, depending on the dipoles and their nature. However, the prevalence of the contribution coming from migrating charges to the permittivity makes it difficult to identify, single out and quantify potentially different relaxation times. Therefore, for the rest of this study, an average relaxation time for all dipoles will be assumed as a simplification. This relaxation time is affected by the formation of the 3D network during the resin cure. As the resin solidifies, the network hinders the dipole orientation, especially in the case of big molecules (Senturia and Sheppard Jr 1986). For that reason, the relaxation time increases during cure, and thus the permittivity of the epoxy resin is affected.

4.3.4. Other phenomena

The movement of ions, electrode polarisation and dipole orientation are the three main contributions to the permittivity of epoxy resins. However, if the resin system is heterogeneous, such as containing conductive metallic particles (Tsangaris *et al.* 1998; Psarras *et al.* 2002) or fillers (Senturia and Sheppard Jr 1986), an additional interface polarisation is observable (Mijovic and Fitz 1998). Because of the impurities or additives present in the resin, this phenomenon is actually always present, but its contribution to the permittivity is too small compared to the aforementioned phenomena to be noticeable, especially when ionic conductivity dominates the permittivity (Tsangaris *et al.* 1998).

It is important to note that the permittivity of any material is temperature dependent. Therefore, the temperature should be monitored at all time during dielectric measurements in order to ensure the variations of permittivity observed are caused by the cure of the resin only.

4.3.5. Total permittivity

The effects of the presented contributions to the permittivity of the resin are cumulative and thus the permittivity of epoxy resin is given by:

$$\varepsilon^* = \varepsilon^*_{ions} + \varepsilon^*_{electrode} + \varepsilon^*_{dipole} \tag{4.17}$$

$$\varepsilon' = \varepsilon'_{bulk}\frac{D}{2d_b}\frac{\frac{\varepsilon''_{bulk}}{\varepsilon'_{bulk}} + \frac{D}{2d_b}}{(\frac{\varepsilon''_{bulk}}{\varepsilon'_{bulk}})^2 + (\frac{D}{2d_b})^2} + \varepsilon_u + \frac{\varepsilon_r - \varepsilon_u}{1+\omega^2\tau^2} \tag{4.18}$$

$$\varepsilon'' = \varepsilon''_{bulk}\frac{D}{2d_b}\frac{\frac{D}{2d_b} - 1}{\left(\frac{\varepsilon''_{bulk}}{\varepsilon'_{bulk}}\right)^2 + \left(\frac{D}{2d_b}\right)^2} + \frac{\sigma}{\omega\varepsilon_0} + \frac{(\varepsilon_r - \varepsilon_u)\omega\tau}{1+\omega^2\tau^2} \tag{4.19}$$

The contribution of the electrode polarisation can be minimised by choosing a frequency range high enough to prevent the formation of the double layer. By further assuming that charge migration is prevalent over dipole orientation in the frequency range chosen, $\frac{\sigma}{\omega\varepsilon_0} \gg \frac{(\varepsilon_r-\varepsilon_u)\omega\tau}{1+\omega^2\tau^2}$ and the previous equations simplify to:

$$\varepsilon' = \varepsilon_u + \frac{\varepsilon_r - \varepsilon_u}{1+\omega^2\tau^2} \tag{4.20}$$

$$\varepsilon'' = \frac{\sigma}{\omega\varepsilon_0} \tag{4.21}$$

In the literature, σ is defined as the apparent conductivity and can be qualitatively linked to the degree of cure and viscosity. In thermoset resins, the apparent conductivity is inversely proportional to viscosity before gelation (Mijovic and Fitz 1998). During the cure of the resin, due to the process-induced temperature rise, the viscosity first drops, allowing an increased mobility of the free ions present in it, hence a higher conductivity. However, when the actual cross-linking reaction begins in the polymer resin, the 3D network created increases the

viscosity, reducing the mobility of the ions and leading to an overall decrease in the conductivity.

4.4. Equivalent circuits of the sensor prototype

The dielectric permittivity can be directly correlated to an idealised electrical model circuit composed of macroscopic electric components (Mijovic and Fitz 1998). That equivalence shall be discussed in the following section.

4.4.1. Relation between permittivity and admittance

The complex permittivity of a material is an intrinsic value that cannot be directly measured. For that reason, dielectric monitoring relies on the measure of complex functions called immitance: the admittance Y*, complex impedance Z* or complex modulus M*. The choice of the quantity monitored depends on the phenomena studied. All the immitance functions are linked to each other via the angular frequency ω and the air capacitance C_0 as shown in Table 4.1.

Table 4.1 *Relations between the different immitances* (*adapted from* Macdonald 1987)

	ε*	**Y***	**Z***	**M***
ε*		$\frac{Y^*}{jC_0\omega}$	$\frac{1}{jC_0\omega Z^*}$	$\frac{1}{M^*}$
Y*	$jC_0\omega\varepsilon^*$		$\frac{1}{Z^*}$	$\frac{jC_0\omega}{M^*}$
Z*	$\frac{1}{jC_0\omega\varepsilon^*}$	$\frac{1}{Y^*}$		$\frac{M^*}{jC_0\omega}$
M*	$\frac{1}{\varepsilon^*}$	$\frac{jC_0\omega}{Y^*}$	$jC_0\omega Z^*$	

The main difference between all the presented functions lies in their dependence with frequency. The complex admittance of the system is related by a very simple proportional relation to both the complex dielectric permittivity and the frequency. It shall thus be favoured in the present work.

4.4.2. Equivalent circuits for the different phenomena

The three main contributions to the permittivity described in 4.3 can be modelled by phenomenological electrical circuit analogies. The energy dissipative processes correspond to the behaviour of a resistance while the energy storage phenomenon can be assimilated to a capacitor (Mijovic and Fitz 1998).

4.4.2.1. *Charge migration*

Assuming that charges are moving instantly when submitted to the field, their movement through the material purely dissipates the energy of the electric field, thus corresponding to a simple resistance (Mijović *et al.* 1996):

$$Y^*_{ion} = \frac{1}{R_{ion}} \tag{4.22}$$

4.4.2.2. *Electrode polarisation*

The electrode polarisation phenomenon depends on several factors such as the shape of the electrodes and their surface characteristics, or the resin chemical composition. For that reason, developing a simple electric equivalent is much more difficult than simply using a combination of capacitors and resistances. Focusing on electrode polarisation as a parasitic phenomenon, Feldman *et al.* (2001) reviewed different approaches to representing the electrode polarisation. Their fractal approach, based on the theory that the electrical double layer is self-similar, gives the corresponding admittance:

$$Y^*_{EP} = \frac{(j\omega)^{\nu}}{A(\nu)} = \frac{e^{j\frac{\nu\pi}{2}}\omega^{\nu}}{A(\nu)} \tag{4.23}$$

where ν ϵ [0,1] is the fractal exponent, A is a parameter and ω is the angular frequency, comprised in a certain range where the electrode polarisation self-

similarity hypothesis is valid. This range depends on the electrode geometry and composition. If v=0, the electrode polarisation is a resistance of A(v) Ohm. If v=1, it becomes a capacitor of 1/A(v) Farad. In between, A is a fitting parameter whose unit is dependent on v.

4.4.2.3. *Dipolar relaxation*

To represent the behaviour of dipoles relaxation in the resin, both induced dipoles and permanent dipoles have to be taken into account in the equivalent electrical model. As discussed in 4.3.3, induced dipoles react instantaneously and only the electron cloud is affected by the field, which does not dissipate energy. For that reason, they can be approximated by a simple capacitor C_{ind}. Permanent dipoles both store and dissipate energy through their orientation in the electric field. Therefore, a capacitor C_{perm} and a resistance R_{perm} in series are necessary to account for their behaviour.

The overall circuit for a single relaxation time dipolar relaxation is shown in Figure 4.3.

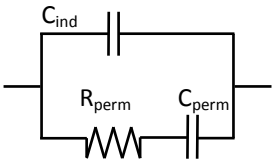


Figure 4.3 *Equivalent circuit for permanent and induced dipoles*

If permanent dipoles with different relaxation times are present, for each relaxation times, another set of resistance and capacitance in series needs to be added in parallel to the previous circuit (Mijovic and Fitz 1998). However, as discussed in 4.3.3, a single mean relaxation time will be assumed for all present dipoles. This relaxation time corresponds to $\tau_{dip}=R_{perm}C_{perm}$.

The admittance of the dipole orientation circuit shown in Figure 4.3 is thus given by:

$$Y_{dip}^{*} = \frac{R_{perm}C_{perm}^{2}\omega^{2} + j(C_{ind}\omega + R_{perm}^{2}C_{perm}^{2}C_{ind}\omega^{3} + C_{perm}\omega)}{1 + R_{perm}^{2}C_{perm}^{2}\omega^{2}} \quad (4.24)$$

$$Y_{dip}^{*} = \frac{C_{perm}\tau_{dip}\omega^{2} + j\omega(C_{ind} + C_{perm} + C_{ind}\tau_{dip}^{2}\omega^{2})}{1 + \tau_{dip}^{2}\omega^{2}} \quad (4.25)$$

4.4.2.4. *Overall circuit model of a thermoset resin*

The overall circuit of the thermoset resin comprises a representation for ion migration, electrode polarisation (E.P) and dipole orientation. The ion migration resistance (R_{ion}) is added in parallel to the circuit corresponding to the dipole orientation. The electrode polarisation is symbolized by two impedances (one for each electrode) in series with the contribution of dipoles and ions. The overall circuit is presented in Figure 4.4.

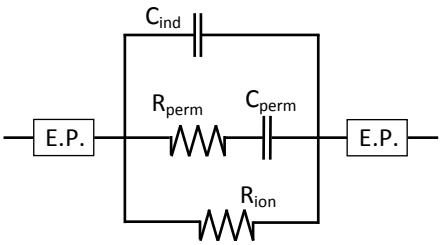


Figure 4.4 *Equivalent circuit of a thermoset resin*

The model parameters are determined by using the spectra of the uncured resin acquired with the final sensor between 1Hz and 10 kHz (see section 6.5.1). Those parameters are given in Table 4.2 and the corresponding modelled spectra are shown in Figure 4.5. The blue zone corresponds to the frequency range studied in the present work.

Table 4.2 *Parameters used in the theoretical electrical circuit model of the RS-M135 epoxy resin system*

N	A ($\Omega.s^{-0.5}$)	C_{ind} (F)	C_{perm} (F)	R_{perm} (Ω)	R_{ion} (Ω)
0.5	10^4	$6.00x10^{-12}$	$1.50x10^{-11}$	$2.55x10^5$	$1.37x10^7$

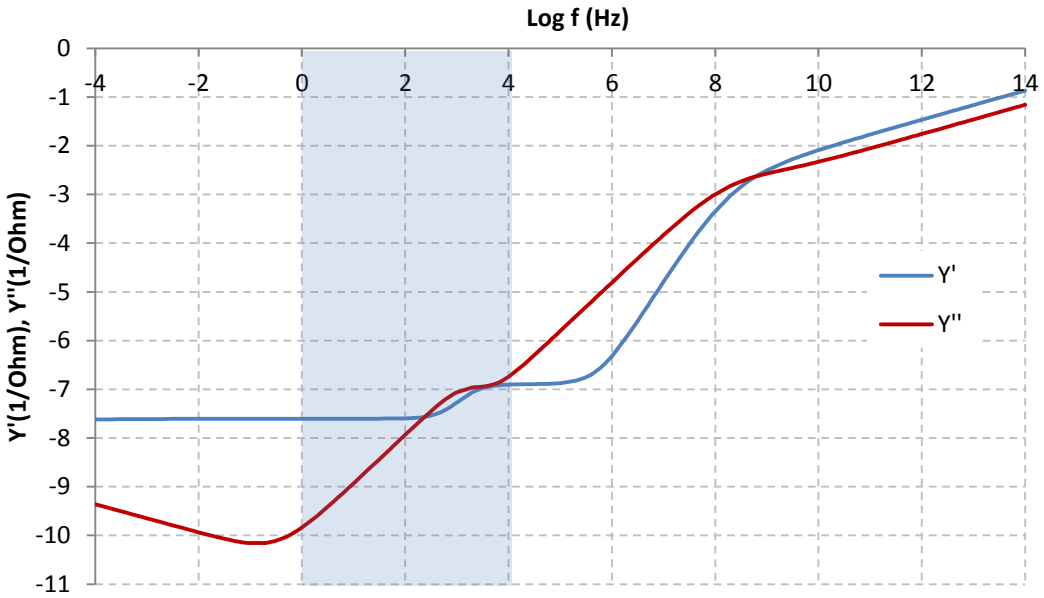
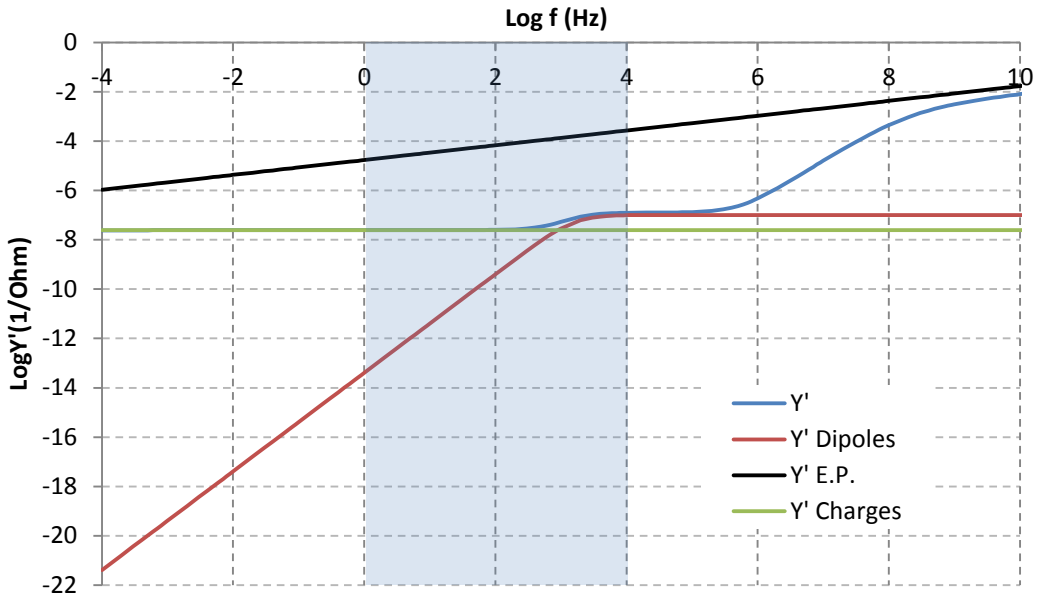
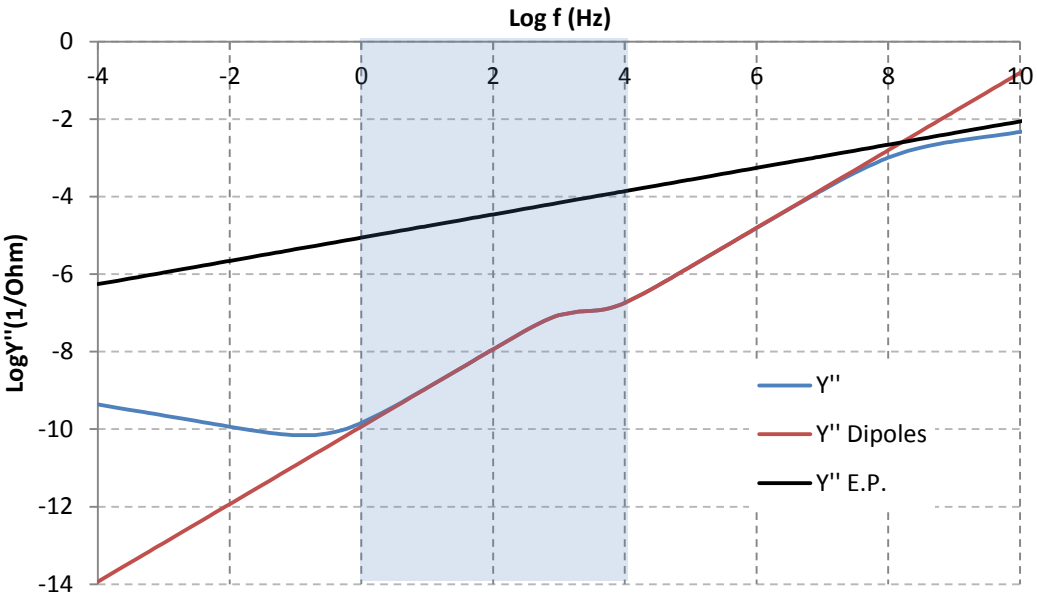


Figure 4.5 *Real and imaginary admittance of the uncured RS-M135 epoxy resin electrical equivalent circuit. In blue, the frequency range investigated in the present study*

By plotting the spectra of the different contributions with the admittance spectra in Figure 4.6 a and b, it is notable that the electrode polarisation is only prevalent at low and high frequencies. In the frequency range studied (1 Hz - 10 kHz), charge migration is the main contribution to the real part of the admittance, while the imaginary part is mostly impacted by dipole orientation.



(a)



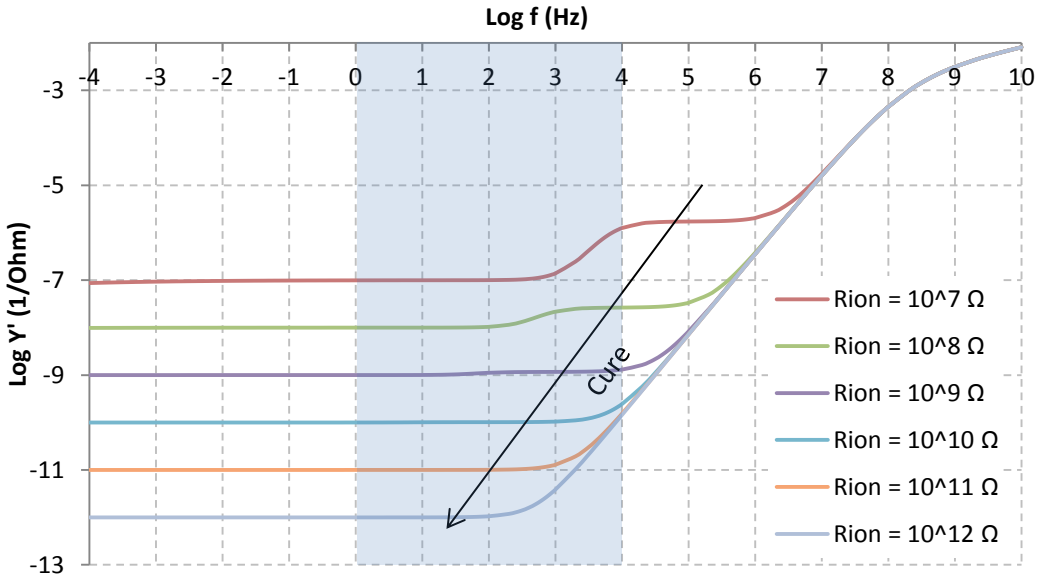
(b)

Figure 4.6 *Real (a) and Imaginary (b) admittance of the uncured RS-M135 epoxy resin electrical equivalent circuit and the contributions of electrode polarisation, dipolar orientation and charge migration*

As highlighted in section 4.3, ionic conductivity is the main contribution to the dielectric properties of the epoxy resin in the frequency range studied. During the

cure reaction, the mobility of the ions is hindered by the increased viscosity and formation of the 3D network. As a result, R_{ion} increases with time. To imitate that effect on the admittance obtained with the theoretical model, the value of R_{ion} is varied while keeping all the other parameters identical. The resulting curves are shown in Figure 4.7.

The spectra presented here shall be compared to the one obtained by the sensor prototypes during the resin cure in chapters 5 and 6 in order to validate ion migration as the main contribution to the epoxy resin permittivity.



(a)

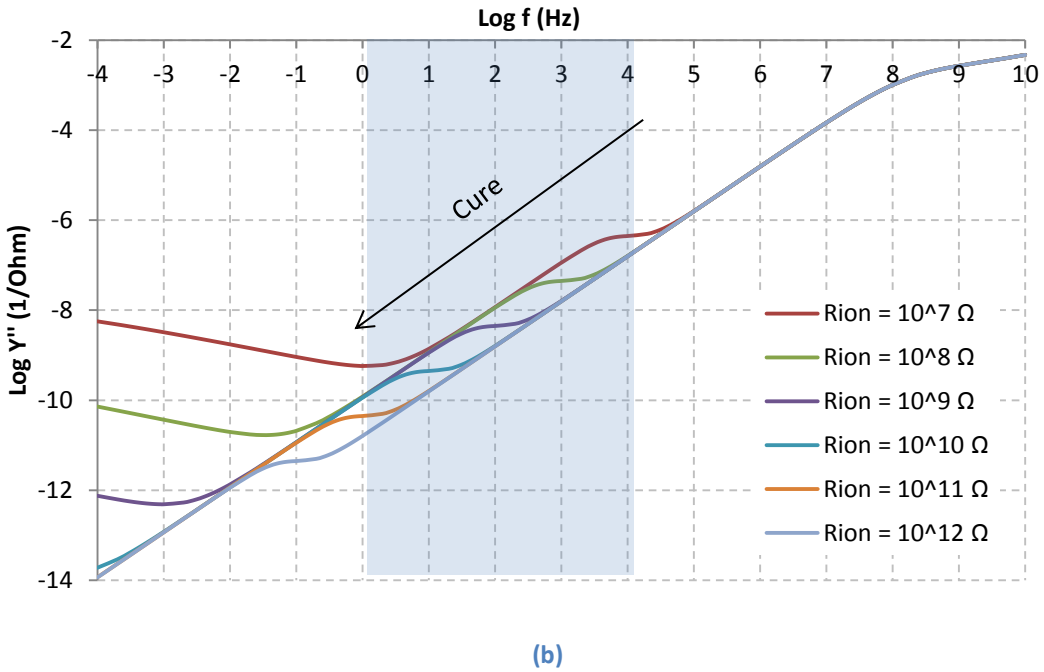


Figure 4.7 *Effect on an increase of R_{ion} on the real (a) and imaginary (b) admittance of the RS-M135 epoxy resin electrical equivalent circuit*

Despite the complexity of the cure mechanisms of a thermoset resin at a molecular level, the equivalent circuit for the dielectric sensor prototype and the curing resin can be further simplified. Assuming that ions migration is the main contribution to the dielectric properties of the studied material, and that all the microscopic losses can be grouped into a single capacitor, the resin system becomes a simple circuit formed of a capacitance and a resistance in parallel (Mijovic and Fitz 1998).

4.4.3. Equivalent circuit of the overall sensor + resin system

If the microscopic phenomena taking place during the cure of an epoxy resin can be modelled by using an electrical circuit equivalent, it is likewise possible to describe macroscopic variations, such as the filling of the infusion mould, as discrete electrical component equivalents.

4.4.3.1. *Dry sensor*

The dielectric sensor in air can be represented by an RC parallel circuit. The resistance and capacitance take into account the characteristics of the dry sensor environment before infusion. Because the sensor itself is made of different material, such as Kapton® adhesive film and PEEK (see sections 5.2.2 and 5.2.3), the contribution of the different materials surrounding the wires is to be taken into account in the characteristics of the RC model. The vacuum bag, breathing fabric and potential reinforcement layer placed on top of the sensor before the infusion process (described in chapter 2.2.3.2) also add their contributions to the electrical properties of the dry sensor. An equivalent circuit of the whole system is given in Figure 4.8.

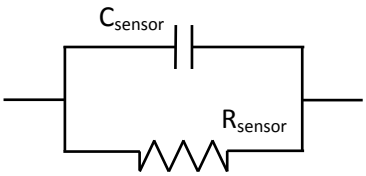


Figure 4.8 *Equivalent circuit of the sensor in air*

4.4.3.2. *Resin infusion*

When the resin starts to flow on top of the dielectric sensor, the electrical circuit can be divided into two sections: the part of the sensor wetted and the part that is still dry. They can be represented by two parallel circuits, shown in Figure 4.9.

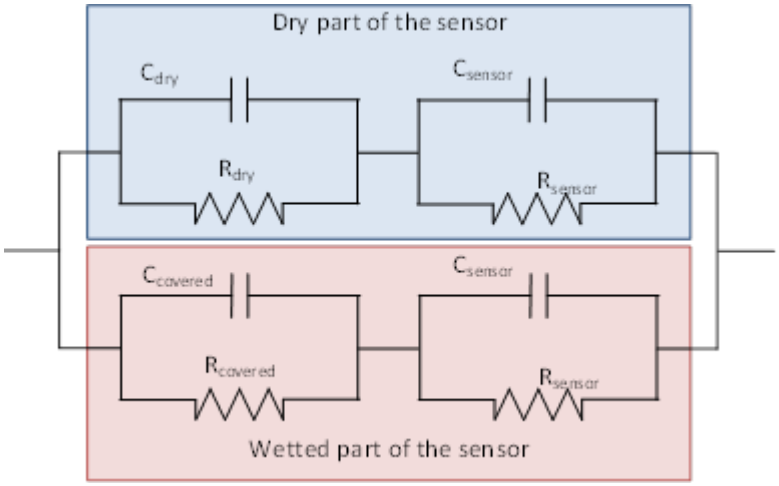


Figure 4.9 *Equivalent circuit of the partially covered sensor*

Assuming that the resin infusion is much quicker than the resin cure, the variations in the admittance measured are primarily due to the difference of permittivity between air and the resin being drawn on top of the sensor. The sensor detects a variation at the macroscopic level rather than a change at the molecular level in the resin itself. By following the variation of the admittance, it is thus possible to follow the filling of the mould (Skordos *et al.* 2000).

4.4.3.3. *Resin cure*

Once the filling of the mould is complete, the equivalent electrical circuit of the sensor fully covered with resin is once again a simple RC circuit, given in Figure 4.10. However, its characteristics are modified by the resin now covering the electrodes.

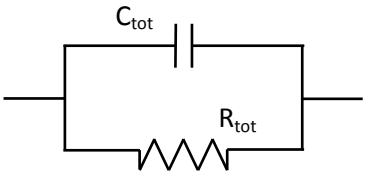


Figure 4.10 *Equivalent circuit of the sensor fully covered by epoxy resin*

The dry part of the circuit presented in Figure 4.9 has disappeared and only remains the wetted part. At that point, it is assumed that the observed variations of

the admittance are only linked to the curing process of the resin, as the system on top of the sensor no longer varies on a macroscopic level.

At the end of the cure, when the resin permittivity no longer varies, the system composed of the sensor and the cured resin (with potential reinforcement) can likewise be assimilated to another RC circuit. The values of the resistance and capacitance for this new circuit depend on the final composite plate. Thus, it would be theoretically possible to detect defects such as porosity in the final composite plate by comparing the values recorded for the corresponding RC circuit to those obtained for a perfectly manufactured composite.

4.5. Chapter Summary

Epoxy resin is a dielectric material characterised by its permittivity. Two main phenomena contribute to the said permittivity: migration of the ions present in the material and polarisation, which can be sub-divided into electrode polarisation and orientation of the dipolar species existing in the resin. Because the formation of the three dimensional network of the polymer affects all of these mechanisms, the permittivity of the resin varies as the cure reaction progresses. Thus, it is possible to follow the curing reaction by investigating the changes in permittivity with time.

Permittivity is an intrinsic value of the resin, which can be linked to its admittance. Working with the admittance allows the development of an electrical circuit analogy for each phenomenon present in the resin and thus an overall representation of the resin system is developed using electrical equivalences. By choosing the frequency range of the excitation signal so that electrode polarisation is negligible and ion migration prevails, the curing resin can be assimilated to a resistance and capacitor in parallel. The microscopic phenomena taking place in the resin as it cures can thus be followed by following the variations of the said capacitance and resistance with time.

On a macroscopic level, the whole sensor prototype can also be represented by RC parallel circuits while in air or covered by resin. In that case, the variations of the resistance and capacitance depend on a change in the environment of the sensor rather than chemical phenomena. Thus, the infusion of epoxy resin on top of the sensor can be monitored by following the admittance as a function of time.

In practice, following Y' and Y'' as a function of time and frequency shall allow the new dielectric sensor developed in the present work to be operational along the whole process of infusion, from the mixing of the resin to the final composite plate. This shall be discussed in chapter 5 and chapter 6.

5. Preliminary Dielectric Sensor Prototypes: Development and Characterisation

5.1. Scope and objectives

As seen in section 4.3, dielectric monitoring techniques are theoretically suitable to follow the entire infusion process of an epoxy resin. However, the sensing devices used for data recording are yet to be adapted to an industrial scale and tested for reinforced composites. To that end, the present research develops an entirely new dielectric sensor. This device has to be designed before being manufactured and tested. In order to validate the viability and geometry of the final prototype, several devices are developed and tested prior to building the final sensor. They are discussed in this chapter, after a brief presentation of the material and methods used for the infusion process of composite plates.

5.2. Sensor prototypes manufacture

The work of A.Skordos, (Skordos *et al.* 2000) proved that two flat electrodes placed at the bottom of an infusion mould were able to follow the filling of the said mould and the cure of an RTM resin. Because of the advantages of a co-planar sensor described in section 2.3.2.2, it has been decided that the sensor prototype developed in the present work would consist on an array of evenly spaced flat electrodes, destined to be placed at the bottom of an infusion mould. The length of the electrodes corresponds to the direction of the resin flow, and the design formed

of multiple electrodes allows for the potential investigation of the effect of electrode spacing on the dielectric response, as described in section 2.3.2.2. Those electrodes are kept in place by mean of a matrix that shall be discussed later in this chapter.

The choice of the material constituting the electrodes predictably turns to copper, due to its good electrical conductivity (59.6×10^6 $S \cdot m^{-1}$) and wide availability. However, the material composing the sensor substrate needs to be defined. This material must meet several industrial requirements, such as being flexible, in order to place the sensor in an existing infusion mould, resistant to high temperatures, and able to withstand numerous cycles of infusion process and de-moulding. In the interest of an industrial application in the wind turbine industry, it should also be possible to manufacture it in relatively large quantities.

In order to design and test the applicability of the proposed geometry, several sensor prototypes were considered and investigated.

5.2.1. PCB sensor

A first suggestion was to use flexible printed circuit boards (PCBs). Consisting of a thin layer of conductive material, usually copper, printed on flexible plastic substrates, PCBs allow precise control over the geometry of the printed conductor. However, many flexible circuits do not perform well above 150 ˚C, limiting their application in the case of infusion processes. Some manufacturers propose flexible circuit material that can perform for temperatures up to 225 ˚C, but these options are limited. Further concerns can be raised about the durability of the sensor: the thickness of the conductive layer deposited on top of the flexible substrate ranges from 10 to 100 µm and without any additional protection, the conductive layer is directly in contact with the resin, therefore likely to be damaged by successive infusions.

A preliminary test of small PCB sensors, shown in Figure 5.1, was nonetheless carried out but the inconclusive results lead to shifting the focus to another design.

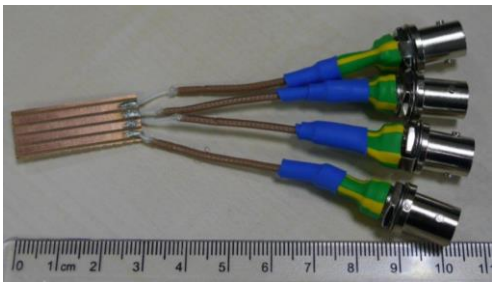


Figure 5.1 *Prototype of a small PCB based sensor*

5.2.2. Kapton® film prototype

In order to test the suitability of the dimensions proposed for the sensor, a very simple prototype was made by laying two couples of parallel flat copper wires 0.05 mm thick and 1.5 mm wide on top of a 400 x 450 mm aluminium plate, effectively creating two independent sensors. The distance between the electrodes of each sensor was 2 mm and 5 mm respectively. Those two sensors will be referred to as SK_1 for the 2 mm spaced electrodes and SK_2 for the 5 mm spaced electrodes. Those electrodes were insulated from the aluminium plate, held in place and protected by Kapton® tape, as shown in Figure 5.2.

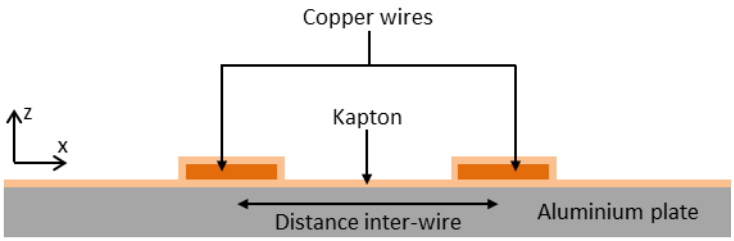


Figure 5.2 *Schematic of the Kapton® sensor layout*

Kapton® is a polyimide film developed by DuPont™ presenting a good resistance to heat and mechanical stress. In the present study, it is also used as a release film during the infusion and cure of the epoxy resin. The Kapton® tape is a 25.4 µm thick film made adhesive by the addition of a silicon adhesive to one of its side.

The aluminium plate on which the copper wires were attached was placed on an aluminium bench, electrically grounding the system and ensuring the electric field was created only in the material placed on top of the wires, effectively creating a half-cylinder shape. One end of each copper electrode was soldered to a female BNC cable connector (https://uk.rs-online.com/web/p/bnc-connectors/5121174/) in order to be connected to the dielectric measurement device (see section 5.3.3). The other end was left free.

This sensor was tested to follow an infusion of glycerol, before monitoring the infusion and cure of epoxy resin and glass fibre reinforced composite plates. The results obtained with this sensor will be presented further in this chapter in section 5.4.1.

5.2.3. First PEEK-based prototypes

After validating the overall geometry of the sensor prototype using the aforementioned Kapton® sensor, the development of a flexible sensor was carried out and two new sensor prototypes were manufactured. The aim of these prototypes was to validate the sensor fabrication protocol, as well as to choose between two possible device configurations, discussed later in this section.

The matrix chosen to encase the copper electrodes was polyetheretherketone (PEEK). PEEK is a semi-crystalline thermoplastic extremely resistant to mechanical stress and stable at high temperature, thus making it a suitable material for the sensor fabrication and industrial use. It presents a glass transition point around 143˚C, but does not melt under 343˚C. The present study uses the APTIV® 1000

Series Films from Victrex® (www.aptivfilms.com) in two thicknesses: 12 µm and 125 µm.

The overall concept of the sensor prototypes is to include the copped electrodes into a PEEK matrix providing a flexible and protective support. In order to embed the electrodes into the PEEK matrix, the wires were placed in contact with solid PEEK sheets in a precise layout described further in this section. The PEEK and wire system was then put under pressure in a heating press and heated until the melting point of the PEEK. At that stage, the PEEK flowed and enclosed the wires. After cooling down, the PEEK matrix solidified around the copper wire electrodes and a flexible sensor prototype was obtained.

In order to maintain the copper wires parallel during the whole process, a guiding tool was designed and built. It consisted of a 400 x 300 mm, 20 mm thick aluminium plate, cut on two opposite sides with sixty 2 mm wide gouges placed 5 mm apart, as shown in Figure 5.3.

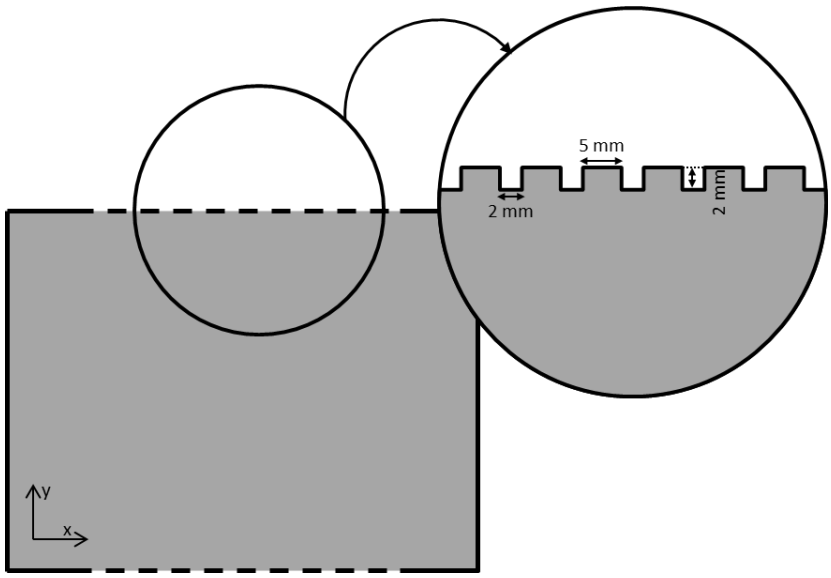


Figure 5.3 *Illustration of the copper wire guiding tool*

The purpose of these gouges was to keep the copper wires evenly spaced and parallel to each other during the melting of the PEEK in the heated press.

Two distinct layouts were tested for the prototype manufacture, as shown in Figure 5.4 and Figure 5.5. For both prototypes created, the same protocol was followed: the guiding tool was first covered by a Kapton® release film before PEEK sheets were added. Eight parallel flat copper wires were cut from the same 0.05 mm thick and 1.5 mm wide flat copper wire used in section 5.2.2 for the Kapton® sensor. They were cleaned with acetone, dried and placed on top of the PEEK in adjacent slots of the guiding tool. The wires were put under tension and taped at the bottom of the guiding tool. Depending on the prototype layout, a second set of PEEK films might be added. The whole system was covered with another Kapton® release film and an aluminium plate. The stack was placed at ambient temperature in a heating press, put under a pressure of 10 bars and heated at 370 ˚C for 20 minutes before cooling down. The pressure was maintained during the cooling down until the temperature reached ambient. The temperature ramp during the cooling down was not controlled.

One sensor prototype was formed by layering two 150 x 250 mm sheets of 12 µm thick PEEK film on top of the sensor, adding the copper wires, and covering them with another two sheets of 12.5 µm PEEK film (Figure 5.4). As the PEEK melted, it encased the wires before solidifying around them during the cooling down. This sensor will be referred to as SP_1.

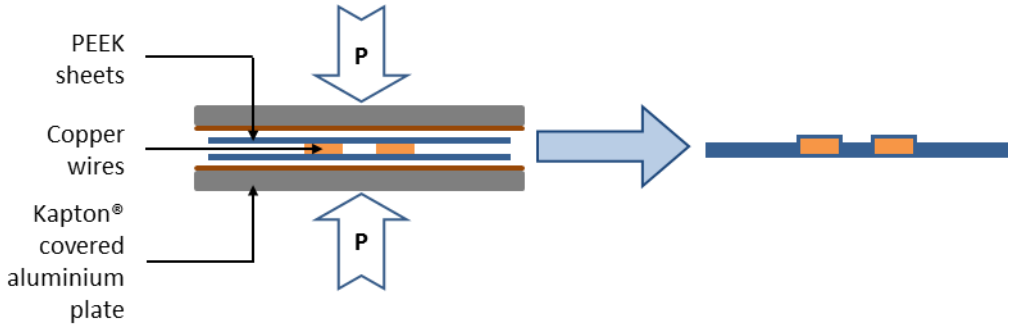


Figure 5.4 *Schematic fabrication of the "sandwich" PEEK sensor (SP_1)*

The second prototype sensor consisted of a 150 x 250 mm, 125 µm thick PEEK film on top of which the copper wires were placed, before being covered directly by the Kapton® release film and aluminium plate (Figure 5.5). In order to ensure a good repartition of the melted PEEK, 100 µm thick shims were placed at all four corners of the PEEK rectangle. As the PEEK melted, the wires were pressed down under the 10 bars load. The final product was a sensor in which the copper wires were level with the surface of the PEEK, rather than inside it. This sensor will be referred to as SP_2.

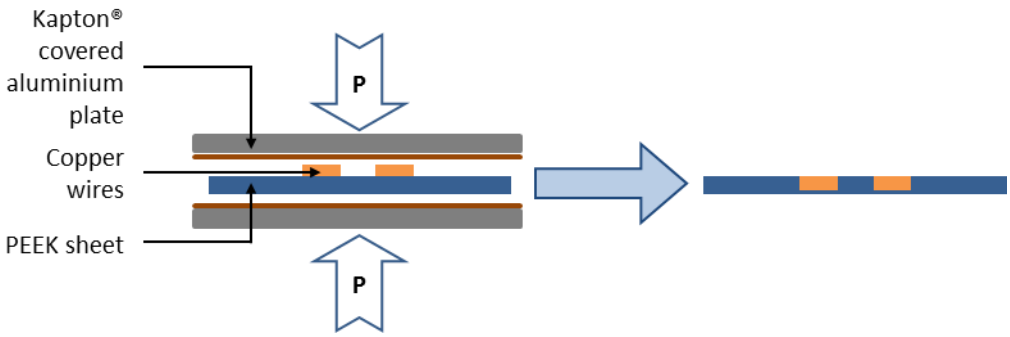


Figure 5.5 *Schematic fabrication of the one-sided PEEK sensor (SP_2)*

For both sensors, the surface in contact with the infused medium was covered with Kapton® tape. This step added an additional protection layer for the electrodes and facilitated the removal of the material investigated after each experiment. In

the case of the SP_2 sensor, the infusion took place on the PEEK rich side (bottom side on Figure 5.5).

Similarly to the Kapton® sensor, females 50 Ohm BNC cables connectors were soldered onto one extremity of each copper electrode while the other one was left free. The copper electrode extremities, having been oxidised by the heating in the press, were etched with a 10% HCl solution before being soldered.

The two sensors obtained were flexible, did not present air bubbles or visible defects in the PEEK matrix. They were sturdy enough to undergo infusion experiments. The sensor SP_2, formed of a thicker sheet of PEEK, was less flexible but easier to manipulate and overall more robust.

The two prototypes were tested by following the infusion of glycerol. The results are given in section 5.4.2, further in this chapter.

5.3. Composite plates manufacture and monitoring

In order to test the response of the dielectric sensor in industrial conditions, several infusions needed to be performed, with and without glass fibre reinforcement. They followed a similar procedure than the one described in 2.2.3.2.

5.3.1. Composite material components

The composite materials used for the present research project have been generously provided by PRF Composite Materials (http://www.prfcomposites.com/)

The epoxy resin used in this study is the RS-M135 (PRF Composite Materials, 2015b). It is a bisphenol A based resin, formulated for the fabrication of glass, carbon and aramid fibre reinforced composites. This resin is more specifically designed for applications in shipbuilding, wind turbines and sports equipment. Its ultra-low viscosity of 200 mPa at 25˚C makes it ideal for injection moulding or

vacuum infusion. The processing of the resin can be made between 10 ˚C and 50 ˚C and its operating temperature ranges from -60 ˚C to 60 ˚C without postcure, and up to 80 ˚C with postcure. The postcure process is briefly explained later in this section.

Some relevant resin properties are presented in Table 5.1.

Table 5.1 *RS-M135 resin properties*

Density at 25˚C ($g.cm^{-3}$)	**Viscosity at 25˚C (mPa.s)**	**Epoxide equivalent**	**Epoxide value**
1.13-1.17	700-1100	166-185	0.54-0.60

The epoxide value given in Table 5.1 represents the number of epoxide groups per gram of resin. It is given by:

$$epoxide\ equivalent = \frac{1}{epoxide\ value} * 1000 \quad (5.1)$$

The RS-M135 resin cure reaction starts when the resin is mixed with a hardener. Two types of the said hardener are proposed by the manufacturer, a slow one and a fast one. The hardener system chosen in the present study is the fast hardener RS-MH134 (PRF Composite Materials, 2015b). This amine based hardener allows a 20 - 30 minutes pot life for the mixed resin. Some of its properties are given in Table 5.2.

Table 5.2 *RS-MH134 hardener properties*

Density at 25˚C ($g.cm^{-3}$)	**Viscosity at 25˚C (mPa.s)**	**Amine value** (mgKOH.g^{-1})
0.94-1.00	10-50	166-185

The amine value corresponds to the weight of potassium hydroxide (KOH) needed to neutralise 1 g of hardener, representing the active hydrogen (NH) content of the hardener.

The ratio of resin to hardener is given by the manufacturer as 10:3 in weight. After the hardener and the resin are mixed, the mixture cures at room temperature

(20 - 25˚C), changing from a clear viscous liquid to a translucent rigid material. It can then undergo a heat treatment at 40 - 150 ˚C to improve the overall mechanical properties of the composite. This heat treatment is called postcure. The main focus of the present study is on the curing process itself, and not on the final composite plate. The mechanical properties of the manufactured composite are thus irrelevant for the present work and the postcure heat treatment was purposefully omitted while manufacturing the composite plates.

The reinforcement material used in all the composite plates fabrication is a plain woven roving glass fabric ER006 at 800g.m^{-2} (PRF Composite Materials, 2015a), with a warp count of 1.8 th.cm^{-1} and a weft count of 1.5 th.cm^{-1}.

5.3.2. Infusion and cure methodology

The sensor prototypes presented in this chapter were used to follow the infusion of glycerol as well as the infusion and cure of the plain RS-M135 epoxy resin. The infusion of glass fibre reinforced epoxy composite plates is studied in chapter 6, but the methodology for the composite infusion being very close to the one used for epoxy or glycerol infusion, it will be described below.

In the case of a composite plate infusion, 3 or 6 layers of glass fibres reinforcement measuring 200 x 200 mm were layered on top of the sensor, as shown in Figure 5.6. These layers were covered with a breathing fabric layer before being vacuum bagged. This porous breathing fabric ensured an even flow of the resin through the vacuum bag and thus a better impregnation of the reinforcement fibres. Depending on the number of layers, the final plate thickness varied from 2 mm to 5 mm.

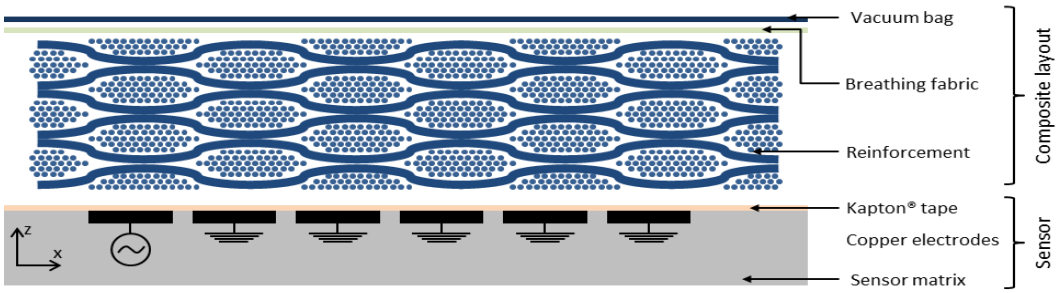


Figure 5.6 *Cut plane of the setting of a composite plate infusion showing the sensor prototype (at the bottom) and the stacking of the glass fibre woven fabric*

To ensure vacuum, tacky tape was applied on the outside of the sensor, two inlets were placed in two opposite corners of the formed square and a vacuum bag was positioned on top of the whole system, as shown in Figure 5.7. Tacky tape was likewise wrapped around the inlet and outlet tubes at their junction with the vacuum bag to ensure the airtightness of the bag.

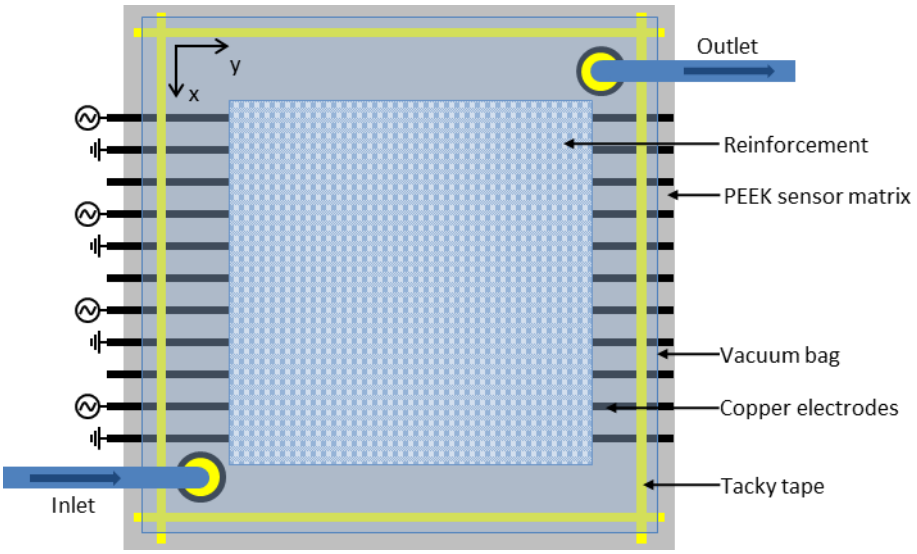


Figure 5.7 *Top view of a composite plate infusion setting*

After drawing the vacuum in the bag and verifying the absence of air leaks, the epoxy resin was mixed with the hardener and immediately infused through the layers of reinforcement. When the fabric was homogeneously wetted by the resin,

the inlet and outlet tubes were clamped before the system was left to cure at room temperature for 24 hours.

In the case of an epoxy-only or glycerol infusion, the layers of reinforcement were replaced by a meshed resin distribution medium to prevent the vacuum bag from sticking to the sensor surface, as well as to ensure the resin progressed homogeneously along the wires.

The dielectric measurements, recorded with the device presented in section 5.3.3, were started with the vacuum being drawn in the bag, just before mixing the resin and hardener. They were stopped after complete cure, 24h after the end of the infusion process. The vacuum bag and breathing fabric were discarded and the cured composite plate was removed from the surface of the sensor.

5.3.3. Dielectric measurement device

The dielectric measurements were performed with a customized Dielectric Monitoring system (c-DieMos) developed by Engineering Technology Solutions E.E. (ETS E.E.). Four dielectric sensors entries were plugged in simultaneously using 50 cm long BNC cables of resistance 50 Ohms (https://uk.rs-online.com/web/p/coaxial-cable/4262038/). The resistance and capacitance measured by the dielectric sensors were logged and processed by the software provided with the monitoring device.

In parallel, the ambient temperature was recorded using a thermocouple. The first cure experiments were monitored with a FLIR T200 infrared camera to assess the variations of temperature in the composite plate during cure. The curing reaction is exothermic, but it was conjectured that the large surface ratio of the composite plate and the contact with large metallic surfaces would allow a quick dissipation of the heat produced. No temperature variations in the plate were visible for three different cure experiments, therefore it was assumed that the

temperature of the experiment was the ambient temperature recorded by the aforementioned thermocouple.

Before an experiment was run, an automatic calibration of each four couples of BNC cables was performed using a known RC circuit box comprising a 50 Ohms resistance and 12 pF capacitance in parallel. This step ensured the contribution of the cables was removed from the dielectric measurements. One couple of cables was plugged into the calibration box and an automatic calibration protocol was started. The protocol run three multifrequency analyses and matched the resistance and capacitance recorded during these analyses to the theoretical values of the calibration resistance and capacitance. This protocol was followed for each couple of BNC cables before each infusion trial.

Two to four independent recordings of the same cure were made for every infusion experiment. Each of the four channels of the c-Diemos can be dedicated to a couple of electrodes from the sensor prototype. In this chapter, only two couples of electrodes were recording for each experiment, but the four channels were used for the testing of the final sensor prototype discussed in chapter 6.

A multifrequency analysis was performed to follow the composite cure: sixteen sinusoidal signals of frequencies between 1 Hz and 10 kHz with four frequencies per decades (1 Hz, 2 Hz, 3 Hz, 6 Hz, 12 Hz, 22 Hz, 40 Hz, 74 Hz, 136 Hz, 251 Hz, 464 Hz, 858 Hz, 1585 Hz, 2929 Hz, 5412 Hz and 10 kHz) and amplitude 10 V were simultaneously sent with a sample rate of 3.5 µs. The resistance and capacitance measured by the dielectric sensors in response to the excitation signal were recorded as a function of time for a period of 24 hours. Following the experimental protocol described in section 5.3.2, the recording was started before the resin was mixed to obtain a baseline for the sensor in air. The monitoring continued until the end of the 24 hours cure.

5.4. Prototypes tests

All the sensors prototypes presented in section 5.2 were submitted to different tests in order to determine their suitability to the monitoring of epoxy infusion and cure. The results obtained for the Kapton® and PEEK based prototypes are given in the following sections.

5.4.1. Kapton® prototype

The Kapton® film sensors were used to validate the suitability of the parallel electrode geometry for the monitoring of an infusion and cure process. The response of the Kapton® sensor was tested in different configurations: infusion of glycerol, infusion and cure of RS-M135 epoxy resin. The influence of inter-wire distance on the signal obtained was briefly studied.

5.4.1.1. *Infusion of glycerol*

Glycerol is innocuous and relatively inexpensive. It presents the advantage of being a viscous fluid of which dielectric properties are known (Segur 1953), thus making it appropriate to test the suitability of the geometry chosen for the dielectric sensor. Some relevant properties of glycerol are given in Table 5.3.

Table 5.3 *Properties of glycerol*

Viscosity (Pa.s)	Dielectric constant	Conductivity (S)
1.41	41.14	10^{-8}

The complex permittivity of glycerol is given by:

$$\varepsilon^* = \varepsilon' - j\varepsilon'' = \varepsilon_r - j\frac{\sigma}{\varepsilon_0 \omega} \quad (5.2)$$

where ε_r is the dielectric constant and σ the conductivity given in Table 5.3, ε_0 is the permittivity of free space and ω is the angular frequency.

Prior to the experiments, the Kapton® sensor surface was cleaned with acetone and left to dry. An additional layer of infusion mesh was added on top the sensor in order to prevent the vacuum back from sticking to the sensor surface and facilitate the glycerol flow. The glycerol was then drawn in the vacuum bag, along the length of the electrodes, as shown in Figure 5.8.

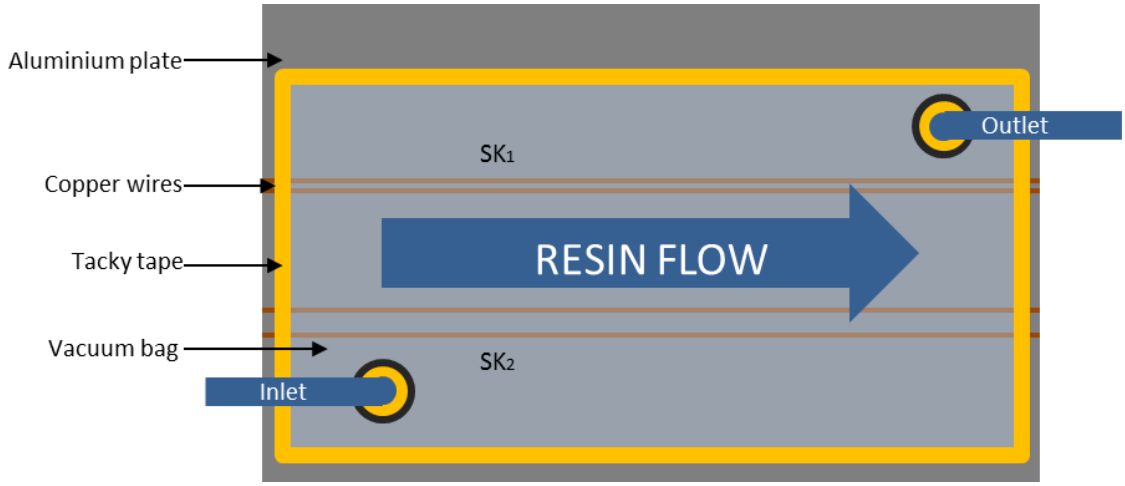


Figure 5.8 *Infusion setup for the Kapton® based sensor*

The spectra obtained for the two sensors in air, prior to any infusion, are presented in Figure 5.9.

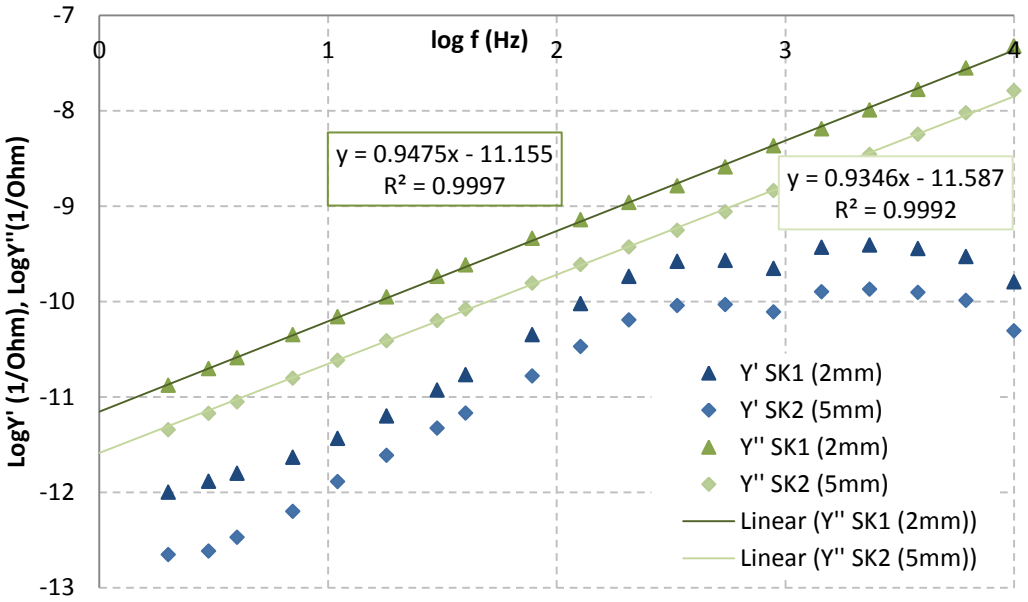


Figure 5.9 *Spectra of the admittance of the Kapton® sensors in air*

The measurements confirm a sensor with closer electrodes provides a stronger signal. The imaginary part of both sensors presents a linear dependence with the frequency. Assuming that the sensor in air can be represented by an RC circuit, as discussed in section 4.4.3, the imaginary part is given by:

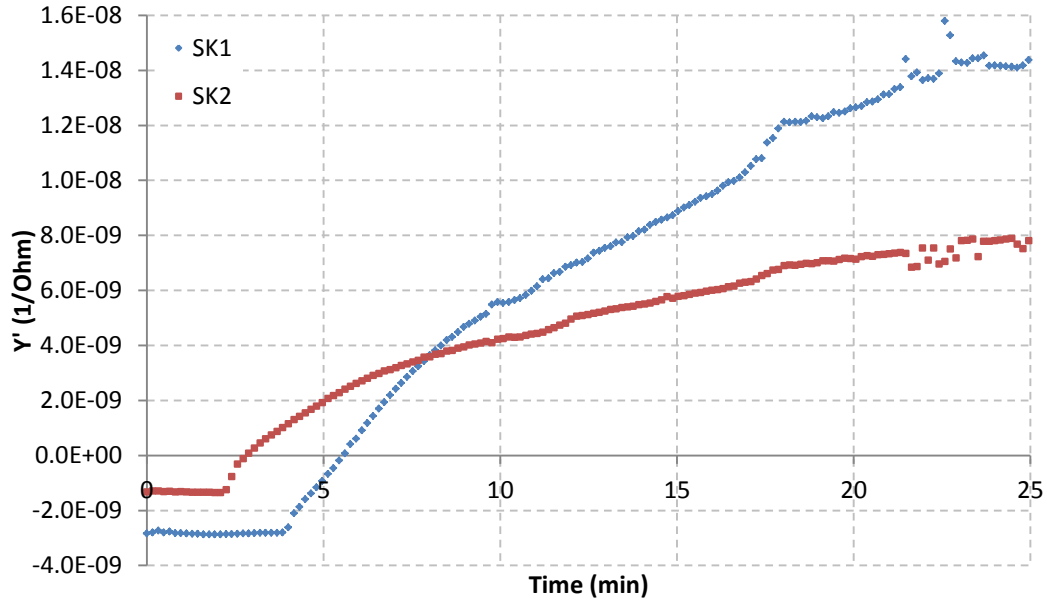
$$Y'' = C_{sensor}\omega \tag{5.3}$$

$$Log(Y'') = Log(C_{sensor}) + Log(\omega) \tag{5.4}$$

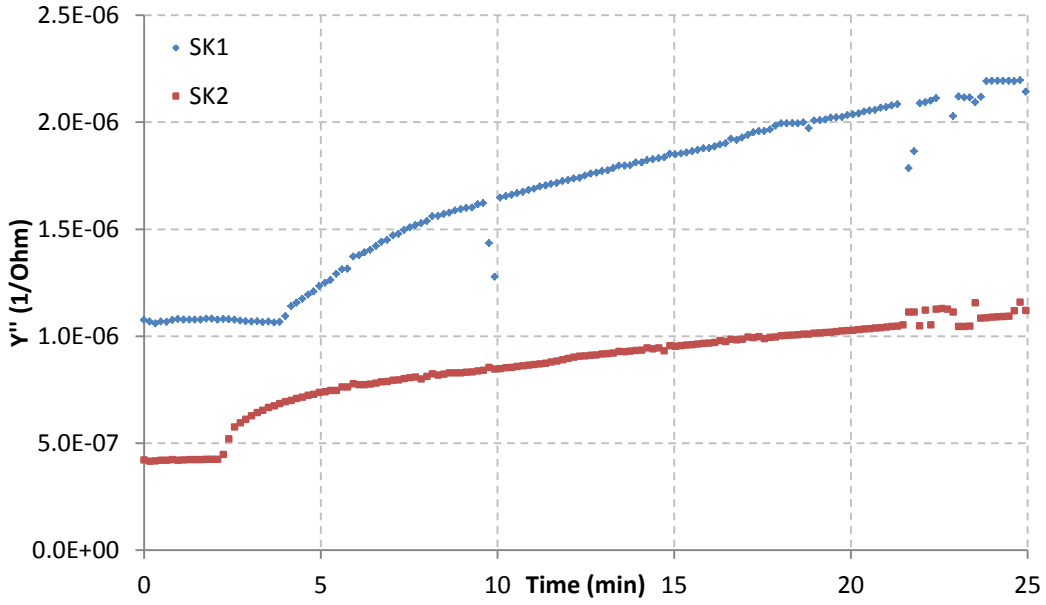
where Y'' is the imaginary part of the admittance, C_{sensor} the capacitance of the sensor in air and ω the angular frequency.

In the case of a perfect RC circuit, the slope of the curves for Y'' in Figure 5.9 is equal to 1. The experimental values obtained are very close to 1, thus confirming the capacitive nature of Y''.

The admittance measured while drawing glycerol on top of the sensors is given in Figure 5.10.



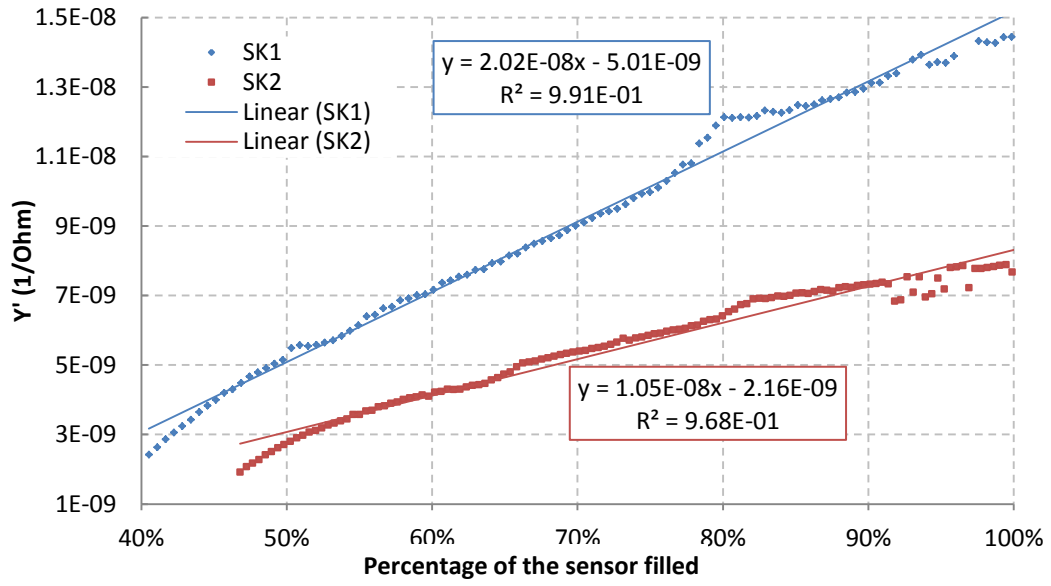
(a)



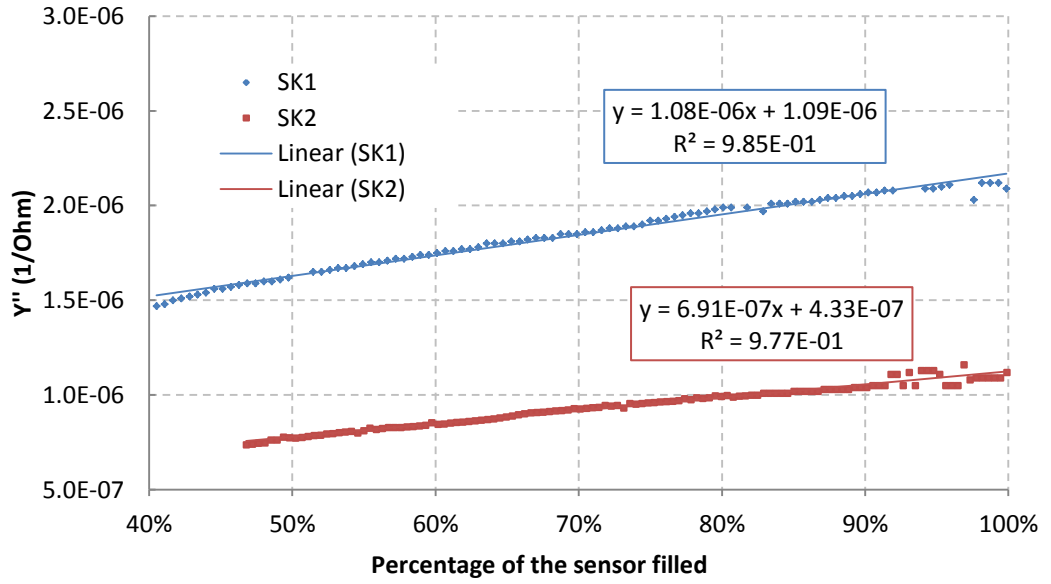
(b)

Figure 5.10 : *Real (a) and imaginary (b) part of the admittance during the drawing of glycerol on top of the Kapton® sensor at respectively 136 Hz and 10 kHz*

For a better understanding of the relationship between the length of the sensor wetted and the admittance measured, Figure 5.11 shows the complex admittance plotted versus the percentage of the sensor covered by glycerol.



(a)



(b)

Figure 5.11 *Real (a) and imaginary (b) admittance versus length of the Kapton® sensor wetted by glycerol at respectively 136 Hz and 10 kHz*

The work of A. Skordos (Skordos *et al.* 2000) has shown that the admittance measured during infusion presents a linear dependence with the length of the sensor covered by the resin:

$$Y_{meas} = \left(Y_{tot} - Y_{dry} \right) l_{\%} + Y_{dry} \quad (5.5)$$

with

$$l_{\%} = \frac{length\ of\ the\ sensor\ covered\ by\ resin}{total\ length\ of\ the\ sensor} \quad (5.6)$$

Y_{meas} is the admittance measured experimentally at $l_{\%}$ filling, Y_{tot} is the admittance of the fully covered sensor and Y_{dry} is the admittance of the dry sensor before infusion.

Matching the previous equation with the linearization factors of the curves shown in Figure 5.11, the equation becomes:

$$Y_{meas} = A_l l_{\%} + B_l \quad (5.7)$$

$$\begin{cases} Y_{dry} = B_l \\ Y_{tot} = A_l + B_l \end{cases} \quad (5.8)$$

Y'_{dry}, Y''_{dry} Y'_{tot} and Y''_{tot} can be calculated using the coefficients obtained by linearizing the experimental results. The values found for Y_{dry} and Y_{tot} are compared to the experimental values measured by the prototype at the beginning and end of the infusion experiment. The results are presented in Table 5.4 with the corresponding relative error:

$$\delta\alpha_r = \frac{|\ Ylinear - Yexperimental\ |}{Yexperimental} \quad (5.9)$$

Table 5.4 *Experimental and calculated values of admittance for the Kapton® sensors (in air and covered by glycerol) at 136 Hz and 10 kHz for respectively the real and imaginary part of the admittance*

	$Y'_{dry\ calculated}$ (1/Ω)	$Y'_{dry\ experimental}$ (1/Ω)	Relative error	$Y''_{dry\ calculated}$ (1/Ω)	$Y''_{dry\ experimental}$ (1/Ω)	Relative error
SK_1	-5.01×10^{-9}	-2.8×10^{-9}	78.93%	1.09×10^{-6}	1.07×10^{-6}	1.87%
SK_2	-2.22×10^{-9}	-1.3×10^{-9}	70.77%	4.33×10^{-7}	4.22×10^{-7}	2.60%
	$Y'_{tot\ calculated}$ (1/Ω)	$Y'_{tot\ experimental}$ (1/Ω)	Relative error	$Y''_{tot\ calculated}$ (1/Ω)	$Y''_{tot\ experimental}$ (1/Ω)	Relative error
SK_1	1.52×10^{-8}	1.42×10^{-8}	6.74%	2.17×10^{-6}	2.23×10^{-7}	2.69%
SK_2	8.28×10^{-9}	8.11×10^{-9}	2.05%	1.12×10^{-6}	1.15×10^{-6}	2.26%

A large relative error is observed for the real part of the dry sensor admittance. This error is in all probability due to the order of magnitude of the measurements: the values are at the limit of the apparatus detection range, leading to consequent uncertainties.

The other calculated values show a good agreement with the measured ones, therefore validating the geometry of the prototype. Despite higher values of the overall admittance recorded, the relative error calculated for the measures obtained with the sensor SK_1 is not significantly better than the one calculated for the sensor SK_2.

The influence of a smaller distance between electrodes on the measurement accuracy is not significant enough to justify an electrode spacing of 2 mm. A distance of 5 mm between electrodes is technically easier to manufacture and sensitive enough for the present study, thus it will be favoured for the building of the subsequent prototypes.

5.4.1.2. *Numerical modelling of the infusion of glycerol*

In parallel of the new dielectric sensor prototype development presented in the previous section, a 3D numerical model of the device was built and studied. The aim of such a model is to obtain a better understanding of the electric field repartition around the sensor, confirm the experimental results and ultimately, be used as a predictive tool to study the infusion and cure process.

The entire modelling work of the present project was developed using the software Comsol Multiphysics™ 5.2. with the addition of its AC/DC module. This module, based on Maxwell's equations, is used to build and solve electromagnetic models at low frequencies. The constitutive equations solved by the software in the present study are:

$$\nabla . J = Q_{j,v} \quad (5.10)$$

$$J = \sigma E + j\omega D + J_e \quad (5.11)$$

$$E = -\nabla V \quad (5.12)$$

where J is the current density, Qj,v the volumetric source of current inside the selected modelled layers, σ the conductivity, E the electric field, j^2=-1, ω the frequency, D the displacement field, J_e the external current density and V the voltage.

In order to correctly model the real lossy materials used in the present study, it is necessary to use a constitutive relation. In the case of the dielectric material studied in the present work, the displacement field D is used. The current conservation condition is thus given by:

$$\sigma = 0 \quad (5.13)$$

$$D = \varepsilon_0(\varepsilon' - j\varepsilon'')E \quad (5.14)$$

where E is the electric field, ε_0 is the permittivity of free space and ε' and ε'' are the real and imaginary permittivity of the material studied respectively. This condition is applied to all domains modelled.

A first simple model of two parallel flat wires in air was run and compared to an analytical solution (Orphanidis, 1999) to validate the model building technique before further complexification. The model was afterwards iterated, first by flattening the wires, then by adding the Kapton® matrix around them and finally by adding the dielectric material on top of the sensor to create a three dimensional model of the Kapton® sensor. The geometry of the model was designed as close to the real sensor as possible, but for the number of wires. Only one couple of wires was investigated in order to minimise the solving time and memory used during the runs of the model.

The dimension and properties of the different components used in the simulation are given in Table 5.5 and Table 5.6 respectively.

Table 5.5 *Dimensions of the Kapton® sensor numerical model components*

	Background	Kapton®	Wires	Glycerol
Width (mm)	100	80	1.5	80
Depth (mm)	30	0.108	0.05	5
Height (mm)	350	30	300	variable

Table 5.6 *Dielectric properties of the Kapton® sensor numerical model components* (Segur, 1953; Dupont, 2018)

Material	Conductivity σ (S.cm^{-1})	ε'	ε''
Air	-	1	0
Kapton®	-	3.4	0.01224
Glycerol	10^{-8}	41.14	$\frac{\sigma_{glycerol}}{\omega\varepsilon_0}$

In Table 5.6, $\sigma_{glycerol}$ corresponds to the conductivity of the glycerol, ω is the angular frequency of the excitation signal and ε_0 the permittivity of free space.

The electrodes were modelled by removing the volume corresponding to the wires from the middle of the Kapton® film volume. The voltage applied to the electrodes being localised at the surface of the conductor, no modelled solid was necessary to represent the electrodes. The faces of the holes created were assigned a voltage: 10 V for one electrode and a ground (0 V) for the other. The bottom of the Kapton® layer was likewise grounded to represent the contact of the bottom of the sensor with the aluminium bench.

The sensor model was surrounded by a rectangular background volume. A boundary condition of "electrical insulation" $\vec{n} \cdot \vec{J} = 0$ (with n normal vector to the surface and J electric current density) was applied on each six faces of the volume. This boundary condition meant that no current was flowing through the faces and that any potential was discontinued across them. The background volume was assigned the material properties of air.

The entire volume of the model was meshed with an automatic tetrahedral mesh of "finer" size. The mesh generated by the software is automatically refined where the geometry of the model requires it. The model was solved for the frequencies corresponding to the multifrequency analysis performed experimentally and described in section 5.3.3.

Figure 5.12 shows the admittance of the SK_1 sensor in air calculated with the model.

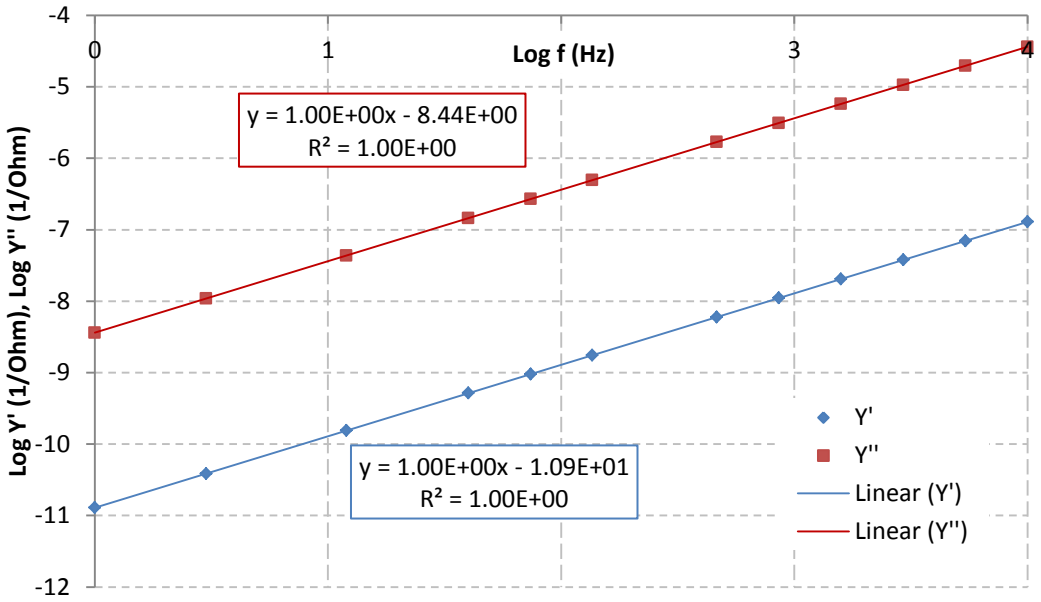


Figure 5.12 *Numerically modelled admittance of the Kapton® sensor in air. The inter-wire distance is set at 2mm*

The values obtained for Y' and Y'' are one to four orders of magnitude superior to the one measured experimentally and shown in Figure 5.9. This indicates the numerical model does not accurately predict the sensor response. However, the imaginary admittance still presents a linear dependence with the frequency, and the slope of the logarithmic curve is 1. This indicates Y'' is proportional to the frequency with a factor equal to the capacitance of the modelled RC circuit. Using the values given by the numerical model, this capacitance is determined to be 1.29×10^{-11} F. The capacitance value obtained experimentally for SK_1 is 4.67×10^{-12} F, thus giving a large relative error of 176%.

A numerical simulation of glycerol infusion is nonetheless carried out and the admittance obtained for a simulated filling of the sensor is given in Figure 5.13.

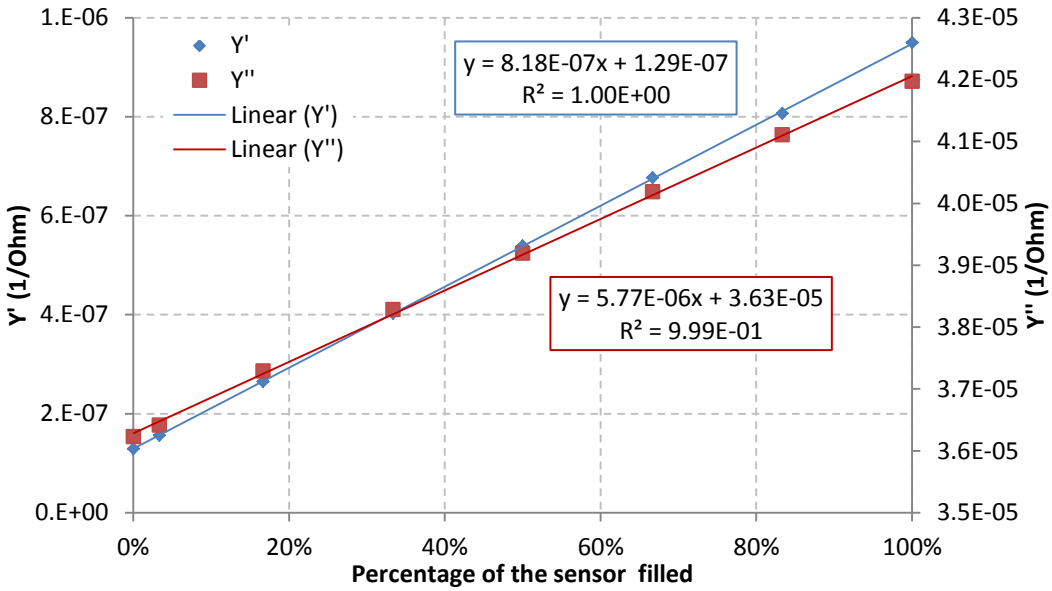


Figure 5.13 *Numerically modelled admittance of the Kapton® sensor during an infusion of glycerol. The inter-wire distance is set at 2mm*

The values of the admittance modelled are still several orders of magnitude above the one observed for SK_1 in section 5.4.1.1. However, the slopes of the curves are close to the one recorded experimentally, as shown in Table 5.7.

Table 5.7 *Comparison between the slope of the modelled and recorded admittance of SK_1 during the infusion of glycerol*

	Slope Y'	**Slope Y''**
Experimental	2.02×10^{-8}	1.08×10^{-6}
Model	8.18×10^{-7}	5.77×10^{-6}

The numerical model of the Kapton® sensor developed is capable of reproducing the trend observed during the experimental infusion of glycerol. However, the large discrepancy between the calculated admittance and the recorded one makes it impossible to use it as an accurate predictive tool as yet.

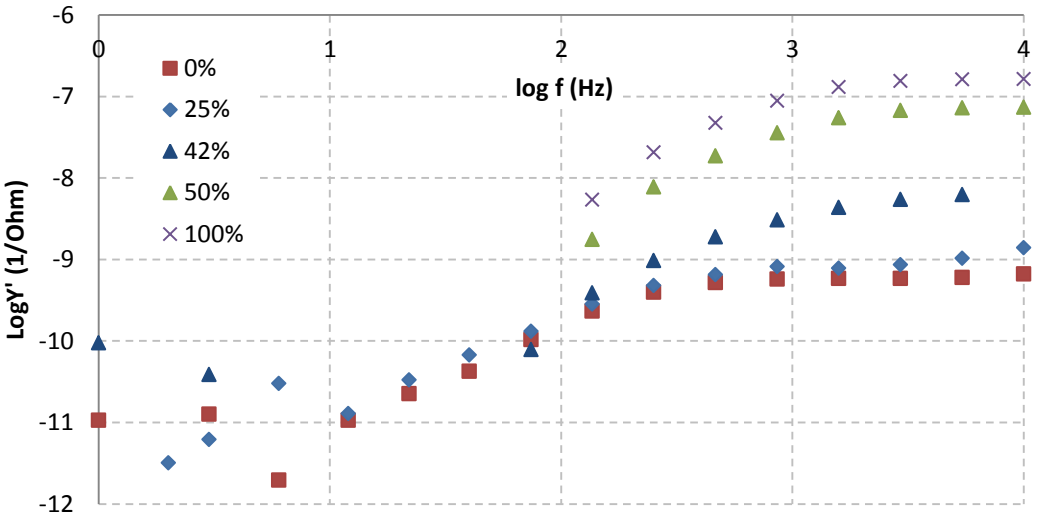
Several factors can explain the discrepancies between the experimental values and the modelled ones. Experimentally, the grounding of the sensor is realised by way of the aluminium bench and the electrode is grounded via the c-Diemos

recording device. In the model, the "ground" condition for the grounded electrode and the bottom of the aluminium plate are the same. This could be a reason for errors, as the software does not differentiate between the two grounds and the electric field modelled might be affected. Improperly designated boundary conditions may as well be causing the observed discrepancies.

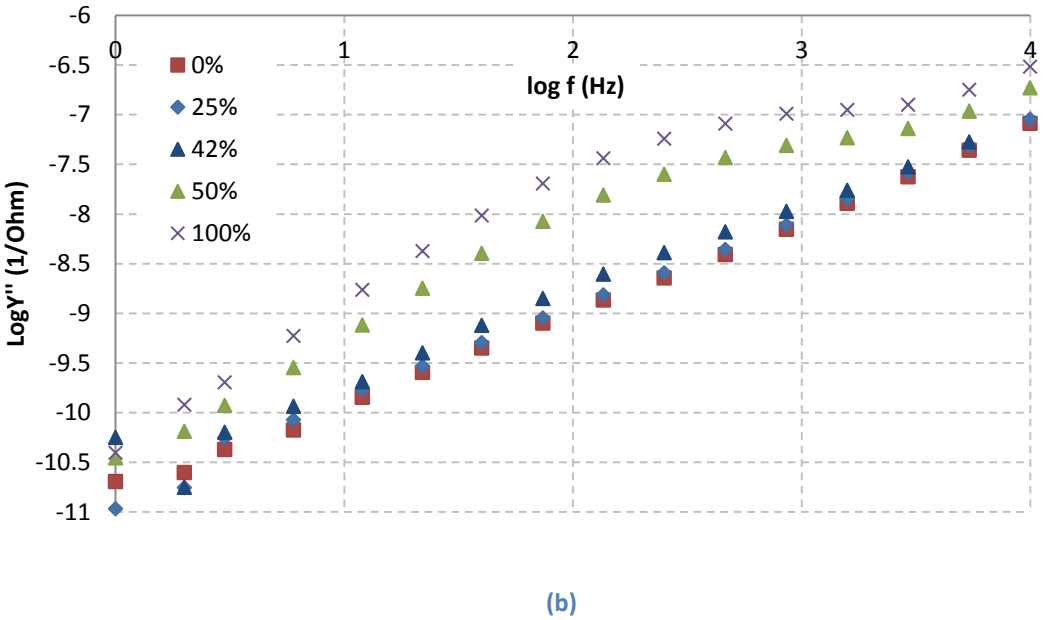
5.4.1.3. *Epoxy infusion and cure*

Experimentally, tests of epoxy infusion and cure were performed on the Kapton® sensor to confirm its suitability for the monitoring of the RM-S135 resin system. The resin was mixed with the hardener just before being drawn under vacuum on top of the sensor with the exact same methodology used for glycerol (see section 5.4.1.1).

The spectra obtained for different length of the sensor SK_1 wetted with epoxy are given in Figure 5.14.



(a)



(b)

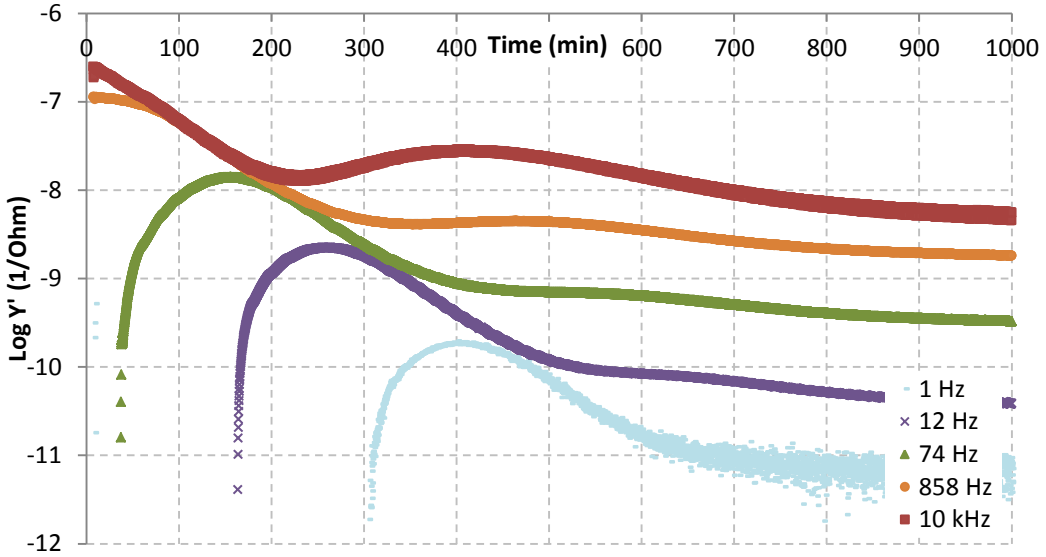
Figure 5.14: *Real (a) and imaginary (b) part of the admittance of the sensor SK_2 during infusion of epoxy resin (1 kHz). The percentage indicates the length of the sensor wetted*

The spectra obtained for the wetting of the sensor show that the resin does impact the sensor response.

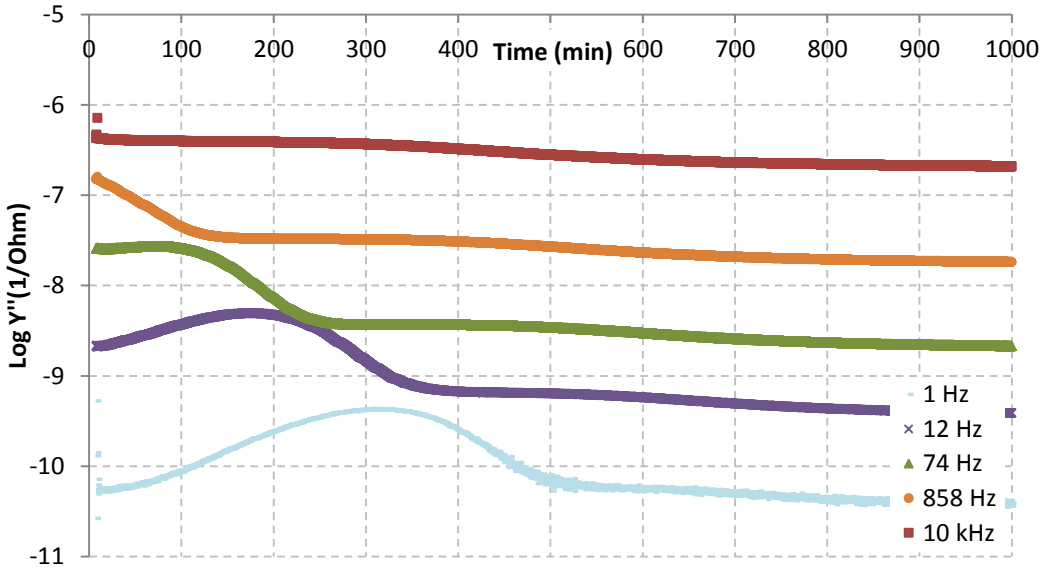
The real part of the admittance presents an increase at high frequencies as the sensor is being covered by the resin. No such trend is observed below 200 Hz, likely due to the apparatus detection range. From the imaginary part of the admittance, it is clear the addition of epoxy transform the circuit formed by the sensor and its surrounding from a capacitive system, translated by a linear relation between Y'' and the length covered, towards a more complex circuit that does not present a linearity .

The curves obtained at 50% and 100% of the sensor covered are similar to the one obtained with the resin electrical analogy presented in section 4.4.3.3 , thus suggesting the sensor is indeed interrogating the uncured epoxy resin.

The epoxy resin was afterward left to cure at room temperature, monitored, for 24 hours. The sensor prototype recorded the variations of the measured admittance along the cure of the resin, as shown in Figure 5.15.



(a)



(b)

Figure 5.15 *Variations of the real (a) and imaginary (b) admittance during the infusion and cure of RS-M135 epoxy resin on top of the Kapton® based sensor. Five frequencies of excitation are presented*

The real admittance at 858 Hz and 10 kHz decreases as the resin cure starts, before increasing again and reaching a local maximum later in the cure. This behaviour is not as clear for lower frequencies, mainly due to the fact the values of Y' at the beginning of the cure are below the c-Diemos detection range. The 1Hz curve is similarly noisy at the end of the cure when it becomes close to the apparatus detection lower limit. All the curves but the one at 1 Hz seem to show a local maximum that moves towards higher cure time as the frequency decreases.

That phenomenon is likewise observed in the curves of the imaginary admittance. The admittances obtained for 858 Hz and 10 kHz decrease from an initial maximum, while the admittances at lower frequencies present a local maximum before decreasing toward their end value.

For both the real an imaginary part of the admittance, higher frequencies give a stronger signal, minimising the experimental error. However, the curves for Y'' only display a local maximum for frequencies below 858 Hz. Thus, lower frequency values are providing important information about the curing reaction and shall be investigated as well.

The spectra obtained at different times during the cure are presented in Figure 5.16.

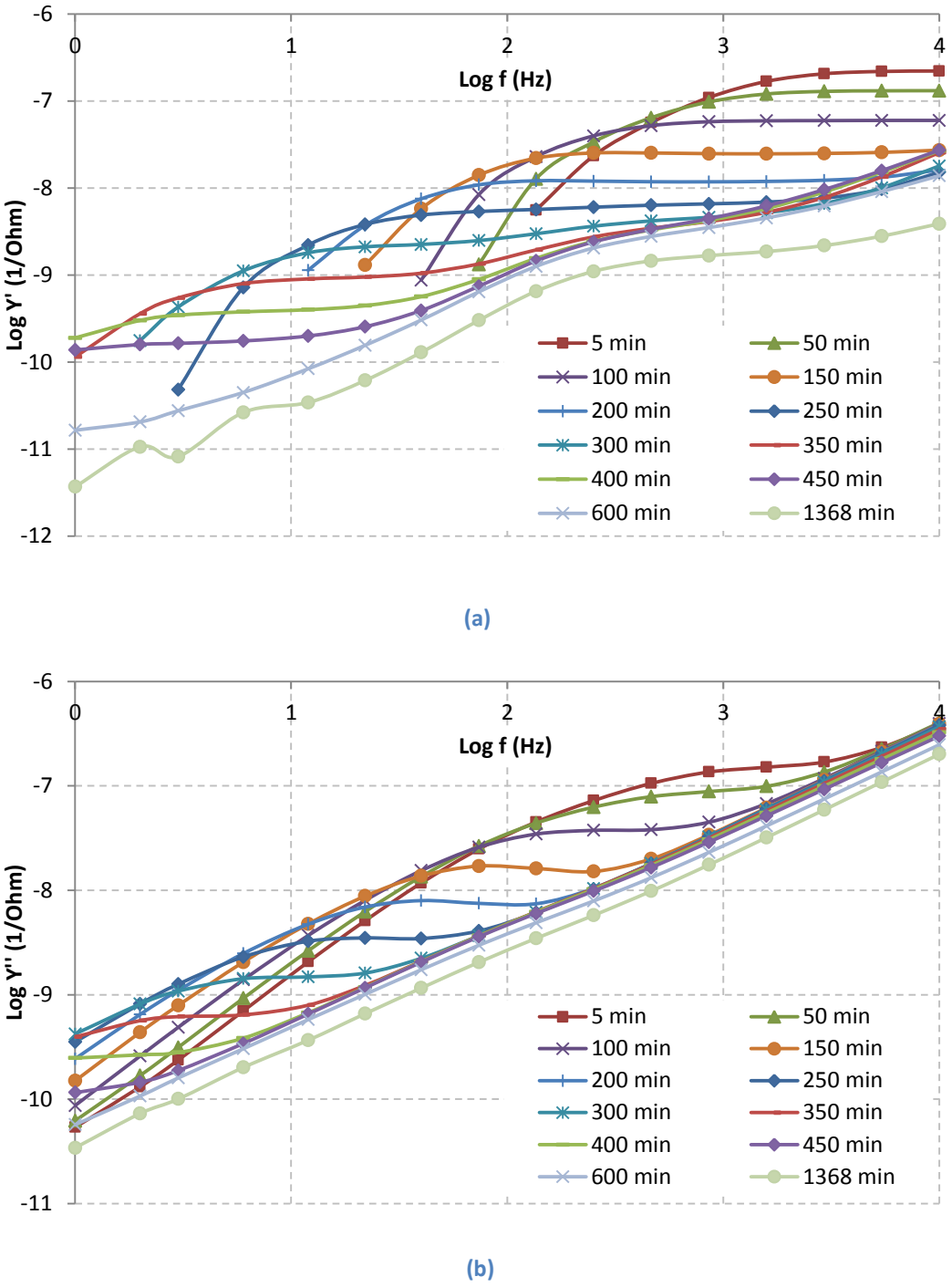


Figure 5.16 *Spectra of real (a) and imaginary (b) admittance during the cure of RS-M135 epoxy resin on the Kapton® sensor*

The spectra obtained are very similar to the ones presented in section 4.4.3.3, proving the ability of the Kapton® sensor to follow the cure of the epoxy resin

investigated. It also confirms the ions migration dominates the conductivity mechanisms between 1 Hz and 10 kHz. This will be further discussed in chapter 6.

The Kapton® sensor results validate the use of two parallel flat copper electrodes as a way to follow the filling of an infusion mould, as well as the cure of the RS-M135 epoxy resin, between 1Hz and 10 kHz. Despite closer wires providing a stronger signal, the difference in accuracy with electrode slightly further apart is not significant enough to justify the choice of a 2 mm wide sensor over a 5 mm wide one. Besides, electrodes further apart create a deeper electric field, penetrating the material investigated and providing information further from the electrode surface (see section 2.3.2.2). This feature is especially interesting in the case of composite manufacture, where the thickness of the final pieces can reach several centimetres. Therefore, the distance between the electrodes of the subsequent prototypes will be set at 5 mm.

5.4.2. PEEK prototypes

The two PEEK sensors presented in 5.2.3 were tested by an infusion of glycerol in order to decide of the settings for the final sensor fabrication.

The glycerol infusion was realised with the protocol described for the Kapton® sensor in section 5.4.1.1. Each PEEK sensor was cleaned with acetone, taped to the aluminium bench before being covered with an infusion mesh and vacuum bagged. The admittance variations with the length of the sensor wetted are given in Figure 5.17 and Figure 5.18.

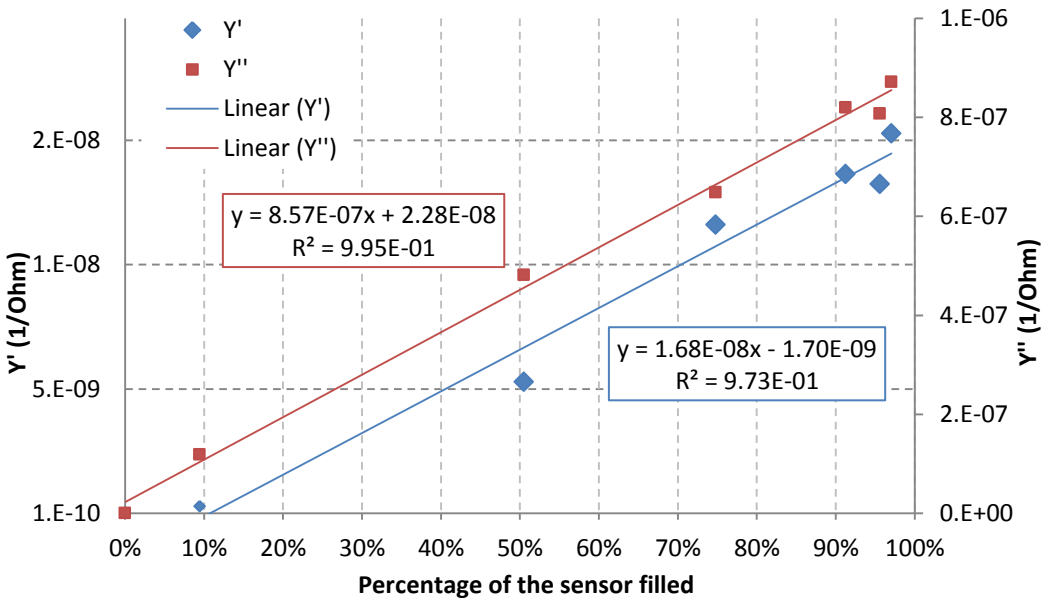


Figure 5.17 *Real and imaginary admittance versus length of SP_1 wetted by glycerol at respectively 136 Hz and 10 kHz*

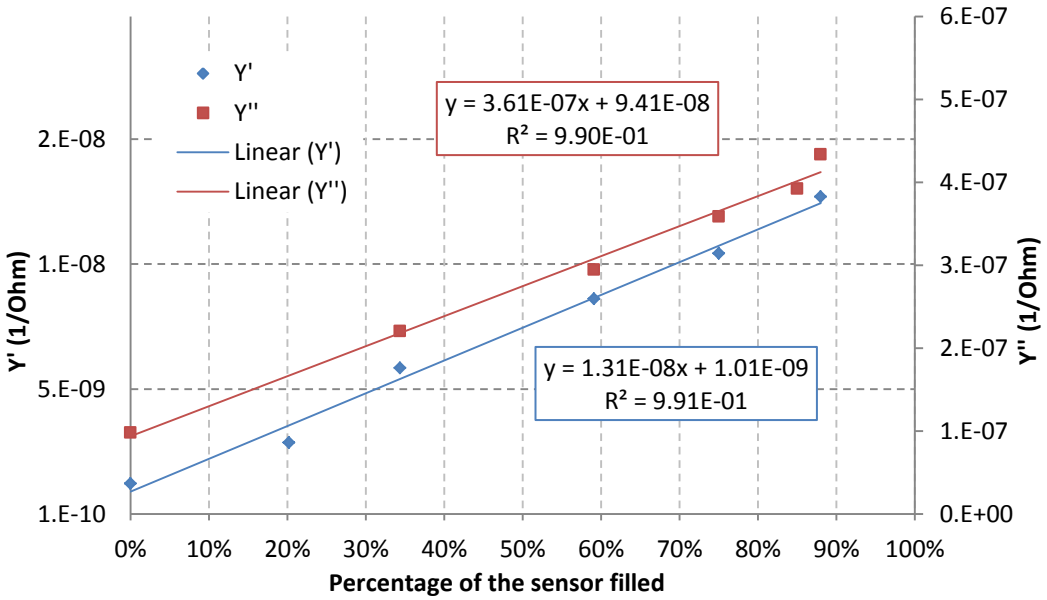


Figure 5.18 *Real and imaginary admittance versus length of SP_2 wetted by glycerol at respectively 136 Hz and 10 kHz*

Once again, the admittances of the dry and covered sensors can be calculated with the coefficients of the linearization curves and compared to the one recorded experimentally. The results are given in Table 5.8.

Table 5.8 *Experimental and calculated values of admittance for the PEEK sensors (in air and covered by glycerol)*

	$Y'_{dry\ calculated}$ (1/Ω)	$Y'_{dry\ experimental}$ (1/Ω)	Relative error	$Y''_{dry\ calculated}$ (1/Ω)	$Y''_{dry\ experimental}$ (1/Ω)	Relative error
SP_1	-1.70×10^{-9}	-1.20×10^{-8}	85.83%	2.28×10^{-8}	2.44×10^{-8}	6.56%
SP_2	1.01×10^{-9}	1.25×10^{-9}	19.20%	9.41×10^{-8}	9.50×10^{-8}	0.95%

	$Y'_{tot\ calculated}$ (1/Ω)	$Y'_{tot\ experimental}$ (1/Ω)	Relative error	$Y''_{tot\ calculated}$ (1/Ω)	$Y''_{tot\ experimental}$ (1/Ω)	Relative error
SP_1	1.51×10^{-8}	1.64×10^{-8}	7.93 %	8.50×10^{-7}	8.55×10^{-7}	2.69%
SP_2	1.41×10^{-8}	1.40×10^{-9}	0.79%	4.55×10^{-7}	4.58×10^{-7}	0.63%

For both sensors, the largest error is observed for the real admittance of the dry sensor because of the very small values measured. Sensor SP_2 provides the smallest relative errors on every measure, in addition to being easier to manipulate and more resistant. For these reasons, it is the setting favoured for the manufacture of the final sensor prototype.

5.5. Chapter Summary

The geometry of the new dielectric sensor to be built was investigated by manufacturing and testing several prototypes. After briefly examining the idea of a PCB sensor and finding it unsuitable, a sensor made of flat copper wires taped to an aluminium plate was built and tested by following an infusion of glycerol. The infusion and cure of epoxy resin were also monitored using this prototype. These sets of experiments confirm the suitability of two parallel flat electrodes to follow both the filling of an infusion mould as well as the cure of epoxy resin between 1 Hz and 10 kHz. It also serves to set the distance between electrodes to 5 mm for the final sensor prototype design.

In parallel, a numerical 3D model for the infusion of glycerol on top of the Kapton® sensor was developed. Its results are promising despite discrepancies being present.

Two prototypes of flexible dielectric sensors based on a PEEK matrix were built in order to validate the final sensor manufacture protocol, as well as determining the best layout for the final sensor prototype. After characterising these sensors using a glycerol infusion, it was established that the best design for the final sensor prototype is copper electrodes 5 mm apart pressed into a 125 µm thick layer of PEEK.

6. Final Prototype of the Flexible Dielectric Sensor

6.1. Scope and objectives

In this chapter, the fabrication of the final PEEK sensor prototype is described. The response of this device during the infusion and cure of the RS-M135 epoxy resin is studied, before the influence of the glass fibre reinforcement on the measurements obtained during both infusion and cure is examined. Finally, the results given by the dielectric sensor prototype for the cure of the epoxy resin are compared with the ones obtained during the epoxy cure characterisation discussed in chapter 3.

6.2. Sensor prototype fabrication

The final PEEK based sensor was built in a similar way than the SP_2 prototype studied in chapter 5. Flat copper wires were placed on top of a PEEK sheet before being treated in a heating thermal press. When heated above its melting temperature under pressure, the PEEK becomes malleable and thus, the wires can be incorporated into the sheet. During cooling down, the PEEK matrix solidifies again and the wires are trapped in place.

A similar protocol to the one described to build the SP_2 sensor in section 5.2.3 was followed, with the same materials. A Kapton® release film was laid on the guiding tool before being covered by a square of 200 x 200 mm, 125 µm thick PEEK.

60 flat copper wires 0.05 mm thick and 1.5 mm wide were cut to form the electrodes of the sensor. The copper electrodes were cleaned by immersing the wires into a 10% solution of HCl for 15 seconds before being rinsed, dried and placed on top of the PEEK sheet, using the gouges of the tool as guides to maintain the wires parallel to each other. The mechanical tension of the copper wires was ensured by taping them at the back of the tool with Kapton® heat-resistant tape. Shims 100 µm thick were placed at all four corners of the PEEK square to guaranty an even repartition of the thermoplastic when melting, as well as a good inclusion of the copper wires in the PEEK matrix. A second layer of Kapton® release film was placed on top before another flat aluminium plate.

The whole stack was placed in a Fontjine thermal press, model Labpro 600. A pressure of 20 kN is applied while the press is heated at 370 ˚C. This temperature was maintained for 15 minutes to ensure an even melting and flow of the PEEK, before the press was cooled down to room temperature. The pressure was released and the sensor prototype removed from the aluminium plates.

The release film was peeled; the oxidized copper electrodes were cleaned with a 10% HCl solution before being soldered to female 50 Ohm BNC cable connectors in order to be connected to the c-Diemos device.

Finally, Kapton® tape was applied to the PEEK-rich surface of the prototype in order to limit the adherence of the cured composite to the device and add an extra layer of protection. This step ensured the prototype could be reused for several experiments without being damaged. The sensor was taped on an aluminium bench, acting like an electrical ground. Consequently, when a voltage was applied to the different electrodes, the electric field created took the shape of a semi-cylinder on top of the sensor electrodes, where the material to investigate was placed.

A picture of the finished sensor is presented in Figure 6.1.

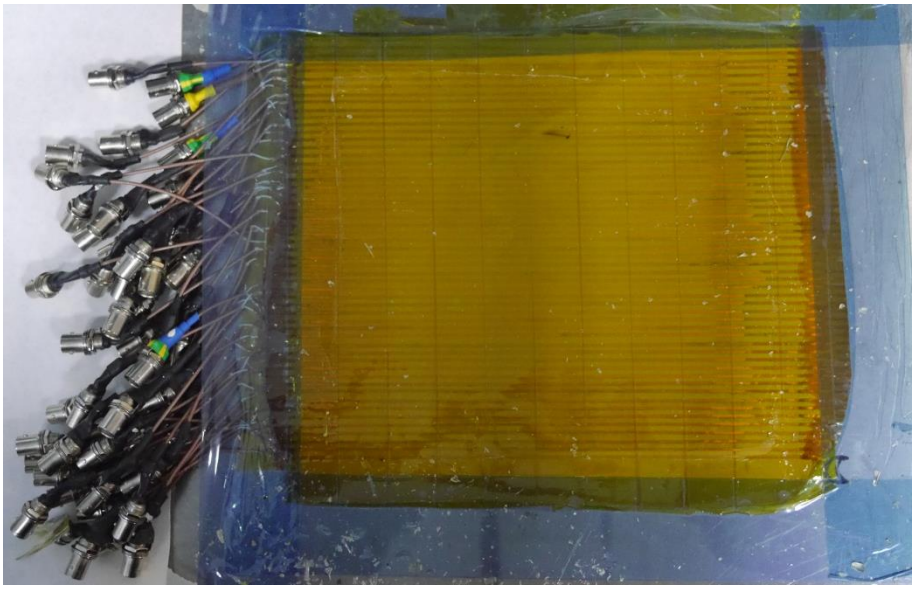
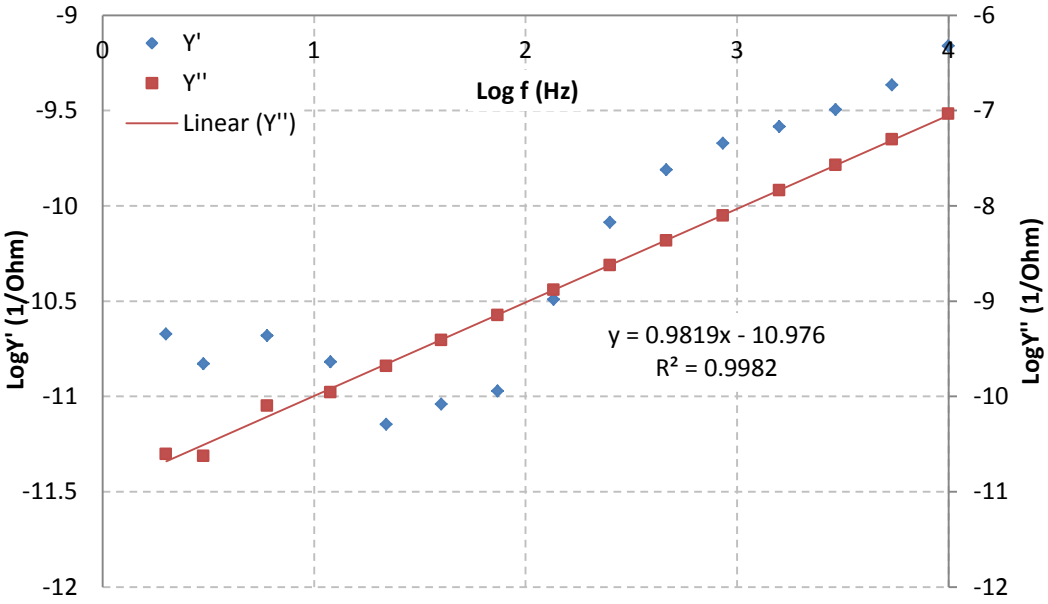


Figure 6.1 *Final sensor prototype*

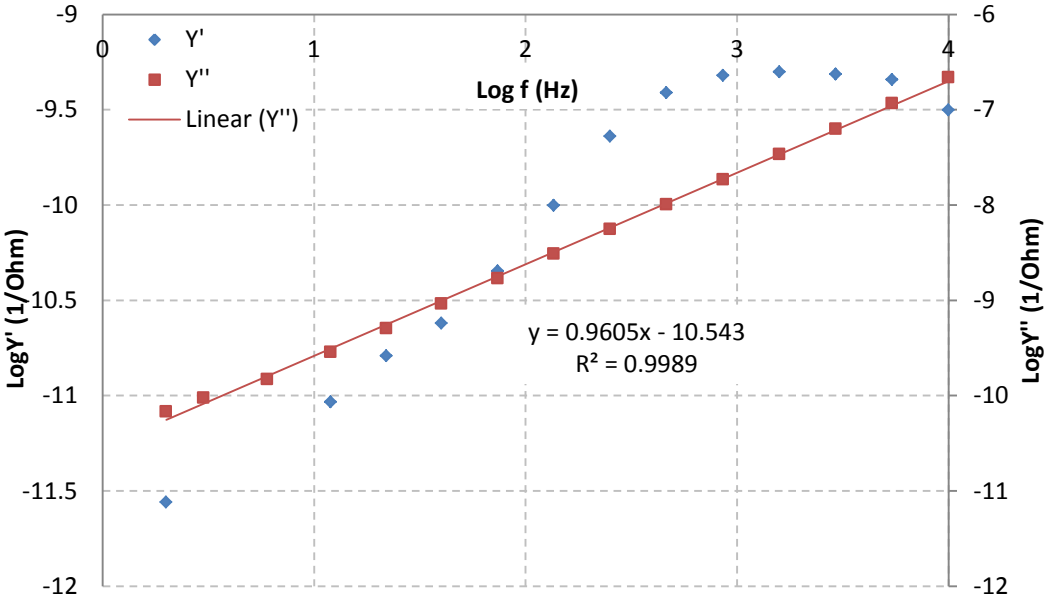
6.3. Prototype characterisation in air

The response of the sensors before infusion was studied in order to obtain the characteristics of the system without resin. In the following section, the spectra of three sensors in air are studied. They correspond to a sensor covered with only infusion mesh and a vacuum bag, a sensor covered with three layers of glass fibre reinforcement and a vacuum bag, and a sensor covered with six layers of glass fibres reinforcement and a vacuum bag.

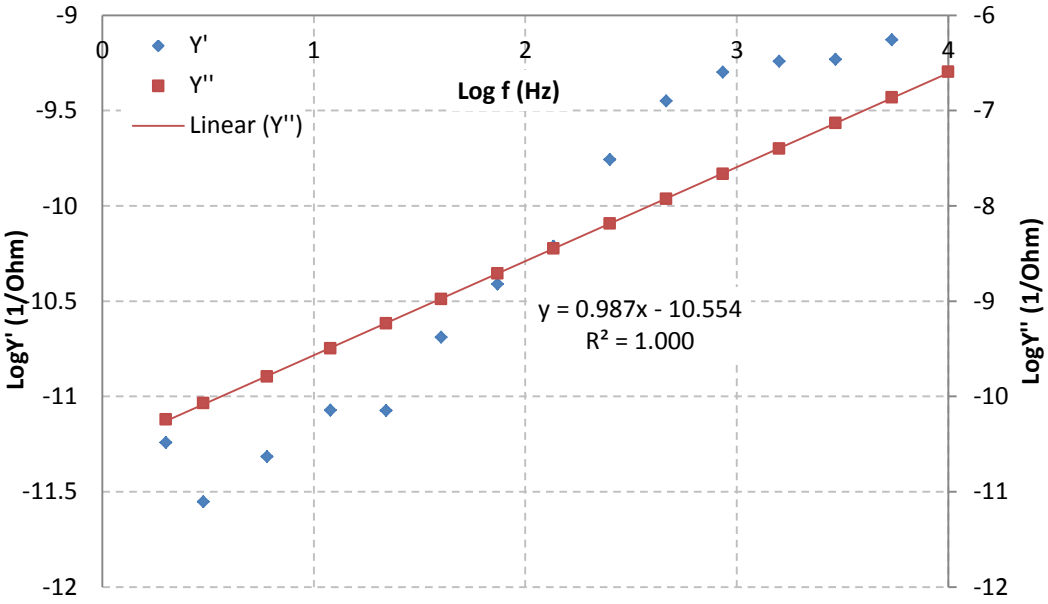
In each case, the recording of the experiment was purposefully started a few minutes before the resin was drawn into the vacuum bag. This allowed the collection of several measures of the dry sensors admittance. An average of the values recorded during this time was calculated for each frequency and the resulting spectra are shown in Figure 6.2.


Y'
Y''
Linear (Y'')
Log f (Hz)
y = 0.9819x - 10.976
R² = 0.9982
LogY' (1/Ohm)
LogY'' (1/Ohm)
-9
-9.5
-10
-10.5
-11
-11.5
-12
-6
-7
-8
-9
-10
-11
-12
0
1
2
3
4

(a)


Y'
Y''
Linear (Y'')
Log f (Hz)
y = 0.9605x - 10.543
R² = 0.9989
LogY' (1/Ohm)
LogY'' (1/Ohm)
-9
-9.5
-10
-10.5
-11
-11.5
-12
-6
-7
-8
-9
-10
-11
-12
0
1
2
3
4

(b)



(c)

Figure 6.2 *Spectra of the real and imaginary admittance of the dry sensor prototype (a) without reinforcement, (b) with 3 layers of glass fibre and (c) with 6 layers of glass fibre*

The imaginary admittance of the three sensors presents a linear relationship with frequency. This is consistent with the parallel RC equivalent circuit described in section 4.4.3. According to the electrical circuit representation, the imaginary admittance is expressed by

$$Y'' = C_{sensor}\omega \tag{6.1}$$

were C_{sensor} is the capacitance of the equivalent circuit and ω is the angular frequency.

For all sensors, the logarithmic plots of Y'' show a slope close to 1, validating the capacitive nature of the imaginary admittance. Using the coefficients of the non-logarithmic curves for the imaginary admittance versus frequency, the capacitances of the different dry sensors can be extracted. They are presented in Table 6.1.

Table 6.1 *Capacitance obtained experimentally for sensor with and without glass fibre reinforcement*

	No reinforcement	3 layers of glass fibre	6 layers of glass fibre
C_{sensor}(Fa)	9.24×10^{-12}	2.17×10^{-11}	2.54×10^{-11}

The addition of glass fibre reinforcement seems to slightly increase the capacitance of the dry sensor. However, the change observed when increasing the number of glass fibre layers is too small to draw clear conclusions.

6.4. Infusion process

The infusion of on top of the sensor prototype was carried out as described in section 5.3.2. Three sets of measurements taken during the wetting of the prototype are presented in the following sections: one set was recorded during an infusion of glycerol only, one during an infusion of epoxy resin through a stack of three layers of glass fibres and the last one during an infusion of epoxy through six layers of glass fibres. The aim of this setting is to validate the results obtained with the new prototype by applying the work of A. Skordos (Skordos *et al.* 2000) to them. The potential influence of glass fibres layers on the sensor response was also investigated.

For the rest of the present research, the four sensors addressed by the dielectric monitoring device are identified as sensor 1 (S_1), sensor 2 (S_2), sensor 3 (S_3) and sensor 4 (S_4). Their numbers correspond to the order in which the infused material (glycerol or epoxy) reaches them. During the infusion of the glycerol, sensor 1 malfunctioned and thus its measures are omitted.

6.4.1. Glycerol

The normalised curves for the real and imaginary part of the admittance versus time at 10 kHz during the infusion of glycerol are shown in Figure 6.3.

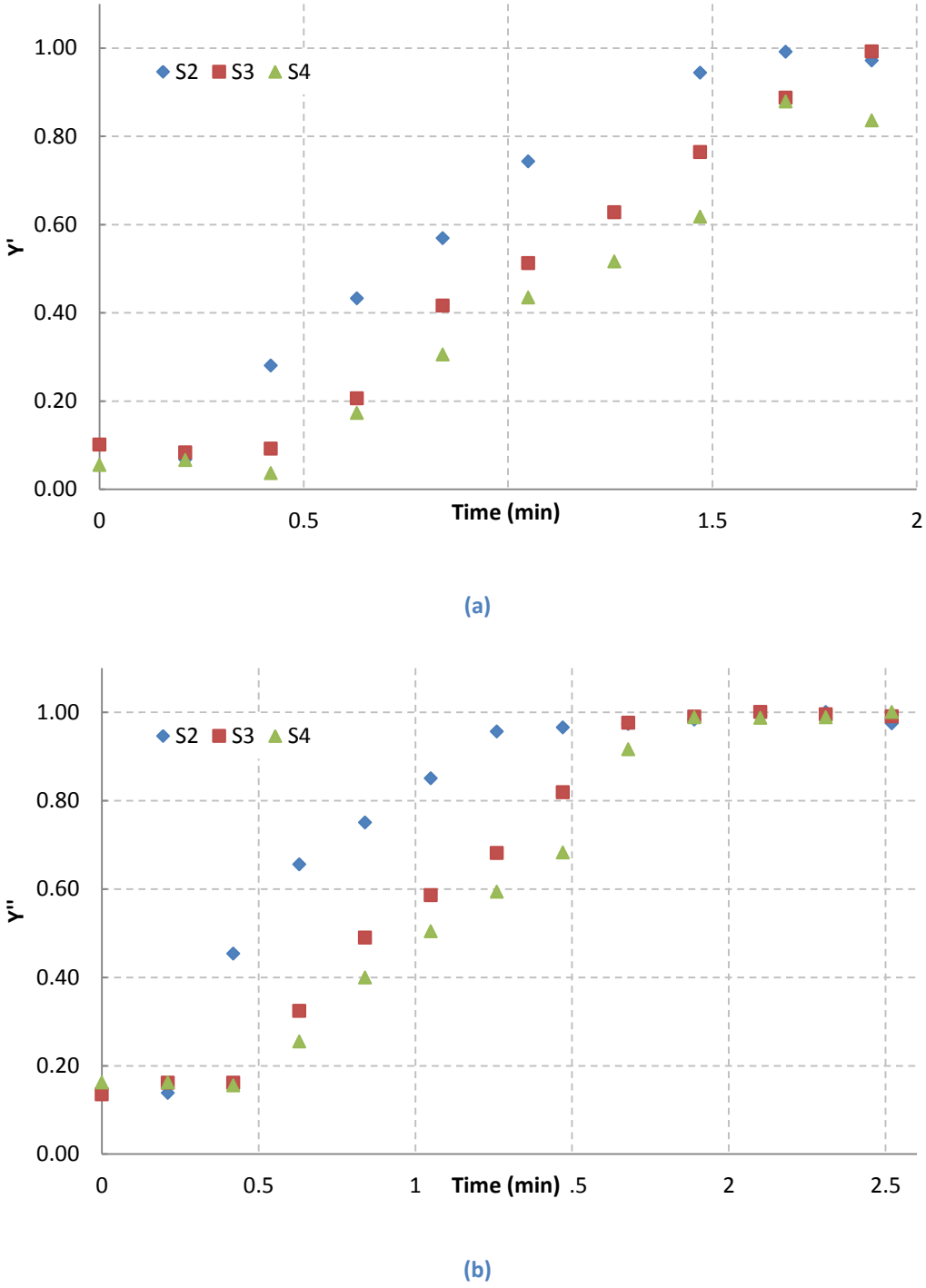


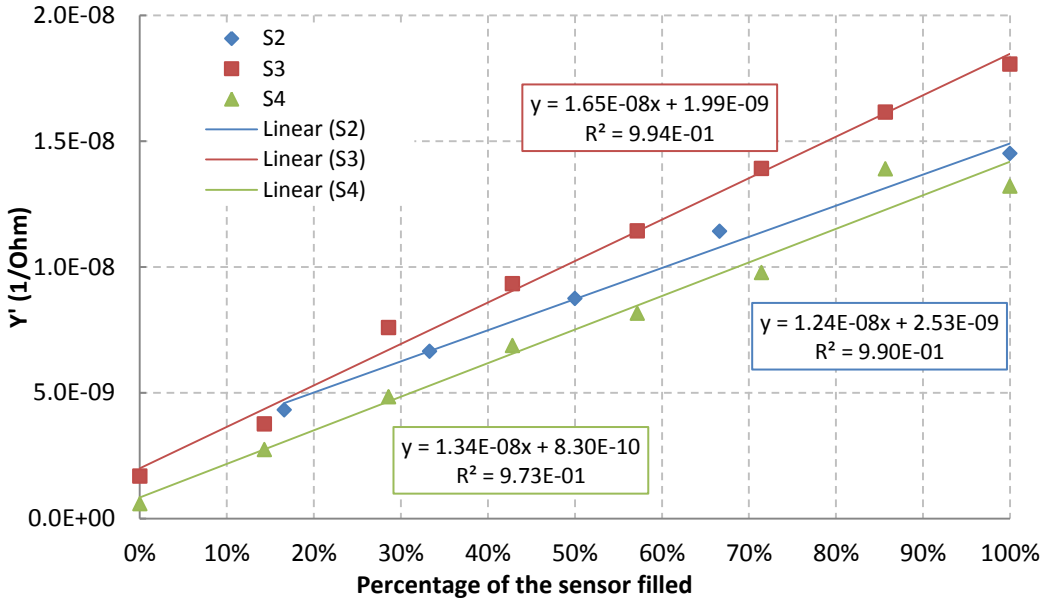
Figure 6.3 *Real (a) and imaginary (b) admittance for three sensors of the final prototype during an infusion of glycerol (normalised)*

The first part of the graphs shows a plateau at a very low value for both Y' and Y'' before the infusion begins. It corresponds to the admittance of the sensor under

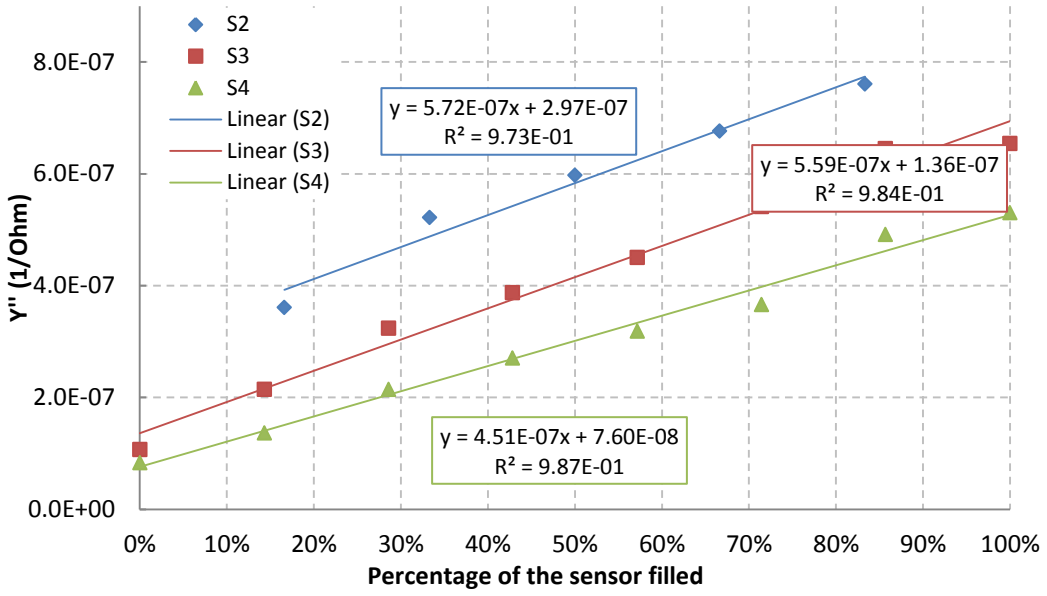
vacuum, before the glycerol is pulled in and the infusion begins, as discussed in section 6.3. When the clench is opened, the glycerol flows and touches the sensors one after the other. As soon as a sensor starts to be covered by glycerol, a jump in both the imaginary and real part of the admittance is observed. Y' and Y'' increase almost linearly as the glycerol progresses along the length of the sensors. The curves reach a second plateau as the infusion is complete and the amount of material covering the sensors no longer varies.

A shift toward higher times is observed between the curves of each sensor. This shift is due to the time it takes the viscous liquid to progress along the sensor array and reach each sensor. The average time delay observed between S_2 and S_4 for an infusion of epoxy resin without reinforcement is 25 seconds.

In order to better study the link between the length of the sensor wetted and the sensor admittance measured, the graph in Figure 6.4 shows the curves for the admittance versus the length of the sensor covered by glycerol. The starting point (0%) is taken just before the liquid touches the first sensor (S_2), and the end point (100%) is taken when the fourth sensor (S_4) is fully covered, or when the glycerol front does not progress anymore and the infusion is considered complete. The determination of the percentage of the sensor wetted is done optically, by using recorded videos of the infusion process.



(a)



(b)

Figure 6.4 *Variations of the real (a) and imaginary (b) admittance versus the length of the sensor filled during an infusion of glycerol*

According to the equation presented in section 5.4.1.1, it is possible to extract a value for the admittance of the sensor both dry and covered by glycerol using the

coefficients of the linear models curves. Those values can be compared to the one obtained experimentally at the beginning and end of the infusion, as shown in Table 6.2.

Table 6.2 *Value for the admittance of the dry sensor obtained with linearization, experimentally and their relative error*

	$Y'_{dry\ calculated}$ (1/Ω)	$Y'_{dry\ experimental}$ (1/Ω)	Relative error	$Y''_{dry\ calculated}$ (1/Ω)	$Y''_{dry\ experimental}$ (1/Ω)	Relative error
S_2	$2.53x10^{-9}$	$4.31x10^{-9}$	41.30%	$2.97x10^{-7}$	$1.17x10^{-7}$	153.85%
S_3	$1.99x10^{-9}$	$1.60x10^{-9}$	24.38%	$1.36x10^{-7}$	$1.07x10^{-7}$	27.10%
S_4	$8.30x10^{-10}$	$8.70x10^{-9}$	4.60%	$7.60x10^{-8}$	$8.62x10^{-8}$	11.83%
	$Y'_{cov\ calculated}$ (1/Ω)	$Y'_{cov\ experimental}$ (1/Ω)	Relative error	$Y''_{cov\ calculated}$ (1/Ω)	$Y''_{cov\ experimental}$ (1/Ω)	Relative error
S_2	$1.49x10^{-8}$	$1.50x10^{-9}$	0.47%	$8.65x10^{-7}$	$7.86x10^{-7}$	10.56%
S_3	$1.85x10^{-8}$	$1.82x10^{-8}$	1.59 %	$6.95x10^{-7}$	$6.60x10^{-7}$	5.30%
S_4	$1.42x10^{-8}$	$1.58x10^{-8}$	9.94%	$5.27x10^{-7}$	$5.37x10^{-7}$	1.86%

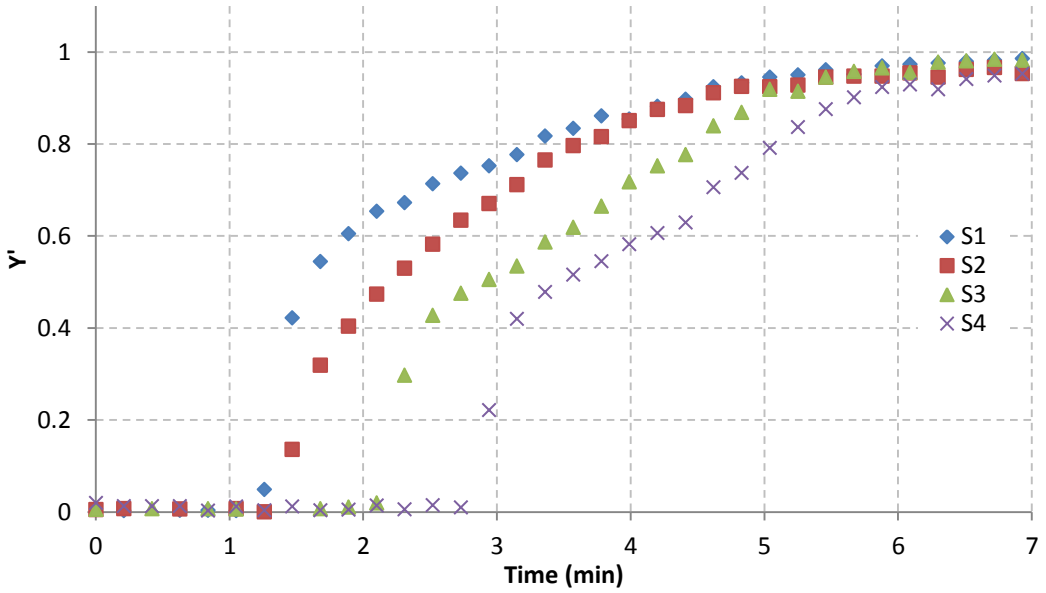
The relative error for the values of Y^*_{dry} is relatively high. It can be explained by the small value of the admittance of the sensor in air. The slightest discrepancy in the values of the linearization curve can have a significant impact on the error. Besides, the infusion without reinforcement is fast (less than two minutes), meaning the human error in the evaluation of the length of the sensor covered by the resin at an instant t is likely to be important.

The relative error observed for the values of Y^*_{tot} is more acceptable except for sensor number 2.

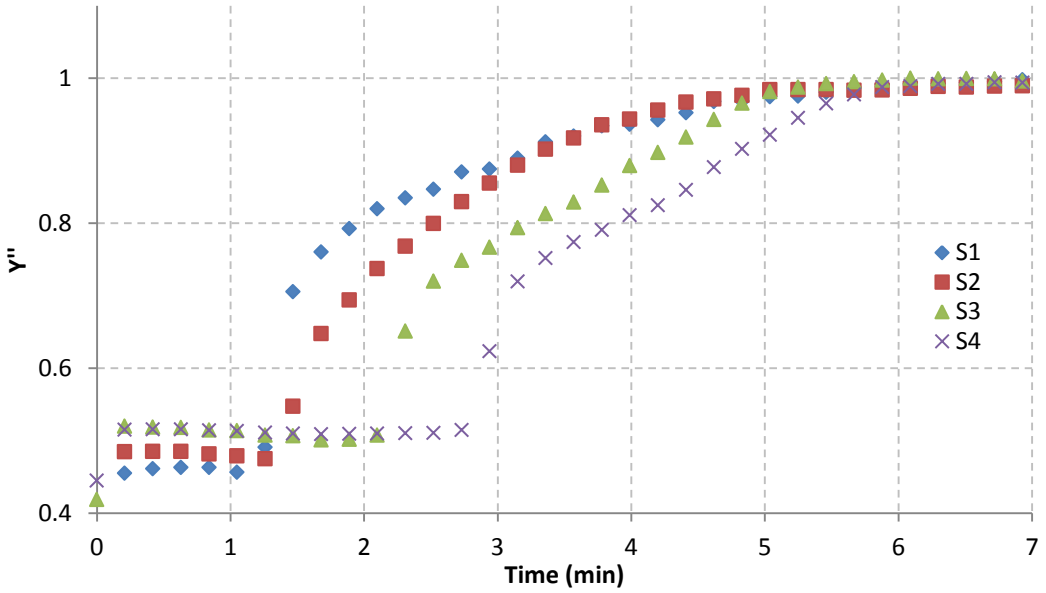
6.4.2. 3 Layers of reinforcement

Three layers of glass fibres were placed into the vacuum bag before infusion. The curves for the real and imaginary part of the admittance versus time at 10 kHz during the resin infusion are shown in Figure 6.5. The shape of the curves exhibits

the plateau before the beginning of the infusion, the linear increase and second plateau at the end of infusion.



(a)



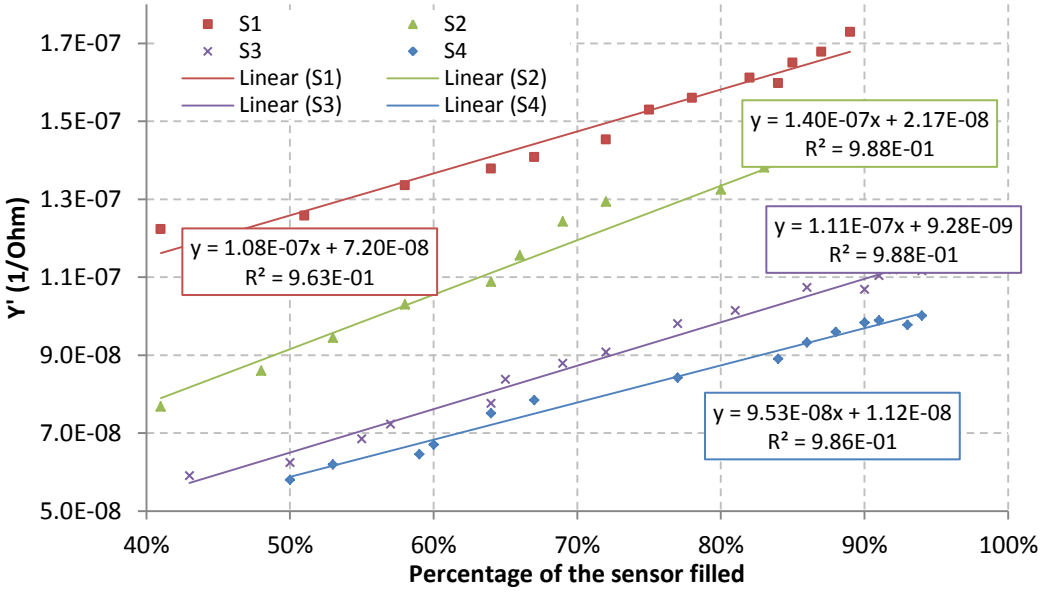
(b)

Figure 6.5 *Variations of the real (a) and imaginary (b) admittance versus time during the infusion of RS-M135 resin through 3 layers of glass fibre reinforcement (normalised)*

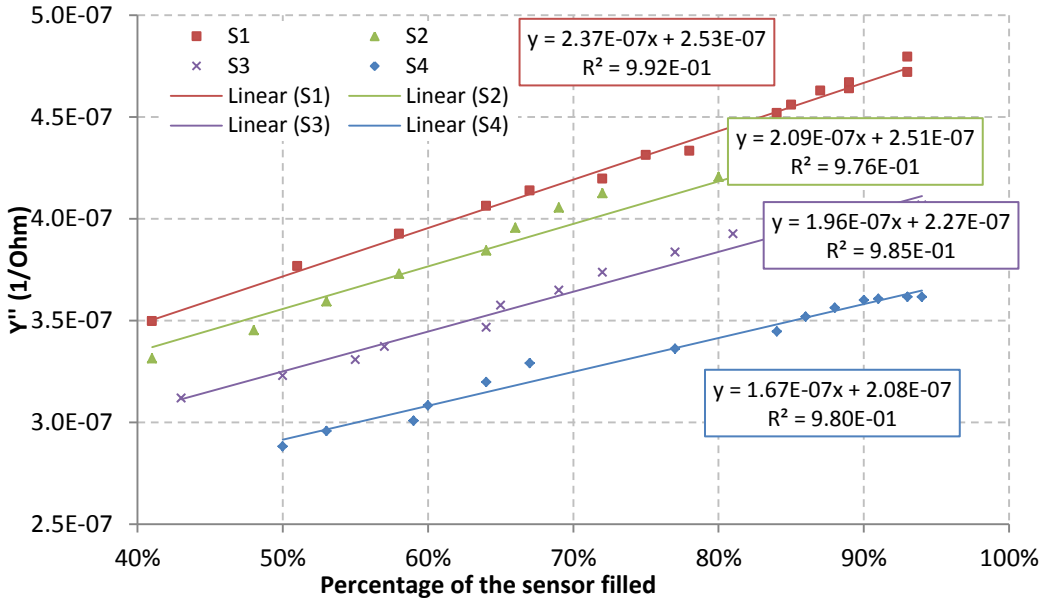
The shift of the curves on the right indicating the interval of time needed for the resin to reach each sensor is still observed. With the addition of glass fibres, the infusion is slower and therefore the time between the wettings of each sensor increases due to the glass fibre reinforcement slowing down the resin progression. Not only do the fibres hinder the flow of the resin, but the amount of resin necessary to fully wet the fibre is greater, thus slowing down the process considering the debit of the resin is constant. The time delay between S_1 and S_2 is around 100s at the beginning of the infusion.

Both the real and imaginary parts of the admittance show a linear increase with the length of the sensor wetted. The linear trend becomes evident only when the percentage of the sensor covered reaches 40 %. This can be explained by the fact the resin does not flow exactly along the electrodes due to the woven reinforcement. Rather, it reaches the sensors slightly perpendicularly because of the diagonal setting of the inlet and outlet, as presented in 5.3.2. Therefore, at the time the two electrodes of each sensor are simultaneously covered by the resin and the electric field is established through it, the sensor might already be partially covered. This is especially true in the case of sensor 3 and 4, further from the entry point of the epoxy.

In order to validate the linear relationship between the admittance and the length of the sensor covered, linear trend lines are added to the curves between 40% and 100% wetting, as shown in Figure 6.6.



(a)



(b)

Figure 6.6 *Real (a) and imaginary (b) admittance versus percentage of the sensor wetted during the infusion of RS-M135 resin through 6 layers of glass fibre reinforcement*

The values for Y'_{dry}, Y''_{dry} Y'_{tot} and Y''_{tot} are once again calculated from the parameters of the respective linear trends and compared to the experimental values. The results are shown in Table 6.3.

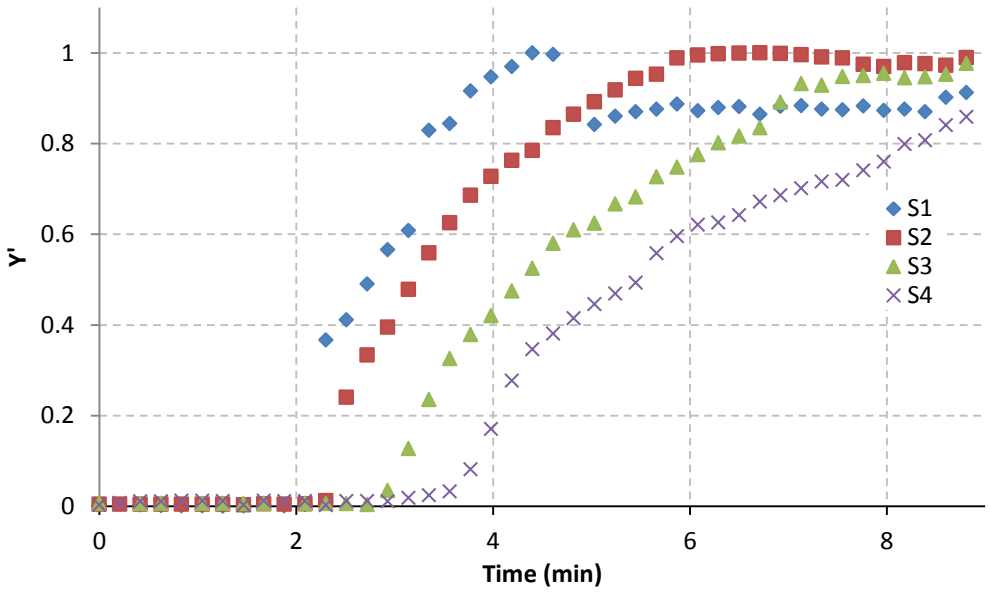
Table 6.3 *Value for the admittance of the dry sensor with 3 layers of glass fibres obtained with linearization, experimentally and their relative error*

	$Y'_{dry\ calculated}$ (1/Ω)	$Y'_{dry\ experimental}$ (1/Ω)	Relative error	$Y''_{dry\ calculated}$ (1/Ω)	$Y''_{dry\ experimental}$ (1/Ω)	Relative error
S_1	$7.20x10^{-8}$	$6.00x10^{-10}$	11900.00%	$2.53x10^{-7}$	$2.29x10^{-7}$	10.48%
S_2	$2.17x10^{-8}$	$1.00x10^{-9}$	2070.00%	$2.51x10^{-7}$	$2.18x10^{-7}$	15.14%
S_3	$9.28x10^{-9}$	$8.00x10^{-10}$	1060.00%	$2.27x10^{-7}$	$2.11x10^{-7}$	7.58%
S_4	$1.12x10^{-8}$	$1.30x10^{-9}$	761.54%	$2.08x10^{-8}$	$1.88x10^{-8}$	10.64%
	$Y'_{tot\ calculated}$ (1/Ω)	$Y'_{tot\ experimental}$ (1/Ω)	Relative error	$Y''_{tot\ calculated}$ (1/Ω)	$Y''_{tot\ experimental}$ (1/Ω)	Relative error
S_1	$1.80x10^{-7}$	$1.85x10^{-7}$	2.70%	$4.90x10^{-7}$	$4.90x10^{-7}$	0.00%
S_2	$1.62x10^{-7}$	$1.55x10^{-7}$	4.32%	$4.60x10^{-7}$	$4.50x10^{-7}$	2.22%
S_3	$1.20x10^{-7}$	$1.15x10^{-7}$	4.59%	$4.23x10^{-7}$	$4.05x10^{-7}$	4.44%
S_4	$1.07x10^{-7}$	$1.00x10^{-7}$	6.50%	$3.75x10^{-7}$	$3.63x10^{-7}$	3.31%

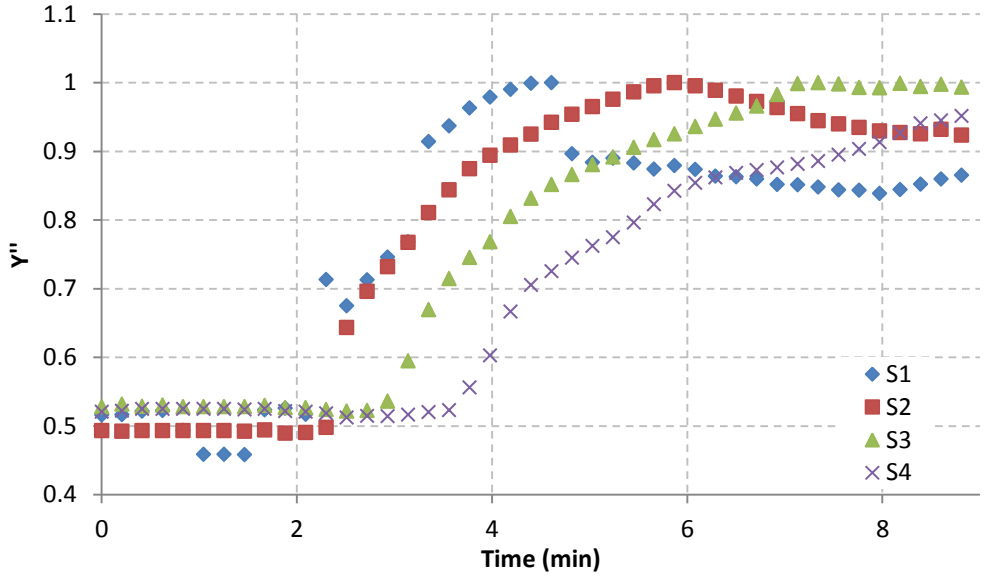
A large relative error for Y'_{dry} is observed due to the very small experimental value, at the very limit of the apparatus detection. Y'' being two orders of magnitude higher than Y', the experimental values are more stable and this translates to a better relative error. The addition of glass fibre reinforcement seems to increase the incertitude on the measures.

6.4.3. 6 Layers of reinforcement

To investigate the influence of the number of reinforcement layers on the admittance measured, an infusion was done through 6 layers of glass fibres stacked on top of the sensor array. The normalised curves for the real and imaginary part of the admittance versus time at 10 kHz are shown in Figure 6.7. Once again, all the curves exhibit a plateau before the beginning of the infusion, a linear increase and a second plateau at the end of infusion.



(a)



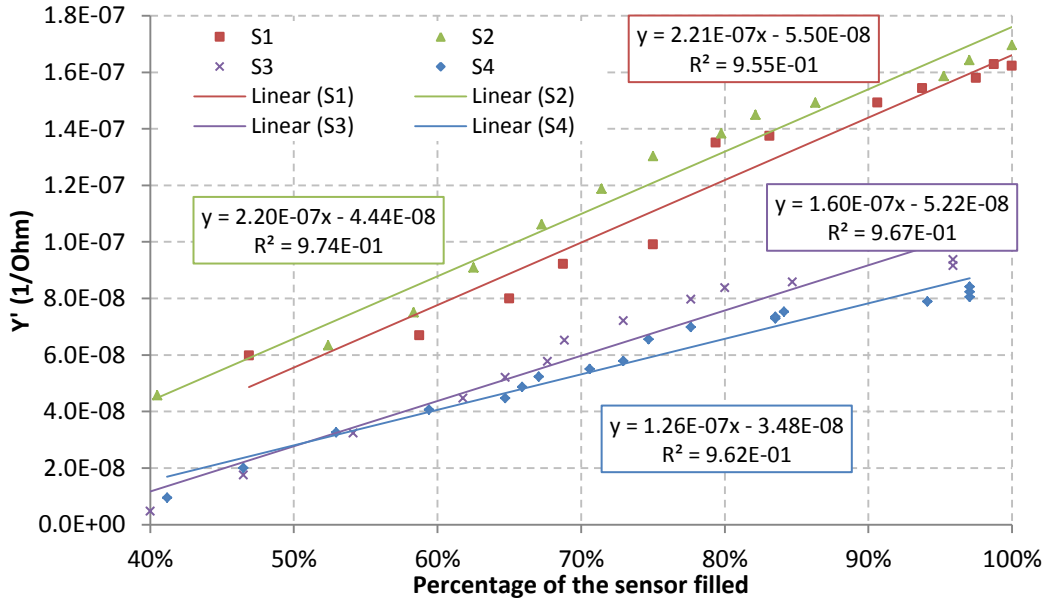
(b)

Figure 6.7 *Variations of the real (a) and imaginary (b) admittance versus time during the infusion of RS-M135 resin through 6 layers of glass fibre reinforcement (normalised)*

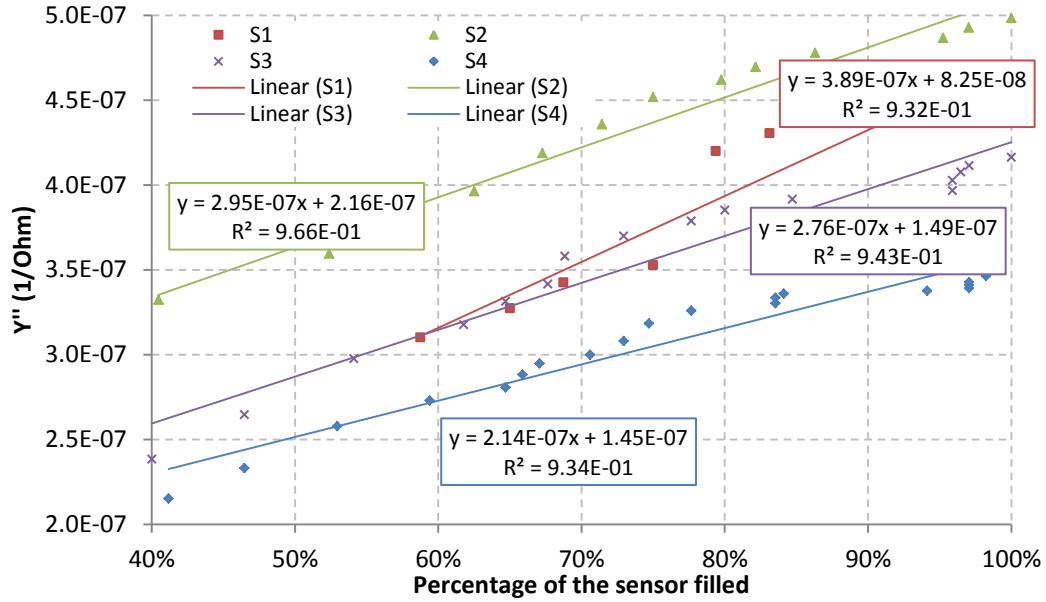
The shift of the curves on the right is still visible, but the time delay between S_1 and S_4 is increased by 25 seconds compared to the infusion with 3 layers of glass fibres. Effectively, the epoxy resin flows in three dimensions, wetting the reinforcement through the z axis as well as flowing on the sensor surface. It is conceivable that adding layers of reinforcement means more resin is necessary to wet the same length of the sensor, because of the material absorbed by the additional fabric. This would explain the extended infusion time observed.

The curves presented in Figure 6.7 show some anomalies in their shape, especially in the case of S_1. This is due to a minor leak in the vacuum bag, detected and repaired at the end of the infusion, before cure.

The linearity of the signal during infusion with is nonetheless observed after 40% of the sensors are covered. This is further displayed in Figure 6.8.



(a)



(b)

Figure 6.8 *Real (a) and imaginary (b) admittance versus percentage of the sensor wetted during the infusion of RS-M135 resin through 6 layers of glass fibre reinforcement*

As previously discussed, the values for Y'_{dry}, Y''_{dry} Y'_{tot} and Y''_{tot} can be calculated from the linearization of the curves and compared to the experimental values, as shown in Table 6.4.

A large relative error for Y'dry is observed, similarly to the experiment using 3 layers of glass fibres, for the same reasons. However, the discrepancy between experimental and linearized values remains high, except for Y''tot which is acceptable. The aforementioned leak is likely to have had an impact on the measured values as well.

Table 6.4 *Value of the admittance of the dry sensor with 6 layers of glass fibres obtained with linearization, experimentally and their relative error*

	$Y'_{dry\ calculated}$ (1/Ω)	$Y'_{dry\ experimental}$ (1/Ω)	Relative error	$Y''_{dry\ calculated}$ (1/Ω)	$Y''_{dry\ experimental}$ (1/Ω)	Relative error
S_1	-5.50×10^{-8}	2.20×10^{-10}	27600.00%	8.25×10^{-8}	2.20×10^{-7}	62.50%
S_2	-4.44×10^{-8}	9.00×10^{-10}	4988.89%	2.16×10^{-7}	2.55×10^{-7}	15.29%
S_3	-5.22×10^{-8}	9.70×10^{-10}	5481.44%	1.49×10^{-7}	2.35×10^{-7}	36.60%
S_4	-3.48×10^{-8}	1.40×10^{-9}	2585.71%	1.45×10^{-7}	$2.03.10^{-7}$	28.57%

	$Y'_{tot\ calculated}$ (1/Ω)	$Y'_{tot\ experimental}$ (1/Ω)	Relative error	$Y''_{tot\ calculated}$ (1/Ω)	$Y''_{tot\ experimental}$ (1/Ω)	Relative error
S_1	1.66×10^{-7}	1.49×10^{-7}	11.41%	4.72×10^{-7}	4.95×10^{-7}	2.72%
S_2	1.76×10^{-7}	1.90×10^{-7}	7.37%	5.11×10^{-7}	5.17×10^{-7}	1.16%
S_3	1.08×10^{-7}	1.36×10^{-7}	20.74%	4.22×10^{-7}	4.45×10^{-7}	5.17%
S_4	9.12×10^{-8}	1.17×10^{-7}	22.05%	3.59×10^{-7}	3.17×10^{-7}	13.25%

The addition of glass fibres does not make a significant difference in the values of the admittance measured, and does not prevent the prototype to follow the infusion process. However, it seems to have an impact on the incertitude of the dielectric measures, especially for smaller values of the admittance.

The design of the prototype, an array of sensors disposed at different points of the infusion mould, can be used to follow the filling of the mould on a 2D scale. By interrogating couples of electrodes placed at various distances from the entry point of the resin, the flow can be monitored not only along the length of the electrodes, but also across the group of sensors, thus effectively giving access to the flow in two dimensions.

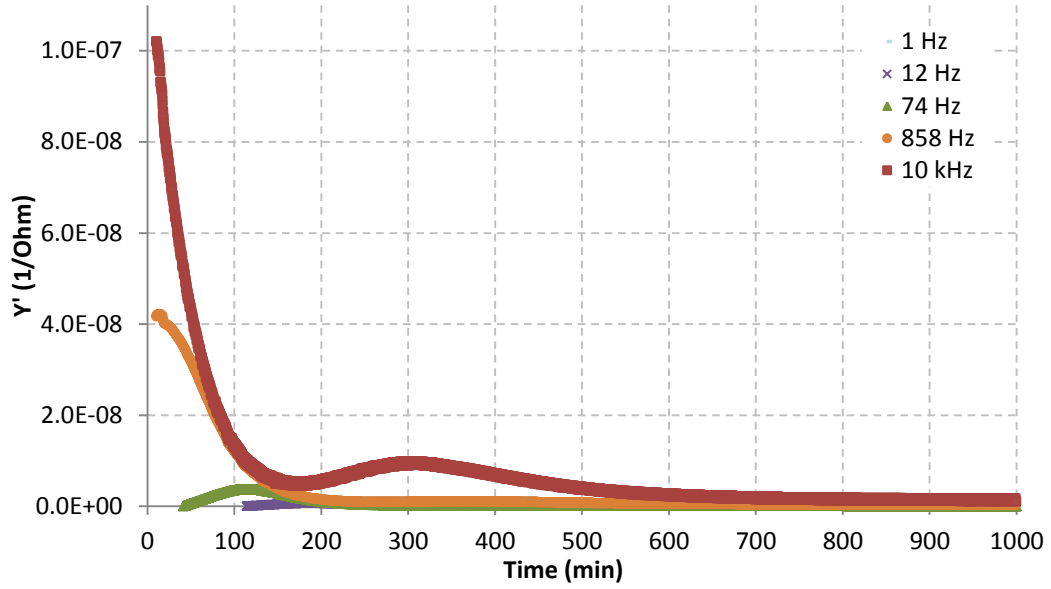
6.5. Composite cure

After the infusions presented in section 6.4, the resin was left to cure at ambient temperature for 24 hours as described in section 5.3.2. The imaginary admittance was recorded for different frequencies along the whole reaction.

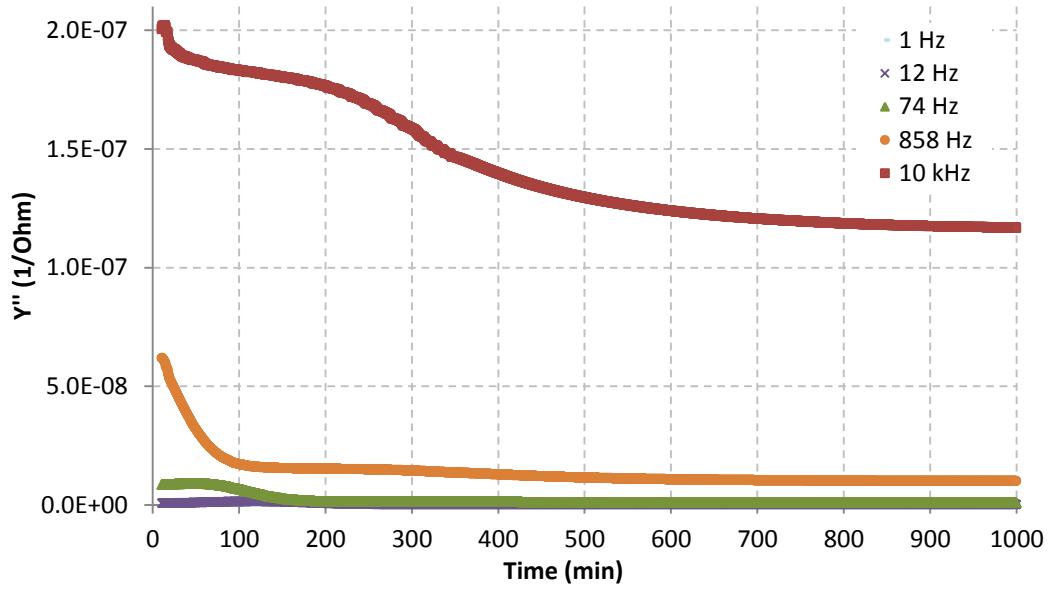
Each experiment provided four sets of data corresponding to the four sensors addressed by the c-Diemos. For the sake of clarity, the following paragraphs will present only one of each set of results.

6.5.1. Epoxy only

The curves obtained while monitoring the imaginary admittance during the cure of the unreinforced epoxy resin are shown in Figure 6.9. The response of one sensor for five different frequencies is presented.



(a)



(b)

Figure 6.9 *Real (a) an imaginary (b) admittance variations during the cure of RS-M135 resin*

The higher values for both the real and imaginary parts of the admittance are obtained for a frequency of 10 kHz, with Y' and Y'' reaching a maximum of respectively $10.6x10^{-7}$ Ω^{-1} and $3.00x10^{-7}$ Ω^{-1}. Smaller values of the excitation frequencies lead to smaller values of the admittance.

For 858 Hz and 10 kHz, the admittance decreases as the cure progresses with time before reaching a plateau value. Between 200 and 400 minutes of cure, the curve for Y' present a local maximum, and the curve for Y'' shows an inflexion point. The curves obtained for lower frequencies do not seem to exhibit the same behaviour, but this cannot be clearly seen on the previous graphs due to the important difference between the values obtained at high and low frequencies. At the beginning of the cure, the values obtained for Y' for 1.2 Hz and 74 Hz are below the detection range of the c-Diemos. Therefore, they are not visible on the plot.

When the same curves are plotted on a logarithmic scale, the difference in the shape of the curves with frequency is made more obvious, as shown in Figure 6.10.

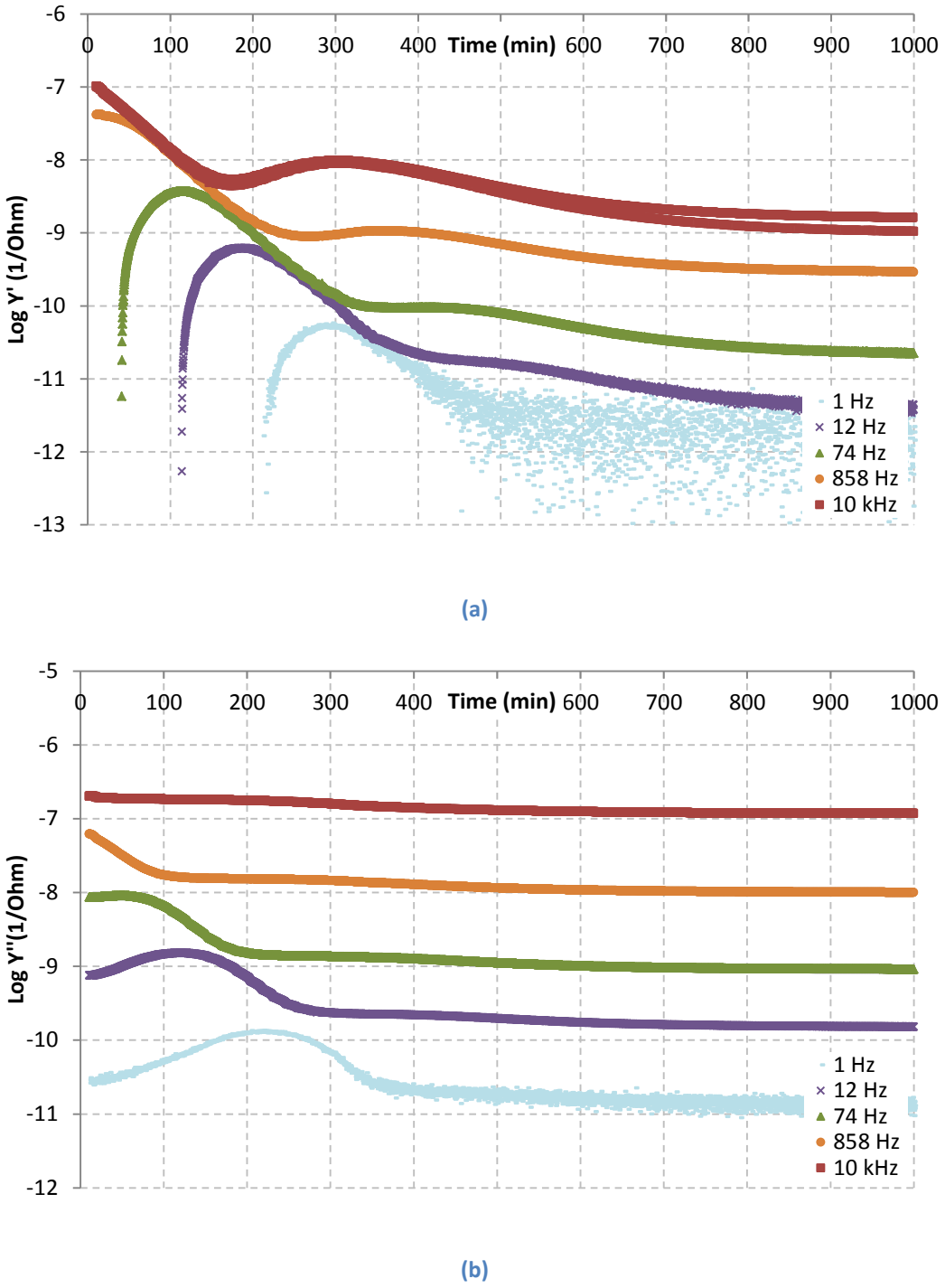


Figure 6.10 *Variations of the real (a) an imaginary (b) admittance during the cure of RS-M135 resin (logarithmic scale)*

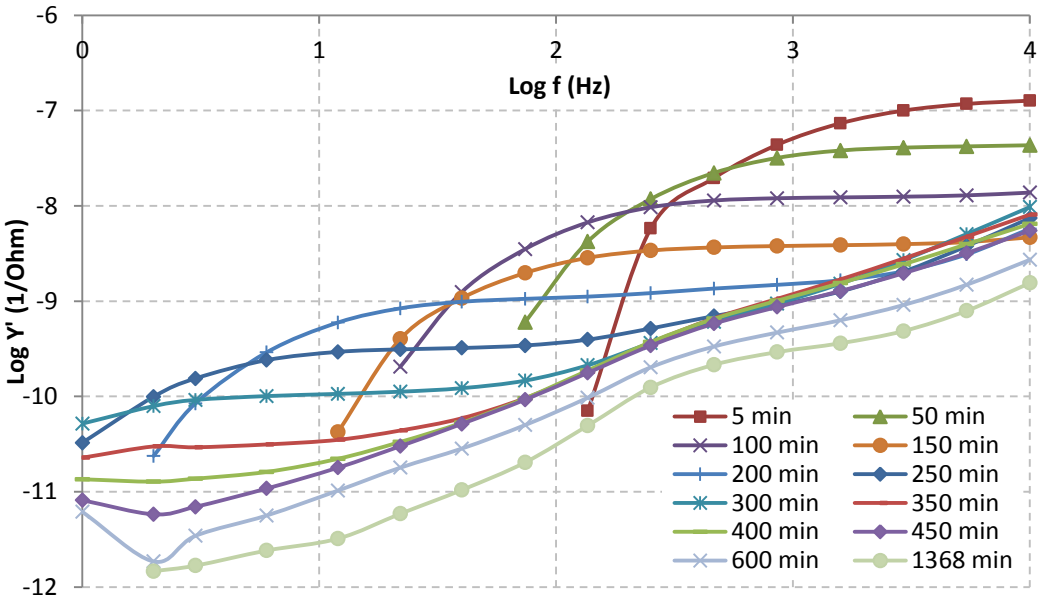
The real admittance curves present a local maximum at high frequencies. This local maximum decreases in amplitude and shifts towards higher values of time as

the frequency of excitation decreases. The curve obtained for Y' at 1 Hz presents noise, likely due to the c-Diemos apparatus detection range. The curve of the real part of the admittance recorded at 10 kHz presents a split near the end of the infusion. It is likely created by the sensor and does not correspond to the resin cure reaction mechanism.

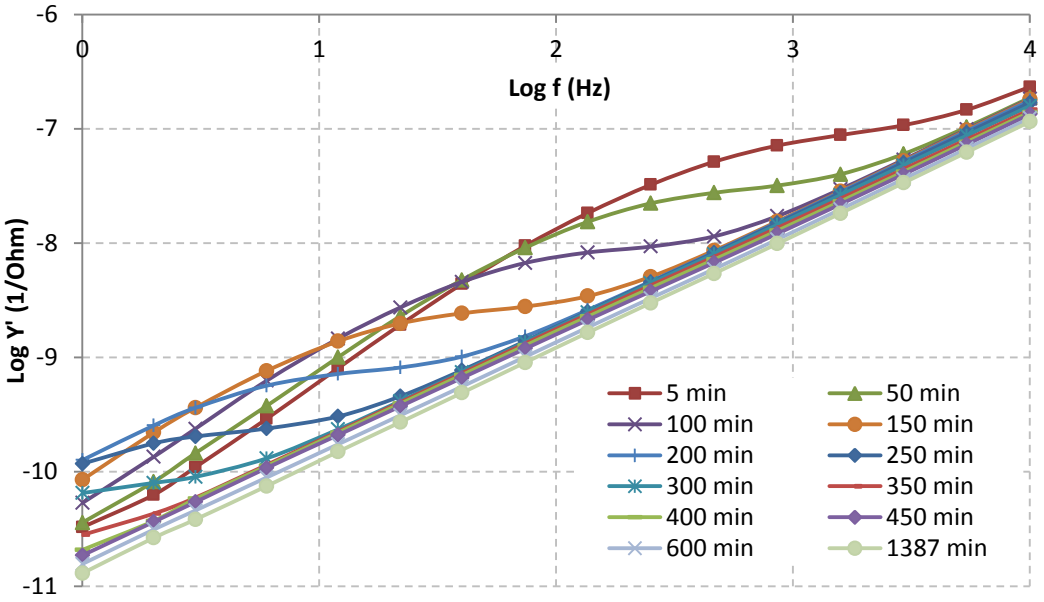
The imaginary admittance curves likewise present local maximums moving toward higher values of time as the frequency decreases. However, their amplitude does not seem to vary with the frequency. The signal obtained at 1 Hz also presents noise when the values of the admittance reach the c-Diemos lower limit of detection.

The local maximum of the admittance correspond to the dipolar relaxation (Gallone *et al.* 2001; Nixdorf and Busse 2001). Despite being averaged for modelisation purposes, the relaxation of the different dipoles present in the epoxy resin (see section 4.3.3) actually occurs with different characteristic times depending on the mobility and the surroundings of the dipoles. At the beginning of the cure, ionic conductivity dominates the signal, as discussed in section 4.3.1. However, the resin cure hinders the circulation of charges by increasing the molecular weight of the polymer, then forming the 3D network. At that point, the dipolar contribution to the dielectric signal becomes visible. The dipoles are however affected by the solidification of the resin as well: their orientation becomes more difficult as the crosslinking reaction takes place, leading to the modification of their characteristic time and the eventual decrease in their signal.

In order to better investigate the relationship between admittance and frequency, the spectra of the admittance at different time of cure is presented in Figure 6.11.



(a)



(b)

Figure 6.11 *Spectra of the real (a) and imaginary (b) admittance during the cure of the of RS-M135 resin*

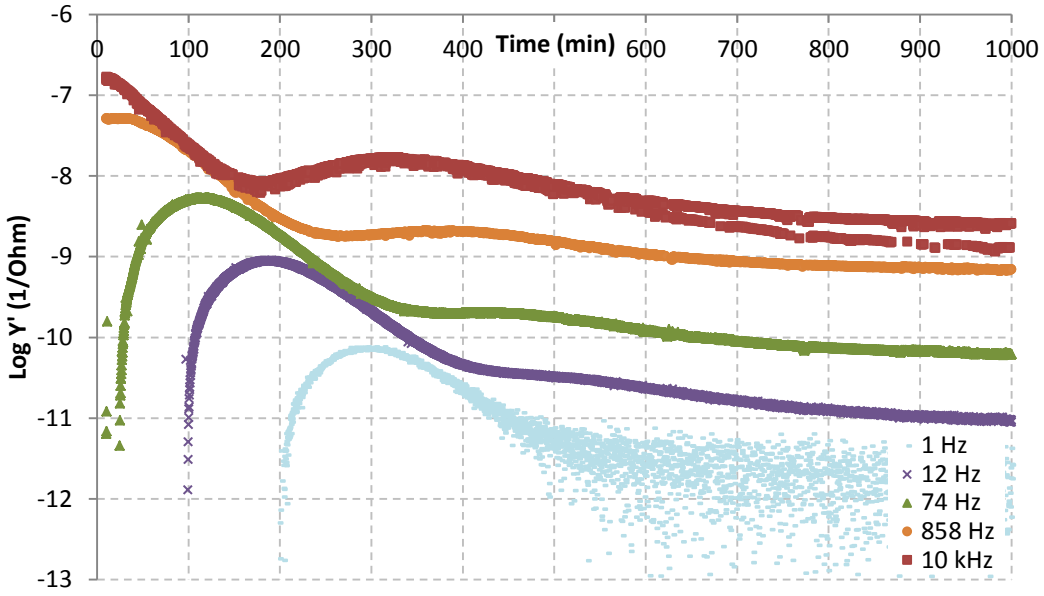
The spectra obtained are similar to the ones presented in section 4.4.2.4, thus validating the hypothesis of a predominance of the ionic conductivity contribution

to the permittivity of the resin studied. They are however not exactly the same, thus corroborating that the dipoles relaxation does play a role in the signal while the cure is happening, albeit minor.

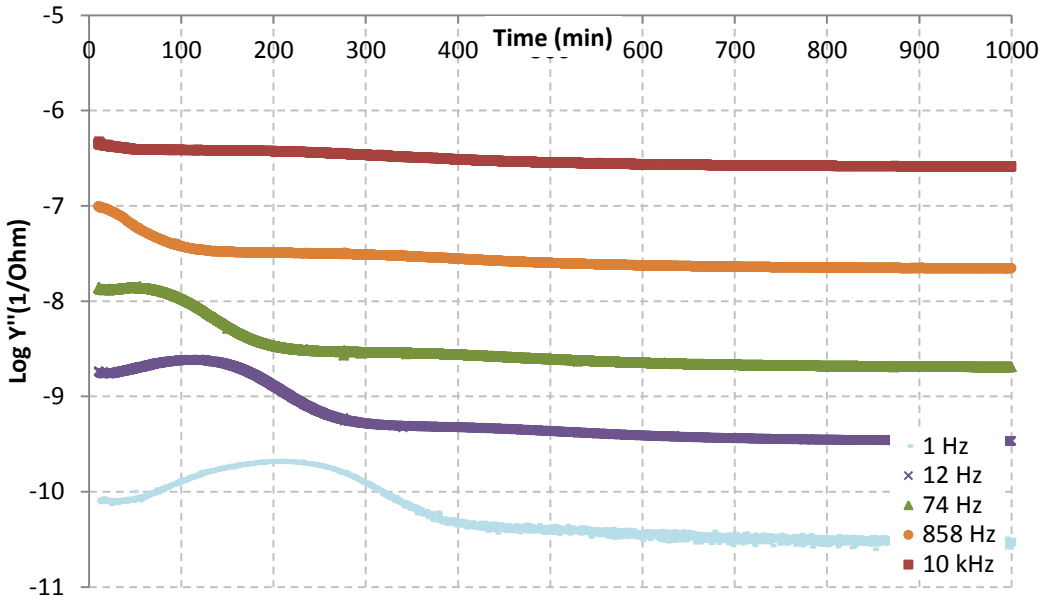
For the frequency range studied, the imaginary part of the admittance shows a linear trend at the end of the cure, thus translating the capacitive nature of the cured resin. This will be discussed further in section 6.6.

6.5.2. 3 Layers of glass fibres

The impact of glass fibre reinforcement on the dielectric measurements during cure is studied by infusing reinforced composite plates. The curves obtained when following the admittance versus time for an infusion realised stacking 3 layers of glass fibres on top of the sensor grid are shown in Figure 6.12.



(a)

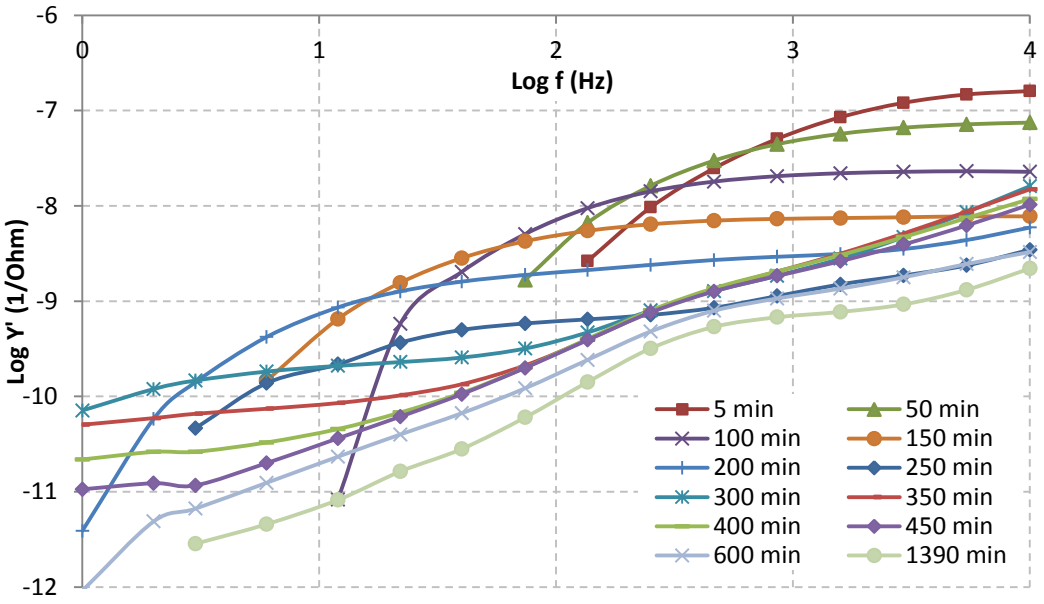


(b)

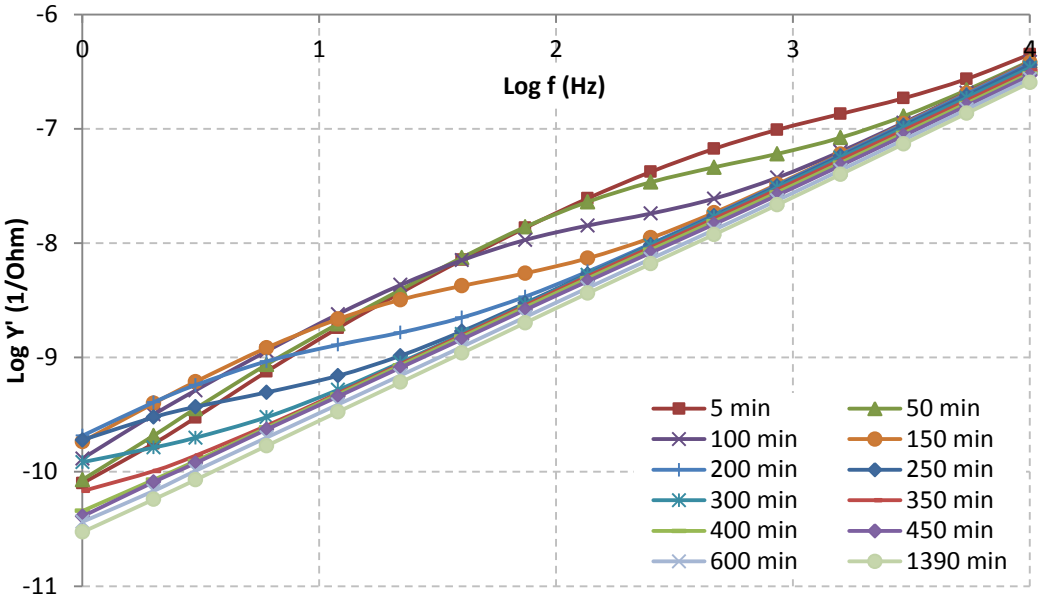
Figure 6.12 *Variations of the real (a) an imaginary (b) admittance during the cure of RS-M135 resin reinforced with 3 layers of woven glass fibre fabric*

Despite a noisier signal, especially at 10 kHz, the shapes of the curves remain similar to the ones obtained for the epoxy resin, thus proving the flexible sensor developed is capable of following the cure of glass fibre reinforced composites. The dipolar relaxation are still visible, corroborating the work of Nixdorf and Busse on the influence on glass fibre reinforcement of epoxies permittivity (Nixdorf and Busse 2001).

The spectra for the cure of the three layer reinforced composite are shown in Figure 6.13. The spectra obtained along the cure of a glass fibre reinforced epoxy matrix are similar to the ones obtained for the unreinforced resin. The glass fibre reinforcement does not seem to affect the resin cure mechanism, nor hinder the monitoring of the cure with the sensor prototype developed.



(a)



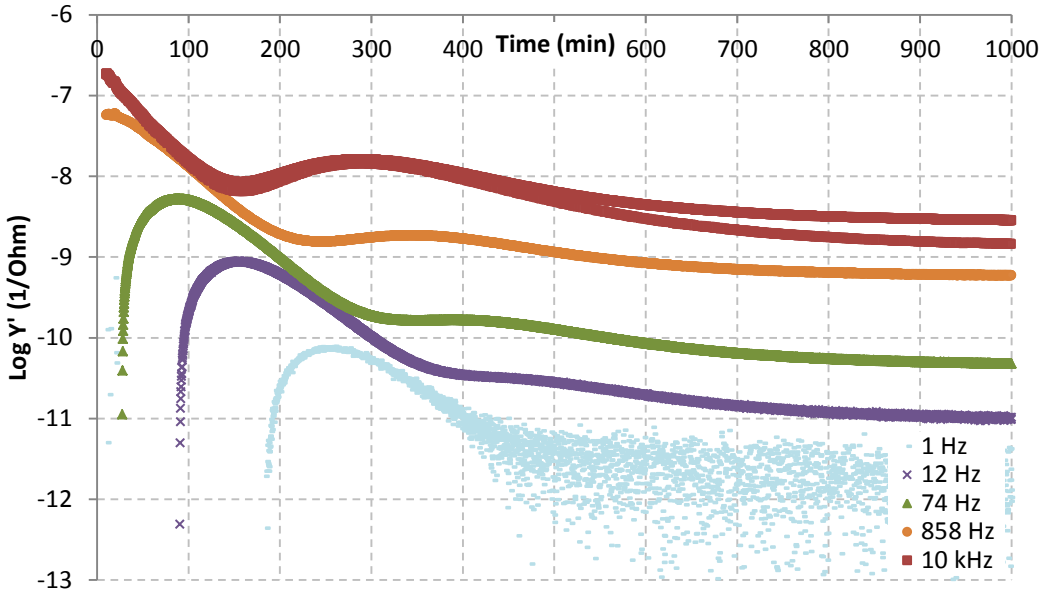
(b)

Figure 6.13 *Spectra of the real (a) and imaginary (b) admittance during the cure of the of RS-M135 resin reinforced with 3 layers of woven glass fibre*

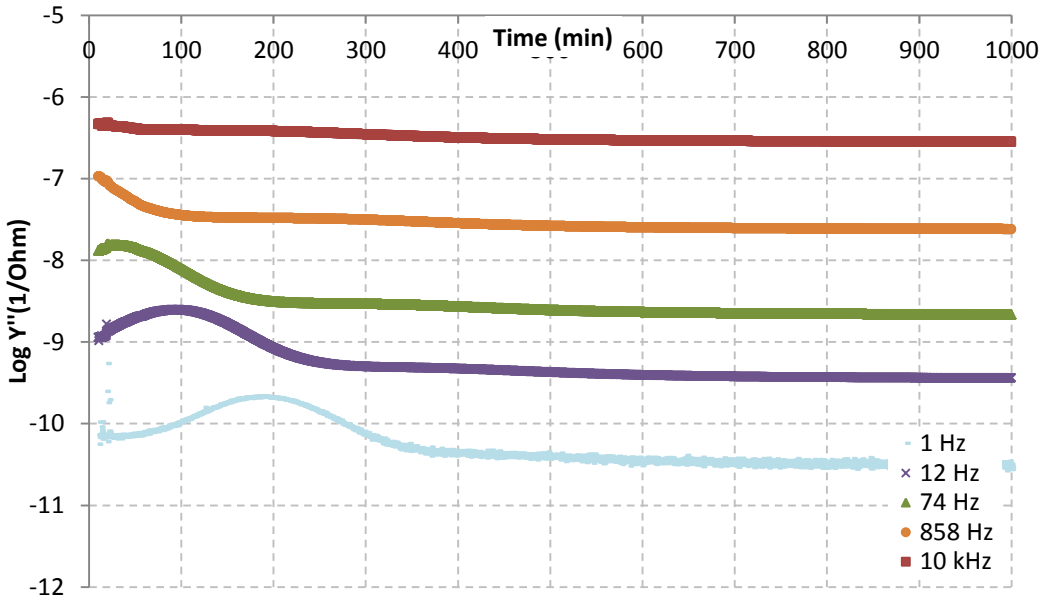
6.5.3. 6 layers of glass fibres

In order to investigate the impact of the number of reinforcement layers in the composite on the dielectric measurements, the fabrication of a composite plate reinforced with 6 layers of woven glass fibres is monitored. The curves obtained during the process are presented in Figure 6.14.

The signal obtained shows the characteristic shape of the curves described in the previous section for the composite with three layers of glass fibres. No noticeable variations of the admittance between the two sets of measurements are observable.



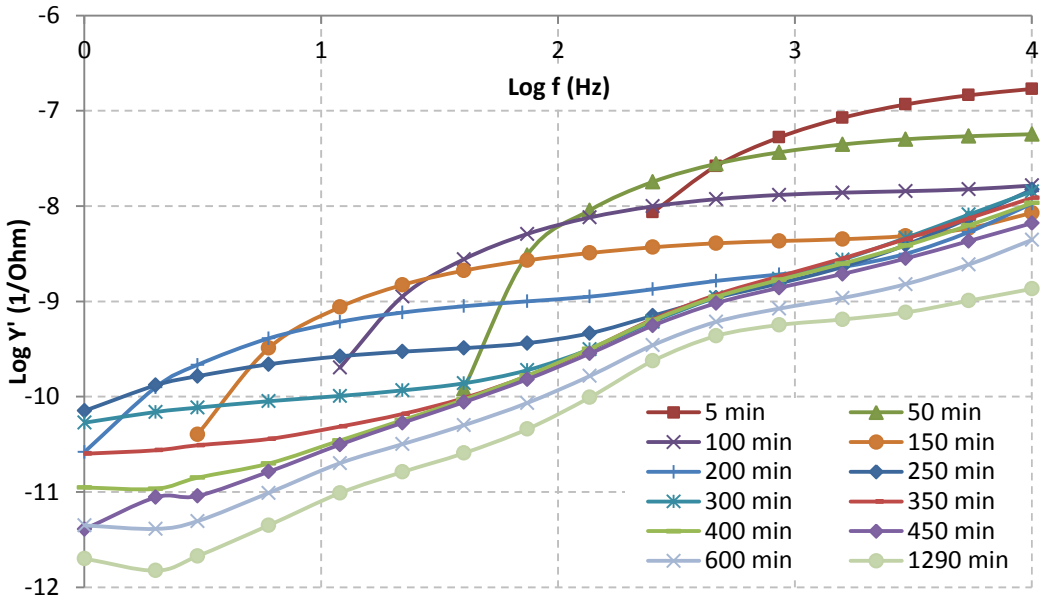
(a)



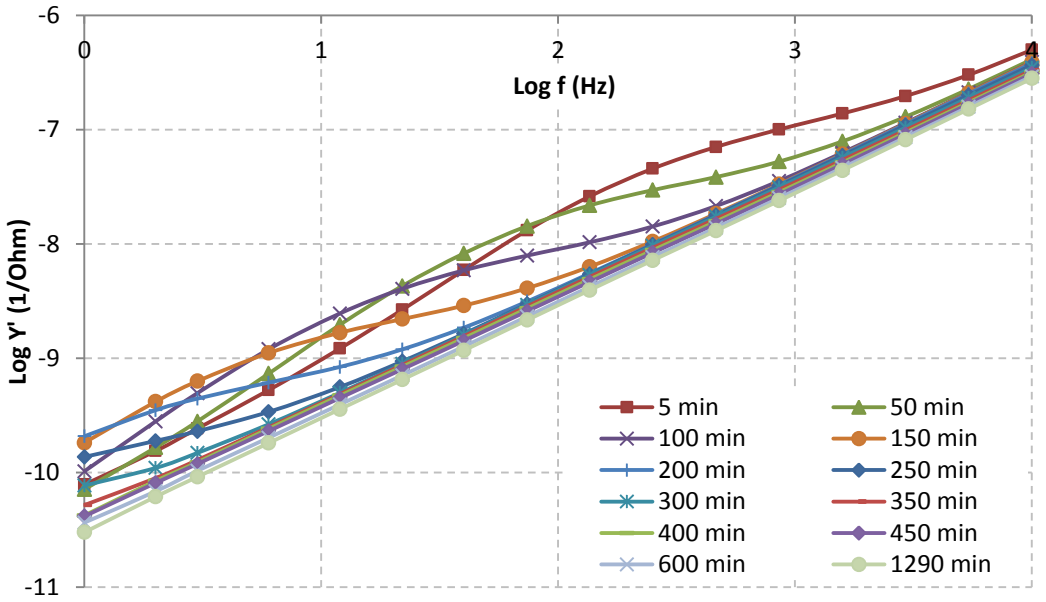
(b)

Figure 6.14 *Variations of the real (a) an imaginary (b) admittance during the cure of RS-M135 resin reinforced with 6 layers of woven glass fibre fabric*

The spectra for the admittance at different points during the cure is presented in Figure 6.15.



(a)



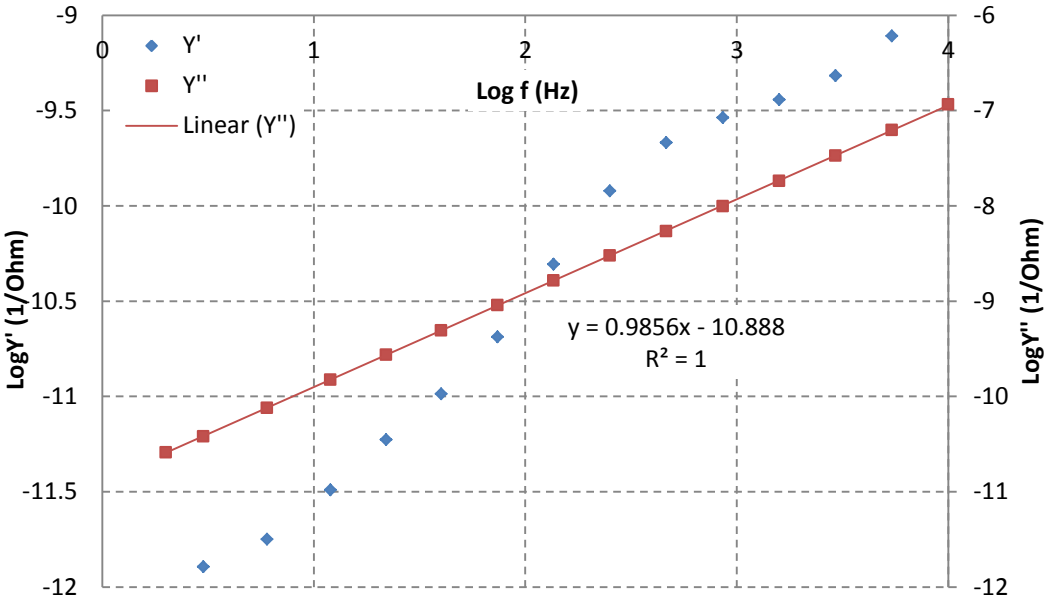
(b)

Figure 6.15 *Spectra of the real (a) and imaginary (b) admittance during the cure of the of RS-M135 resin reinforced with 6 layers of woven glass fibre*

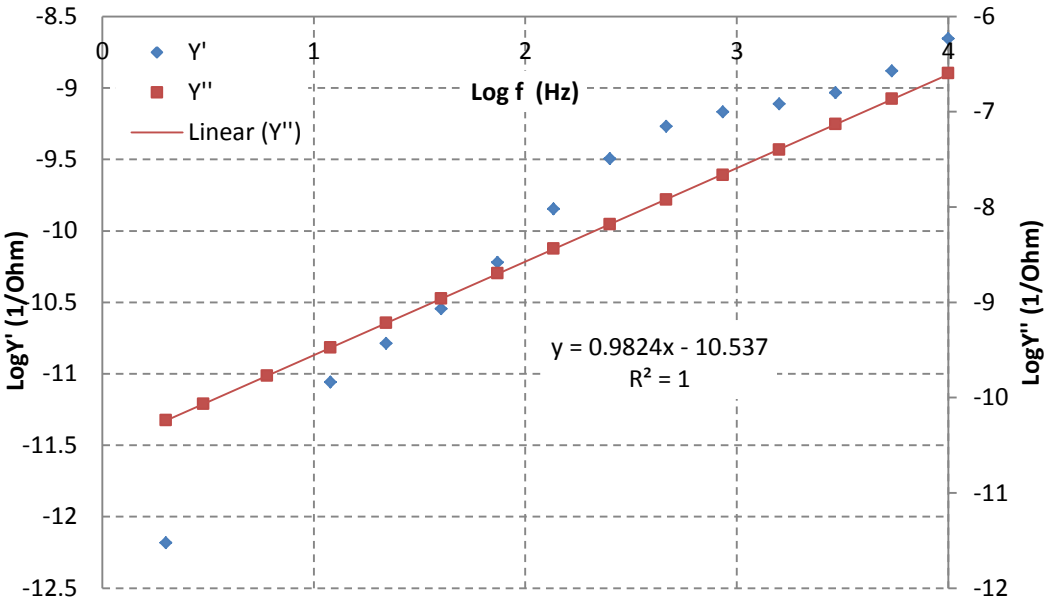
Similarly to the spectra obtained with 3 layers of reinforcement, the spectra are coherent with the cure mechanism of the epoxy resin. The number of glass fibre reinforcement layers does not seem to affect the sensor ability to follow the cure.

6.6. Prototype characterisation at the end of the cure

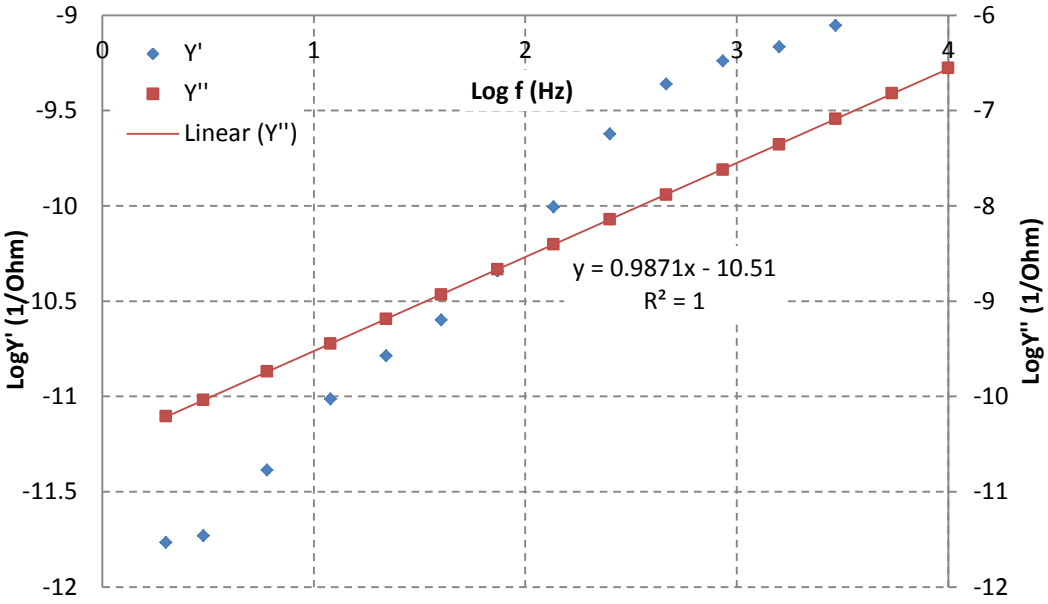
The admittance obtained at the end of the cure of the epoxy, the 3 layer of glass fibres composite plate and the 6 layers of glass fibres composite plate are presented in Figure 6.16.


Y'
Y''
Linear (Y'')
Log f (Hz)
y = 0.9856x - 10.888
R² = 1
LogY' (1/Ohm)
LogY'' (1/Ohm)
-9
-9.5
-10
-10.5
-11
-11.5
-12
-6
-7
-8
-9
-10
-11
-12
0
1
2
3
4

(a)


Y'
Y''
Linear (Y'')
Log f (Hz)
y = 0.9824x - 10.537
R² = 1
LogY' (1/Ohm)
LogY'' (1/Ohm)
-8.5
-9
-9.5
-10
-10.5
-11
-11.5
-12
-12.5
-6
-7
-8
-9
-10
-11
-12
0
1
2
3
4

(b)



(c)

Figure 6.16 *Spectra of the real and imaginary admittance of the sensor prototype after full cure of the RS-M135 epoxy resin (a) without reinforcement, (b) with 3 layers of glass fibres and (c) with 6 layers of glass fibres*

As seen in section 6.3, Y'' presents a linear relation with the frequency. For the three sensors, the slope of the curve is close to 1, implying the RC electrical circuit is valid model for a sensor covered in cured resin, either with or without glass fibre reinforcement.

The capacitances of the different systems at the end of the resin cure are extracted from the experimental data and their variations from the dry sensors capacitance (given in Table 6.1) are presented in Table 6.5.

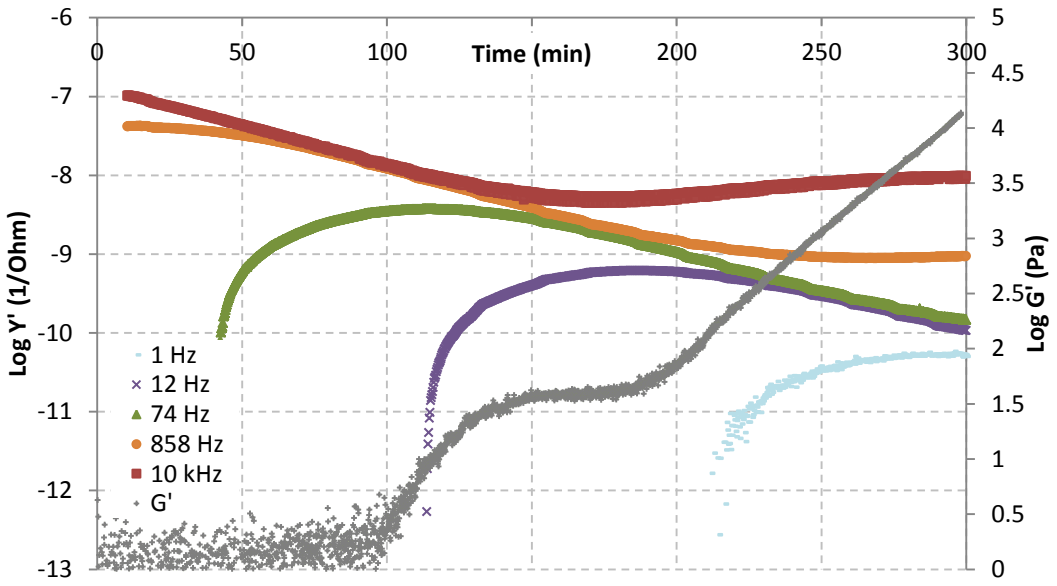
Table 6.5 *Capacitances of the sensors after full resin cure*

	No reinforcement	**3 layers of glass fibre**	**6 layers of glass fibre**
Capacitance (Fa)	1.15×10^{-11}	2.56×10^{-11}	2.80×10^{-11}
% of increase	24%	53%	10%

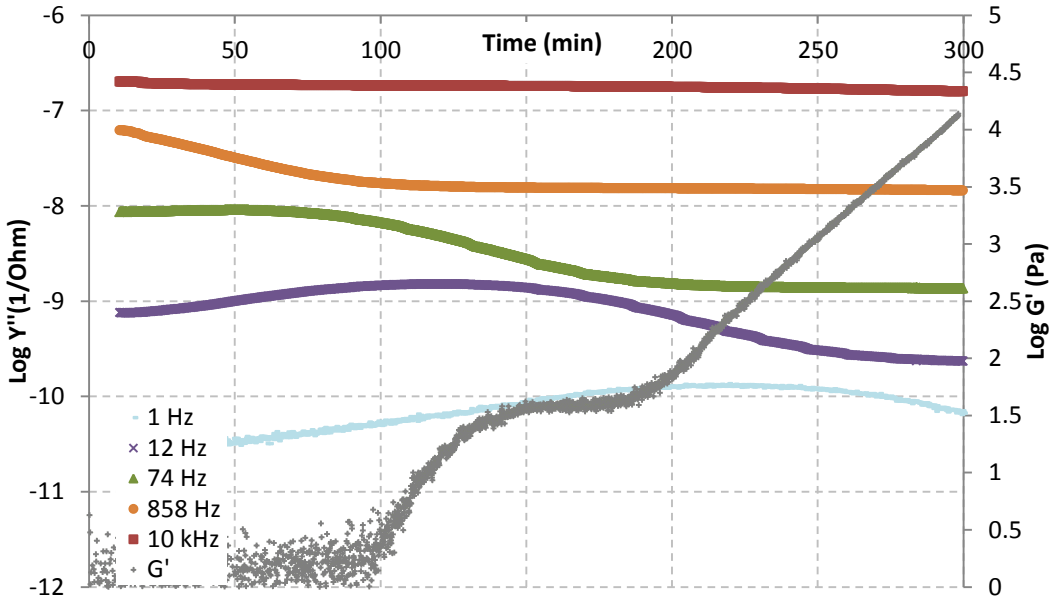
The capacitance of the sensor covered by cured epoxy is predictably higher than the capacitance of the dry sensor, due to the addition of the resin and glass fibre on top of the electrodes. The addition of the cured epoxy and potential glass fibres modifies the resistance and capacitance of the RC circuit corresponding to the dry sensor, as discussed in section 4.4.3. At the cured stage, the addition of glass fibre layers seems to increase the capacitance measure compared to the unreinforced resin, but no real influence of the number of reinforcement layers on the capacitance can be drawn.

6.7. Discussion

The dielectric measurements obtained during the cure of the unreinforced epoxy resin can be compared to the characterisation of the cure carried out in chapter 3. In particular, the determination of the gel point and the advancement of cure can confirm the interpretation of the local maximum observed in the admittance curves. The curves for the admittance and elastic modulus of the resin around gelation are given in Figure 6.17.



(a)



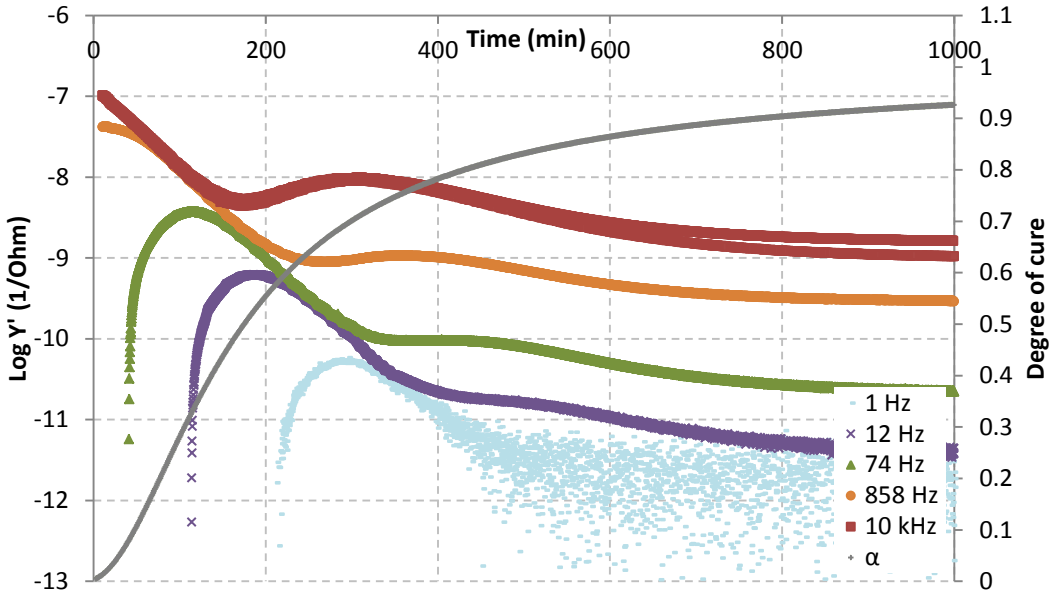
(b)

Figure 6.17 *Evolution of the elastic modulus, real (a) and imaginary (b) part of the admittance during the cure of RS-M135 epoxy resin at 20 ˚C*

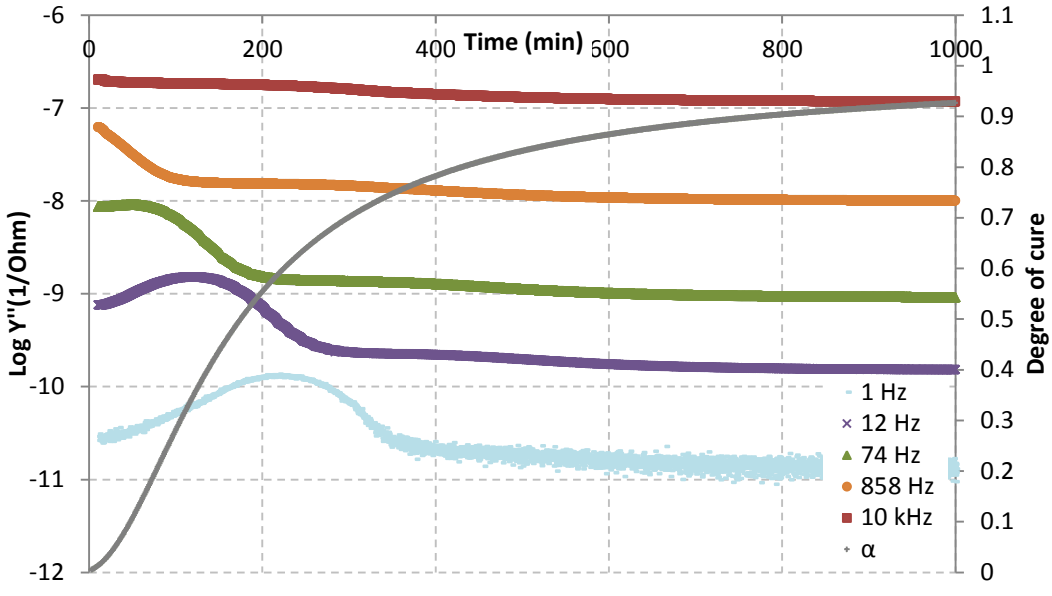
At ambient temperature, the gel point of the resin determined by using the change in the elastic modulus slope seems to correspond to the local minimum of Y' at 10 kHz. At the beginning of the cure, the signal is dominated by the charge migration. As the resin cures and its viscosity increases, the mobility of the ions decreases and the dipole contribution becomes visible on the real admittance. When vitrification occurs, the ionic species are trapped inside the 3D network and thus only the dipoles are responsible for the dielectric properties of the glassy resin.

The imaginary part of the admittance does not present any remarkable correlation with the elastic modulus. However, the local maximums happen before the gel point of the resin for all frequencies but 1 Hz. These results must be mitigated by the potential inaccuracy of the viscosity results discussed in section 3.4.

The degree of cure at which every local maximum appear can be determined using Figure 6.18.



(a)



(b)

Figure 6.18 *Evolution of the degree of cure α, real (a) and imaginary (b) part of the admittance during the cure of RS-M135 epoxy resin at 20 ˚C*

The location of the dipole relaxation maximums and their corresponding admittance are given in Table 6.6. For the real admittance, the peaks are observed after the gel point, determined to be 58% of cure in section 3.6. On the contrary, all

the local maximums observed for the imaginary part of the admittance take place before gelation.

Table 6.6 *Location of the dipole relaxation peaks and corresponding degree of cure for the RM-S135 resin cure at 20˚C*

Frequency	Y'(Ohm^{-1})	Time (min)	Degree of cure
74 Hz	9.61x10^{-11}	416	79%
858 Hz	1.06x10^{-9}	347	74%
10 KHz	9.75x10^{-9}	309	71%
Frequency	**Y''(Ohm^{-1})**	**Time (min)**	**Degree of cure**
1 Hz	1.35x10^{-10}	219	59%
12 Hz	1.51x10^{-9}	119	34%
74 Hz	9.10x10^{-9}	47	10%

Assuming that the dipolar relaxations happen at a set degree of cure for each frequency, following the local maximums of the real and imaginary admittance can provide information about the advancement of the cure reaction. By monitoring the admittance and using those maximums as indicators of a certain degree of the resin cure, it is possible to have an estimation of the reaction stage in real time. This estimation is however limited to degrees of cure close to the gel point of the resin studied, as the maximum degree of cure observable is 79%. This maximum degree of cure corresponds to the vitrification of the resin, after which the polymer becomes a glassy solid and the polymerisation reaction dies down.

In the present study, the variations of the complex admittance were investigated, but it is not the only way to follow the polymerisation reaction using the dielectric properties of the epoxy resin under cure. As mentioned in section 4.4.1, it is possible to use other immitances instead, such as the complex impedance (Skordos and Partridge, 2004).

The 3D crosslinking of the resin hinders the migration of charged species, thus resulting in an increasing impedance of the system as the polymerisation reaction progresses. The imaginary impedance spectrum of an epoxy resin is of interest as it presents a minimum and a clear maximum. By following the variations of that spectrum, and particularly the evolution of its maximum along the cure, it is thus possible to follow the cure reaction. Typically, for an isothermal setting such as the one described in the present study, the absolute value of the imaginary impedance maximum increases as the cure progresses because of the decreasing mobility of the charged species. The increased viscosity of the resin also implies an augmentation of the characteristic time of the dipoles present in the system, which in turns results in a shift of the imaginary impedance spectrum towards lower frequencies with time. Plotting the imaginary impedance maximum versus the cure time would result in a curve similar to the DSC results observed in Figure 3.10 : the curve would present an increase as the reaction progresses, before reaching a plateau at the end when the reaction dies down. The cure reaction of the epoxy resin used in the present work could thus be investigated by following the variations of the imaginary impedance maximum.

6.8. Chapter Summary

In this chapter, a prototype for a new type of dielectric sensor was manufactured. Based on flat copper electrodes embedded in a flexible PEEK matrix, its dimensions are suitable to follow resin infusions on the scale of several centimetres. The aptitude of this prototype to follow the filling of an infusion mould by epoxy resin was demonstrated, both with and without glass fibre reinforcement. The addition of glass fibres did not make a significant difference but for the infusion time. The design of the prototype as an array of parallel electrodes provides a way

to monitor the infusion process in both the direction of the resin flow and across the length of the prototype device.

The prototype demonstrated it could be used to follow the cure of epoxy resin, as well as glass fibre reinforced composite plates. The results obtained while studying the cure process corroborated the prevalence of the ionic contribution to the conductivity of epoxy resin, but the dipolar contribution was discernible as the cure progressed.

By comparing the dielectric measurements obtained with the prototype and the resin characterisation carried out in chapter 3, it was possible to link the said dipolar contribution to the gel point of the epoxy resin at 25 °C and to suggest a way to follow the cure advancement in real time around gelation.

7. Conclusions and Suggestions for Further Work

In this study, a new flexible dielectric sensor has been manufactured. It was used to monitor the infusion and cure of glass fibre reinforced composite panels measuring several centimetres.

7.1. Conclusions

The main conclusions drawn from this study are as follows:

The DSC study of the RS-M135 resin cure with the RS-MH134 hardener validated the autocatalytic nature of the reaction and its independence from the heating rate. Two cure kinetics models of the resin cure were fitted for both dynamic testing conditions and isothermal cure.

The experimental data obtained by studying the resin cure at ambient temperature with dynamic viscometry indicated that the gel point of the resin studied is to be determined using the change in the elastic modulus slope curve rather than the crossover of the elastic and viscous modulus curves. This gel point was found to be 200 minutes after the resin and hardener were mixed.

The possibility of following the microscopic phenomena taking place in the resin during cure by investigating the changes in its permittivity was highlighted. The permittivity of the resin was linked to its admittance and an electrical equivalent circuit of the curing resin was discussed.

An equivalent circuit of the dielectric sensor and its surrounding during the infusion process was proposed.

A Kapton® based sensor prototype was developed. Infusions of glycerol and epoxy resin were successfully monitored by this prototype, as well as the cure of unreinforced resin. The results obtained confirmed the entirety of an infusion process could be monitored by following the variations of the admittance with time and/or frequency. It validated the geometry of the final sensor prototype.

A first attempt was made to develop a three dimensional numerical model of the Kapton® prototype during infusion, with limited but encouraging results.

Two PEEK-based sensor prototypes were manufactured in order to determine the best layout and fabrication protocol for the final device. After testing their response to an infusion of glycerol, it was determined that a dielectric sensor prototype formed of parallel flat copper wires pressed into a PEEK matrix would be the best option.

A new flexible dielectric sensor prototype consisting on an array of flat copper electrodes embedded in a sheet of PEEK was manufactured. It was successfully used to monitor glycerol and epoxy infusion. The cure reactions of epoxy resin, both with and without glass fibre reinforcement, were also followed with the device.

The design of the said prototype, an array of copper wires electrodes, allowed one to monitor the filling of the mould in two dimensions. The length of the sensor wetted could be linked to the impedance measured, and the time difference between each sensor signal gave indications about the progression of the resin perpendicularly to the flow front. The addition of glass fibre reinforcement did not seem to have a distinct influence on the admittance measured but for an increased incertitude.

The cure of the commercially available RS-M135 epoxy resin could be monitored with the flexible sensor prototype. This extended to the glass fibre reinforced

composite manufactured with this resin. The number of reinforcement layers did not seem to affect the prototype ability to follow the cure.

The parallel RC electrical equivalent of the sensor was proven valid for the dry prototype. It remained valid when the prototype was covered in cured resin, both with and without glass fibres.

7.2. Suggestions for further work

The sensor prototype developed in this study proved that an array of copper wire electrodes held in place by a PEEK matrix could be used as an effective way to monitor the infusion and cure process of glass fibre reinforced epoxy composites. The development of reusable, large scale dielectric sensors able to fit in a wind turbine blade mould is thus conceivable on the long term.

A first attempt at a 3D numerical model of the sensor response during infusion and cure has been done in this study, but its findings were very limited. A 3D numerical model of the sensor and its surrounding would be a powerful tool for the sensor design and the optimisation of the resin cure profile. That numerical model could be used in a variety of applications. The influence of different sensor parameters (nature of the matrix, dimensions, wire position…) on the sensor response could be studied in order to optimise the design of the device to different composites cures, or mould geometries, without the need to manufacture prototypes. Coupling the electrostatic modelling with a fluid mechanic model for the resin flow inside the mould would allow the simulation of infusion processes and could be used as a predictive tool. Similarly, modelling the change in the resin permittivity as it polymerises could provide a simulation of the cure process. With a numerical model powerful enough, a simulation of the whole infusion process from the filling of the mould to the final composite could be envisaged. The parameters of the infusion and cure, such as temperature and pressure, could be optimised

numerically and a simulation of the dielectric sensor response during a “perfect cure” could be developed. By using the actual dielectric sensor measurements in a real time loop and comparing them with the simulation, instant feedback on the cure could be attained. This would allow the detection and potential correction of problems during the cure rather than waiting for the final composite piece to be finished for inspection. Additionally, instant feedback would allow interventions on the cure parameters in real time if necessary, such as adjusting the mould temperature if the curing reaction speed is found inadequate.

The dielectric sensor developed could also be used to detect defects in the final composite plate, such as voids, porosity, foreign inclusions or delamination. This would be done directly after cure and before demoulding of the piece. Interrogating different electrodes along the array would provide indications on the location of the defects in two dimensions: determining the couples of electrodes showing a non-conform signal would first provide a band of material to be investigated as well as information about the size of the defect. Then, using the array design of the sensor to vary the distance inter-electrode would allow an evaluation of the depth of the defect. To enable such a use of the dielectric sensor, a study of the impact of different composite defects on the measured admittance must be carried out. To that end, intentionally flawed pieces of composites would need to be produced in a known and reproducible way, in order to characterise their admittance and compare it to the one obtained with a perfect composite.

The present work provided encouraging results, but more work needs to be done in order to make this technique applicable to the challenges of the wind turbine industry.

8. References

Agarwal, B. D., Broutman, L. J. and Chandrashekhara, K. (2017) *Analysis and Performance of Fiber Composites*. Edited by John Wiley & Sons.

Ashcroft, W. R. (1993) 'Curing agents for epoxy resins', in Ellis, B. (ed.) *Chemistry and Technology of Epoxy Resins*. Springer, Dordrecht, pp. 37–71.

Bang, K. G. *et al.* (2001) 'Measurement of the degree of cure of glass fiber-epoxy composites using dielectrometry', *Journal of Materials Processing Technology*, 113(1–3), pp. 209–214. doi: 10.1016/S0924-0136(01)00657-4.

Bidstrup, S. A., Sheppard, N. F. and Senturia, S. D. (1989) 'Dielectric analysis of the cure of thermosetting epoxy/amine systems', *Polymer Engineering & Science*, 29(5), pp. 325–328. doi: 10.1002/pen.760290510.

Bilyeu, B., Brostow, W. and Menard, K. P. (2001) 'Epoxy Thermosets and their Applications III. Kinetic Equations and Models', *Journal of Materials Education*, 23(4–6), pp. 189–204.

Bogetti, T. A. and Gillespie, J. W. (1991) 'Two-Dimensional Cure Simulation of Thick Thermosetting Composites', *Journal of Composite Materials*, 25, pp. 239–273. doi: 10.1177/002199839102500302.

Brøndsted, P., Lilholt, H. and Lystrup, A. (2005) 'Composite Materials for Wind Power Turbine Blades', *Annual Review of Materials Research*, 35(1), pp. 505–538. doi: 10.1146/annurev.matsci.35.100303.110641.

Brouwer, W. D., Van Herpt, E. C. F. C. and Labordus, M. (2003) 'Vacuum injection moulding for large structural applications', *Composites Part A: Applied Science and Manufacturing*, 34(6 SPEC.), pp. 551–558. doi: 10.1016/S1359-835X(03)00060-5.

Cairns, D. S., Riddle, T. and Nelson, J. (2011) 'Wind Turbine Composite Blade Manufacturing : The Need for Understanding Defect Origins , Prevalence , Implications and Reliability', (February), pp. 1–25. Available at: http://www.ntis.gov/help/ordermethods.asp?loc=7?4?0#online.

Caithness Windfarm Information Forum (2018) *Summary of Wind Turbine Accident data to 30 June 2018*. Available at: http://www.caithnesswindfarms.co.uk/accidents.pdf.

Chin, W. S. and Lee, D. G. (2007) 'Laminating rule for predicting the dielectric properties of E-glass/epoxy laminate composite', *Composite Structures*, 77(3), pp. 373–382. doi: 10.1016/j.compstruct.2005.07.019.

Ciang, C. C., Lee, J. R. and Bang, H. J. (2008) 'Structural health monitoring for a wind turbine system: A review of damage detection methods', *Measurement Science and Technology*, 19(12). doi: 10.1088/0957-0233/19/12/122001.

Day, D. R. *et al.* (1985) 'The Role of Boundary Layer Capacitance at Blocking Electrodes in the Interpretation of Dielectric Cure Data in Adhesives', *The Journal of Adhesion*, 18(1), pp. 73–90. doi: 10.1080/00218468508074937.

Deshpande, A. P. (2009) *Techniques in oscillatory shear rheology*, *Conference Proceedings*. Available at: http://www.physics.iitm.ac.in/~compflu/Lect-notes/abhijit.pdf.

Dupont (2018) 'Dupont ™ kapton ® General Specifications datasheet'.

Fava, R. A. and Horsfield, A. E. (1968) 'The interpretation of electrical resistivity measurements during epoxy resin cure', *Journal of Physics D: Applied Physics*, 1(1), pp. 117–120. doi: 10.1088/0022-3727/1/1/417.

Feldman, Y. *et al.* (2001) 'Electrode polarization correction in time domain dielectric spectroscopy', *Measurement Science and Technology*, 12(8), pp. 1355–1364. doi: 10.1088/0957-0233/12/8/351.

Flory, P. J. (1953) *Principle of polymer chemistry*. Cornell University Press.

Franck, A. (2004) 'Understanding Rheology of Thermoplastic Polymers', *TA Instruments*, 118, pp. 1–8. Available at: http://scholar.google.com/scholar?hl=en&btnG=Search&q=intitle:Understanding+Rheology+of+Thermoplastic+Polymers#4.

Galappaaththi, U. I. K. *et al.* (2013) 'The Effect of Ply Waviness for the Fatigue Life of Composite Wind Turbine Blades', *Renewable Energy and Power Quality Journal*, 1(11), pp. 1195–1199. doi: 10.24084/repqj11.574.

Galappaaththi, U. I. K. *et al.* (2013) 'Strategic Quality Control Measures to Reduce Defects in Composite Wind Turbine Blades', *Renewable Energy and Power Quality Journal*, 1(11), pp. 1244–1249. doi: 10.24084/repqj11.589.

Gallone, G. *et al.* (2001) 'Dielectric analysis of the linear polymerization of an epoxy resin', *Polymer International*, 50(5), pp. 545–551. doi: 10.1002/pi.663.

Gurit Holding (2016) *Guide to composites*. doi: GTC-3-0509 Available at: https://www.gurit.com/-/media/Gurit/Datasheets/guide-to-composites.pdf.

Hahn, B., Durstewitz, M. and Rohrig, K. (2007) 'Reliability of Wind Turbines: Experiences of 15 years with 1,500 WTs', *Wind Energy: Proceedings of the Euromech Colloquium*, (July), pp. 329–332. doi: 10.1007/978-3-540-33866-6.

Horie, K. *et al.* (1970) 'Calorimetric investigation of polymerization reactions. III. Curing reaction of epoxides with amines', *Journal of Polymer Science Part A-1: Polymer Chemistry*, 8(6), pp. 1357–1372. doi: 10.1007/s10549-017-4547-3.

Inada, T. and Todoroki, A. (2003) 'Cure Monitoring of CFRP Using Electric Capacitance Change with Applied AC Frequency', *Journal of the Society of Materials Science, Japan*, 52(8), pp. 922–926. doi: 10.2472/jsms.52.922.

Karkanas, P. I. and Partridge, I. K. (2000) 'Cure Modeling and Monitoring of Epoxy/Amine Resin Systems. II. Network Formation and Chemoviscosity Modeling', *Journal of Applied Polymer Science*, 77, pp. 2178–2188. doi: 10.1002/1097-4628(20000815)77:7<1419::AID-APP3>3.0.CO;2-N.

Karkanas, Panagiotis I. and Partridge, I. K. (2000) 'Cure Modeling and Monitoring of Epoxy / Amine Resin Systems . I . Cure Kinetics Modeling', *Journal of Applied Polymer Science*, 77, pp. 1419–1431.

Karkanas, P. I., Partridge, I. K. and Attwood, D. (1996) 'Modelling the Cure of a Commercial Epoxy Resin for Applications in Resin Transfer Moulding', *Polymer International 41*, 41(2), pp. 183–191.

Kenny, J. M., Maffezzoli, A. and Nicolais, L. (1990) 'A model for the thermal and chemorheological behavior of thermoset processing: (I) Processing of epoxy-based composites', *Composites Science and Technology*, 29(15), pp. 339–358.

Kenny, J. M. and Trivisano, A. (1991) 'Isothermal and dynamic reaction kinetics of high performance epoxy matrices', *Polymer Engineering & Science*, 31(19), pp. 1426–1433. doi: 10.1002/pen.760311909.

Konstantopoulos, S., Fauster, E. and Schledjewski, R. (2014) 'Monitoring the production of FRP composites: A review of in-line sensing methods', *Express Polymer Letters*, 8(11), pp. 823–840. doi: 10.3144/expresspolymlett.2014.84.

Kranbuehl, D. *et al.* (1989) 'Use of the frequency dependence of the impedance to monitor viscosity during cure', *Polymer Engineering & Science*, 29(5), pp. 285–289. doi: 10.1002/pen.760290504.

Kranbuehl, D. *et al.* (1997) 'In Situ Monitoring of Polymer Processing Properties', *Polymers for Advanced Technologies*, 8(2), pp. 93–99. doi: 10.1002/(SICI)1099-1581(199702)8:2<93::AID-PAT615>3.0.CO;2-S.

Lapique, F. and Redford, K. (2002) 'Curing effects on viscosity and mechanical properties of a commercial epoxy resin adhesive', *International Journal of Adhesion and Adhesives*, 22(4), pp. 337–346. doi: 10.1016/S0143-7496(02)00013-1.

Laurent-Mounier, A., Binétruy, C. and Krawczak, P. (2005) 'Multipurpose carbon fiber sensor design for analysis and monitoring of the resin transfer molding of polymer composites', *Polymer Composites*, 26(5), pp. 717–730. doi: 10.1002/pc.20104.

Lauter, C. *et al.* (2017) 'Improvement of Productivity and Quality in the Wind Energy Industry Through the Use of an Advanced Sensor System', *Sampe Europe*, 53(6), pp. 6–10.

Lira, C. *et al.* (2017) 'Automating resin transfer moulding', *Sampe Europe*, (Dc).

Macdonald, J. R. (1987) 'Impedence Spectroscopy--Emphasizing Solid Materials and Systems', *Wiley-Interscience, John Wiley and Sons*, pp. 1–346.

Mamishev, A. V *et al.* (2004) 'Interdigital Sensors and transducers', *Proceedings of the IEEE*, 92(5), pp. 808–845.

Matějka, L. (1991) 'Rheology of epoxy networks near the gel point', *Polymer Bulletin*, 26(1), pp. 109–116. doi: https://doi.org/10.1007/BF00299355.

Matsuzaki, R. *et al.* (2011a) 'Control of resin flow/temperature using multifunctional interdigital electrode array film during a VaRTM process', *Composites Part A: Applied Science and Manufacturing*, 42(7), pp. 782–793. doi: 10.1016/j.compositesa.2011.03.004.

Matsuzaki, R. *et al.* (2011b) 'Full-field monitoring of resin flow using an area-sensor array in a VaRTM process', *Composites Part A: Applied Science and Manufacturing*, 42(5), pp. 550–559. doi: 10.1016/j.compositesa.2011.01.014.

Matsuzaki, R. *et al.* (2012) 'Cross-sectional monitoring of resin impregnation using an area-sensor array in an RTM process', *Composites Part A: Applied Science and Manufacturing*. Elsevier Ltd, 43(4), pp. 695–702. doi: 10.1016/j.compositesa.2011.12.024.

Matthews, F. L. and Rawlings, R. D. (1999) *Composite Materials: Engineering and Science*. Elsevier Ltd.

McIlhagger, A., Brown, D. and Hill, B. (2000) 'Development of a dielectric system for the on-line cure monitoring of the resin transfer moulding process', *Composites Part A: Applied Science and Manufacturing*, 31(12), pp. 1373–1381. doi: 10.1016/S1359-835X(00)00050-6.

Mijović, J. *et al.* (1996) 'Impedance spectroscopy of reactive polymers. 3. Correlations between dielectric, spectroscopic, and rheological properties during cure of a trifunctional epoxy resin', *Journal of Polymer Science, Part B: Polymer Physics*, 34(2), pp. 379–388. doi: 10.1002/polb.1996.885.

Mijovic, J. and Fitz, B. D. (1998) 'Dielectric Spectroscopy of Reactive Polymers', *Materials Science*, 2(Section 5), pp. 1531–9. doi: 10.1109/ISE.1999.832080.

Nixdorf, K. and Busse, G. (2001) 'The dielectric properties of glass-fibre-reinforced epoxy resin during polymerisation', *Composites Science and Technology*, 61(6), pp. 889–894. doi: 10.1016/S0266-3538(00)00174-3.

Orphanidis, S. . (1999) *Electromagnetic Waves and Antennas*. Rutgers University.

PRF Composite Materials (2015a) *Product Data, Composite Reinforcement, Glass fabric*. Available at: www.prfcomposites.com/wp-content/uploads/2015/07/ER006EGLAS1250-1.1-Jul-2015.pdf (Accessed: 23 November 2018).

PRF Composite Materials (2015b) *Product Data, Epoxy Resin Systems RS-M135*. Available at: www.prfcomposites.com/store/image/data/PDF/RS-M135.pdf%0A%0A (Accessed: 23 November 2018).

PRF Composite Materials (no date) *Epoxy Resin Systems*. Available at: http://www.prfcomposites.com/materials/resin/ (Accessed: 23 November 2018).

Psarras, G. C., Manolakaki, E. and Tsangaris, G. M. (2002) 'Electrical relaxations in polymeric particulate composites of epoxy resin and metal particles', *Composites - Part A: Applied Science and Manufacturing*, 33(3), pp. 375–384. doi: 10.1016/S1359-835X(01)00117-8.

Schubel, P. J. *et al.* (2013) 'Review of structural health and cure monitoring techniques for large wind turbine blades', *Renewable Energy*. Elsevier Ltd, 51, pp. 113–123. doi: 10.1016/j.renene.2012.08.072.

Segur, J. (1953) 'Physical properties of glycerol and its solutions', *Glycerol*, 2, pp. 1–27. doi: 10.1007/s13398-014-0173-7.2.

Senturia, S. D. and Sheppard Jr, N. F. (1986) 'Dielectric analysis of thermoset

cure', *Advances in Polymer Science*, 80(3), pp. 1–47. doi: 10.1007/3-540-16423-5.

Shigue, C. Y. *et al.* (2004) 'Monitoring the epoxy curing by the dielectric thermal analysis method', *IEEE Transactions on Applied Superconductivity*, 14(2), pp. 1173–1176. doi: 10.1109/TASC.2004.830477.

Shigue, C. Y. *et al.* (2006) 'Dielectric Thermal Analysis as a Tool for Quantitative Evaluation of the Viscosity and the Kinetics of Epoxy Resin Cure', *IEEE Transactions on Applied Superconductivity*, 16(2), pp. 1786–1789. doi: 10.1109/TASC.2005.869624.

Skordos, A. A., Karkanas, P. I. and Partridge, I. K. (2000) 'A dielectric sensor for measuring flow in resin transfer moulding', *Measurement Science and Technology*, 11(1), pp. 25–31. doi: 10.1088/0957-0233/11/1/304.

Skordos, A. A. and Partridge, I. K. (2004) 'Determination of the degree of cure under dynamic and isothermal curing conditions with electrical impedance spectroscopy', *Journal of Polymer Science, Part B: Polymer Physics*, 42(1), pp. 146–154. doi: 10.1002/polb.10676.

Sørensen, B. F. *et al.* (2004) *Improved design of large wind turbine blade of fibre composites based on studies of scale effects (Phase 1) - Summary Report*. doi: Risø-R-1390(EN).

Stephan, F., Duteurtre, X. and Fit, A. (1998) 'In-process control of epoxy composite by microdielectrometric analysis. Part II: On-line real-time dielectric measurements during a compression molding process', *Polymer Engineering and Science*, 38(9), pp. 1566–1571. doi: 10.1002/pen.10327.

Tsangaris, G. M., Psarras, G. C. and Kouloumbi, N. (1998) 'Electric modulus and interfacial polarization in composite polymeric systems', *Journal of Materials Science*, 33(8), pp. 2027–2037. doi: 10.1023/A:1004398514901.

Tung, C. M. and Dynes, P. J. (1982) 'Relationship between Viscoelastic Properties and Gelation in Thermosetting Systems', *Journal of Applied Polymer Science*, 27(I), pp. 569–574.

Vaidya, U. K., Jadhav, N. C. and Hosur, M. V (2000) 'Assessment of flow and cure monitoring using direct current and alternating current sensing in vacuum-assisted resin transfer molding', 727.

Veers, P. S. *et al.* (2003) 'Trends in the design, manufacture and evaluation of wind turbine blades', *Wind Energy*, 6(3), pp. 245–259. doi: 10.1002/we.90.

Wadsworth, J. and Lesuer, D. R. (2000) 'Ancient and modern laminated composites - from the Great Pyramid of Gizeh to Y2K', *Materials Characterization*, 45(4–5), pp. 289–313.

Yang, J. *et al.* (2013) 'Structural investigation of composite wind turbine blade considering structural collapse in full-scale static tests', *Composite Structures*. Elsevier Ltd, 97, pp. 15–29. doi: 10.1016/j.compstruct.2012.10.055.

Yang, Y. *et al.* (2014) 'Development of a Dielectric Sensor System for the On-line Cure Monitoring of Composites', *Procedia Technology*. Elsevier B.V., 15, pp. 631–637. doi: 10.1016/j.protcy.2014.09.024.

Yang, Y. *et al.* (2016) 'Design and fabrication of a flexible dielectric sensor system for in situ and real-time production monitoring of glass fibre reinforced composites', *Sensors and Actuators, A: Physical*. Elsevier B.V., 243, pp. 103–110. doi: 10.1016/j.sna.2016.03.015.

Yenilmez, B. and Murat Sozer, E. (2009) 'A grid of dielectric sensors to monitor mold filling and resin cure in resin transfer molding', *Composites Part A: Applied Science and Manufacturing*. Elsevier Ltd, 40(4), pp. 476–489. doi: 10.1016/j.compositesa.2009.01.014.